

**POLITECNICO DI TORINO**

**Corso di Laurea Magistrale in  
Ingegneria Biomedica**

**Tesi di Laurea Magistrale**

**Theranostic microparticles  
manufactured through  
Layer by Layer functionalisation**



**Supervisors**

Prof. Gianluca Ciardelli  
Dr. Irene Carmagnola  
Dr. Piergiorgio Gentile

**Candidate**

Alessandro Ferrarini  
Matricola: s249515

**A.A. 2018/2019**



## Declaration of work

I declare that this thesis is based on my own work and has not been submitted in any form for another degree at any University or any other tertiary education. Information derived from published and unpublished work of others have been acknowledged in the text and in the list of references given in the bibliography.

## Abstract

Cancer is considered the leading cause of death and estimates assess that the new tumour cases will rise to 20.3 million per year with 13.2 deaths by 2030.

For improving drug delivery, pharmaco-kinetics, bio-distribution and real-time tracking, the past decade research has been focusing into the development of new theranostic systems able to combine a therapeutic compound with an imaging probe in the same vehicle, able to selectively target cancer cells.

In this work we developed microcapsules, combining the bioimaging properties of excitation-dependent fluorescent graphene quantum dots (GQDs) with therapeutics-loaded microparticles functionalized by electrostatic Layer by Layer (LbL), using calcium carbonate ( $\text{CaCO}_3$ ) core as template. This approach is suitable for drug encapsulation in the core as well as incorporation of biomolecules in the coating as an attractive multi-modal strategy able to be tracked *in vivo* and real time. LbL technology has been widely studied and used in many different fields such as optics, electronic, biology and medicine thanks to its simplicity and versatility. Moreover, semiconductor Quantum Dots (QDs) have emerged as an interesting tool for bioimaging purposes but they presented biocompatibility lack. Recently carbon-based quantum dots have been discovered and applied as imaging probes to replace semiconductor QDs, thanks to their strong fluorescence, water and photo-stability and, mainly, high cytocompatibility. Therefore, in this work GQDs produced from green route, were adopted. Their morphology, physico-chemical and optical properties have been analysed via Transmission Electron Microscopy (TEM), Zeta-potential, Fourier Transform Infrared Spectroscopy (FTIR-ATR), X-ray Photoelectron Spectroscopy (XPS) and UV-Visible (UV-Vis), showing round-shaped structure, negative surface charge and excitation-dependent emission. Moreover, it was assessed their cytocompatibility via Live/Dead and Presto Blue assays, with high fibroblast viability up to 500  $\mu\text{g}/\text{mL}$  concentration and cells ability to internalize the nanoparticles even at low concentration (50  $\mu\text{g}/\text{mL}$ ). Then,  $\text{CaCO}_3$  microparticles have been synthesized starting from calcium chloride ( $\text{CaCl}_2$ ) and sodium carbonate ( $\text{NaCO}_3$ ) reagents, optimizing the process in order to stabilize the  $\text{CaCO}_3$  vaterite form, to avoid the transformation into

calcite (more stable water suspension). To tackle this challenge 1 mg/mL of poly(styrenesulfonate) (PSS) was added to the reagents. Then, the manufactured particles were used as sacrificial template for the deposition of two biocompatible polyelectrolytes, Poly(allylamine hydrochloride) (PAH) (positively charged) and PSS (negatively charged), via LbL technique to create a nanocoating (shell) surrounding the inner  $\text{CaCO}_3$  particle (core).

Subsequently, the QDs were incorporated within the nanocoating after dissolution in PSS. The morphology and final size were investigated via Scanning Electron Microscopy (SEM) as well as the optical properties by using the Confocal Microscope. Following the LbL coating step, the  $\text{CaCO}_3$  core was dissolved in EDTA solution leaving the polyelectrolyte shell to obtain a hollow microcapsule interesting for further investigations regarding drug loading and delivery tests.

Furthermore, as proof of concept, during the last period of the project we reduced the particles size, in order to reach the nanoscale. By dissolving the reagents in Glycerol (83.3% V/V) an average diameter of 700 nm was achieved.

## Acknowledgements

I have now arrived at the end of my university career; I've grown up and improved as a person and this thesis is the perfect conclusion of my academic path and I would like to thank all the people who helped me to accomplish it.

I must thank, first of all, my professors, who allowed me to do this project and helped me during these months: Prof. Gianluca Ciardelli, Dr. Irene Carmagnola and Dr. Chiara Tondaturo, who with their professionalism and experience made this work possible.

Thank you to Newcastle University, in particular to Dr. Ana Marina Ferreira Duarte and Prof. Kenny Dalgarno who welcomed me, allowed me to use their labs and equipment and gave me useful suggestions. I would like to thank Dr. Ann Phan and Mr. Aumber Abbas who provided me with Graphene Quantum Dots and helped me with their expertise and advices.

I must thank two amazing people, met only few months ago, who made my time in Newcastle special. Piergiorgio, a kind person whose passion for his job, his interest and dedication were inspiring, and his precious advices were and will be very important to me. Annachiara, a wonderful friend, who supported me so much in every aspect of the experience, a happy person who manages to put a smile on every face, always present for an advice, a chat or a laugh.

I would like to thank my friends from Mezze, who I've known since I wasn't even born, a friendship that will last forever and I feel very lucky for it. Friends that I met the first day of elementary school and those met in the subsequent years, who I spent every moment of my last 10 with, and I look forward to spend even more time in the future, regardless of what life will reserve us. And I thank those friends met more recently: we supported and helped each other, enjoyed moments in and out the University and without whom this accomplishment wouldn't have been possible.

I want to thank my relatives, who showed in every occasion interest in my studies with special mention to my grandmothers, who I love more than anything.

Last but not least, my parents, Isabella and Enrico, who supported me in every way they could, helped me to overcome obstacles and difficulties, allowed me to live some amazing experiences and have always been there for me and always will be.

This degree is dedicated to them.

# Table of contents

Abstract .....	ii
Acknowledgements.....	iv
Table of contents.....	v
List of figures .....	viii
List of tables .....	xii
List of abbreviations .....	xiii
<b>Chapter 1. Introduction .....</b>	<b>1</b>
1.1 Cancer.....	1
1.1.1 Cancer general features .....	1
1.1.2 Cancer Hallmarks.....	2
1.1.3 Cancer statistics.....	3
1.2 State of the art: New advanced approaches for cancer treatment .....	4
1.2.1 Theranostic approach.....	4
<i>Concept and strategies</i> .....	4
<i>Passive and Active targeting</i> .....	9
1.2.2 Quantum dots .....	13
<i>Carbon-based nanostructures</i> .....	16
<i>Carbon and Graphene Quantum Dots</i> .....	17
1.2.3 Layer by layer technology .....	25
<i>General features and different LbL-based technologies</i> .....	25
<i>LbL application in Nanomedicine</i> .....	31
1.3 Aim and Objectives of the work.....	35
<b>Chapter 2: Manufacturing protocols and characterisation.....</b>	<b>36</b>
2.1 Materials .....	36
2.2 Manufacturing Methods .....	36
2.2.1 CaCO <sub>3</sub> microparticles synthesis.....	36
2.2.2 Nanoparticles synthesis .....	37
2.2.3 Polyelectrolyte deposition .....	37
2.2.4 Graphene-based QDs synthesis .....	38
2.2.5 Combining the CaCO <sub>3</sub> microparticles and the GQDs via LbL assembly.....	38
2.2.6 Microcapsules fabrication .....	39
2.3 Characterisation methods.....	39

2.3.1 QDs characterisation .....	39
2.3.1.1 Physico-chemical analysis .....	39
2.3.1.1.1 Fourier Transformed Infrared spectroscopy (FTIR-ATR) .....	39
2.3.1.1.2 X-ray photoelectron spectroscopy (XPS).....	40
2.3.1.1.3 Zeta Potential .....	40
2.3.1.1.4 Absorbance .....	41
2.3.1.1.5 Fluorescence .....	41
2.3.1.2 Morphological analysis.....	41
2.3.1.2.1 Transmission Electron Microscopy (TEM) .....	41
2.3.1.3 Cytotoxicity Evaluation.....	41
2.3.1.3.1 Live/dead.....	42
2.3.1.3.2 PrestoBlue .....	43
2.3.2 CaCO <sub>3</sub> Characterisation .....	43
2.3.2.1 Physico-chemical analysis .....	43
2.3.2.1.1 Quartz Crystal Microbalance (QCM) .....	43
2.3.2.2 Morphological analysis.....	44
2.3.2.2.1 Scanning Electron Microscopy (SEM).....	44
2.3.2.3 Cellular uptake analysis.....	44
2.3.3 Statistical analysis.....	45
<b>Chapter 3. Results</b> .....	46
3.1 Graphene Quantum Dots .....	46
3.1.1 Morphological characterisation .....	46
3.1.2 Physico-chemical characterization.....	47
3.1.3 Optical properties.....	49
3.1.4 Cytocompatibility assessment.....	50
3.2 CaCO <sub>3</sub> synthesis and functionalisation .....	54
3.2.1 Morphological characterisation .....	54
3.2.1.1 LbL-Functionalisation of CaCO <sub>3</sub> Microparticles .....	56
3.2.1.2 CaCO <sub>3</sub> Nanoparticles synthesis.....	59
3.2.2 Physico-chemical characterisation.....	61
3.2.2.1 Quartz crystal microbalance .....	61
3.2.2.2 FTIR-ATR and XPS analysis.....	63
3.2.3 Cellular uptake studies .....	73
<b>Chapter 4. Discussion</b> .....	75
4.1 Graphene Quantum Dots .....	75
4.2 Bioimaging analysis .....	78

4.3 CaCO <sub>3</sub> microparticles synthesis and protocol optimization .....	78
4.4 LbL functionalisation .....	81
4.5 Nanoparticles synthesis .....	86
<b>Chapter 5. Conclusion and future perspectives.....</b>	<b>88</b>
References.....	91

## List of figures

Figure 1.1 Metastasis formation: cancer cells spread through blood vessels or lymphatic system, reaching different areas of the body. ....	xii
Figure 1.2 The six cancer hallmarks (Hanahan and Weinberg 2011) .....	2
Figure 1.3 UK Cancer statistics [Cancerresearchuk.org] .....	4
Figure 1.4 Growing number of publications regarding theranostic systems between 2010 and 2015 (Y. Ma et al. 2016) .....	4
Figure 1.5 Advantages of Theranostic platforms. Improvements in drug delivery and bio-distribution are achieved; it's possible to track the system and to combine various therapeutics in the same vehicle.....	5
Figure 1.6 Illustration of the pH-responsive drug releasing mechanism of the Folic Acid functionalized theranostic system: when reaching the cancer environment the ligand-receptor interaction allows the internalization of the drug carrier, which releases the cargo thanks to the acidic pH in the cytoplasm (Chiu et al. 2016).....	6
Figure 1.7 Illustration of the EPR effect: the nanoparticles manage to extravasate and enter the tumor environment thanks to the leaky vasculature, typical of the cancer vessels. A healthy vessel has a compact endothelial wall, prohibiting the particles' passage. ....	10
Figure 1.8 active targeted nanoparticle. The surface can be functionalized with peptides, antibodies, nucleic acids, polymers and ligands. Therapeutic compounds and imaging agents can be loaded into the carrier or deposited on the external surface. ....	11
Figure 1.9 Band Theory of semiconductor materials, Quantum Confinement Effect and light emission mechanism. As the QD diameter decreases the Band Gap Increases, emitting more energetic photons. ....	13
Figure 1.10 Cell viability comparison between bare CdSe and ZnS-capped CdSe: when coated the QDs' cytotoxic effects decrease. The UV exposure increases the ROS production, decreasing the cell viability (Derfus, Chan, and Bhatia 2004).....	15
Figure 1.11 Different Carbon-based nanomaterials and the potential applications (Chen et al. 2015) .....	17
Figure 1.12 Carbon Quantum Dot, sphere-shaped with surface passivation to enhance fluorescence. Graphene Quantum Dots with the peculiar honeycomb structure like graphite.	18
Figure 1.13 Photoluminescence spectra of carbon-based QDs. a) excitation-dependent emission (Nair et al. 2017) b) excitation independent emission (Chiu et al. 2016).....	19
Figure 1.14 CDs internalized by cells and excited at different wavelengths. a) brightfield image b) 330-385 nm c) 450-480 nm d) 510-550 nm. Scale bar: 50 $\mu$ m (S. Zhao et al. 2015) .....	20
Figure 1.15 Schematic illustration of Top Down and Bottom Up methods. The former uses a large carbon source that gets cut in small nanostructures. The latter begins from an organic precursor, irradiated with energy that leads to nucleation and synthesis of QDs. ....	21

Figure 1.16 Alternative deposition of oppositely charged polyelectrolytes on a pre-charged substrate .....	25
Figure 1.17 Illustration of the immersive Layer by Layer.....	26
Figure 1.18 A) Scheme of the drug-loaded nanoparticle coated through LbL, using siRNA as polyanion and various materials as polycation. B) TEM images clearly showing the core-shell structure. (Deng et al. 2013) .....	28
Figure 1.19 Scheme of the Spray LbL technique (Saqib and Aljundi 2016) . Steps 1 and 3 illustrate the polyelectrolytes deposition, while steps 2 and 4 the rinse passages.....	29
Figure 1.20 Comparison between the layer deposition in the immersive and Spin LbL. The former creates a disorganized structure in which the polyelectrolytes mix together. The latter instead creates a well organized architecture with the final film well stratified (J. J. Richardson, Bjornmalm, and Caruso 2015).....	30
Figure 1.21 Representation of the electrodeposition and microfluidic LbL. (XIAO et al. 2016) .	31
Figure 1.22 Coating process of a particle that in the last step is dissolved, leaving a hollow capsule (Johnston et al. 2006).....	33
Figure 1.23 Schematic illustrations of the CaCO <sub>3</sub> functionalization with PAH and PSS, the incorporation within the layers of the GQDs and the final inner core dissolution.....	35
Figure 2.1 Schematic illustration of the LbL functionalization. A total of 7.5 cycles were conducted.....	38
Figure 2.2 LbL process with the addition of GQDs from the 10th layer.....	39
Figure 2.3 image displaying the well-plates used for the cytocompatibility tests. a) 24 well-plate for Live/Dead, cell cultured with various GQDs-based medium concentrations. b) 96 well-plate for Presto Blue, solution already poured and ready for scanning .....	42
Figure 3.1 TEM pictures of GQDs, with a wide size distribution, ranging from 4.5 nm to 100 nm. Pictures E & F) show the tendency of the structures to agglomerate in water.....	46
Figure 3.2 FTIR-ATR spectrum of GQDs and their highlighted surface functional groups. Table 3.1 schematize the chemical bonds and the respective wavenumbers. ....	47
Figure 3.3 A) XPS survey spectrum of the GQDs; B) High resolution spectrum of the C <sub>1s</sub> element in GQDs.....	48
Figure 3.4 color shift of GQD water-based solution under exposure to UV light .....	49
Figure 3.5 a) Fluorescence and b) absorbance patterns of the GQDs. The former shows a typical excitation dependent behavior; the latter displays two shoulders centered at 280nm and 320 nm. ....	50
Figure 3.6 Live/Dead fluorescent microscope pictures. a) Neo-Fibroblasts and Y201 MSCs incubated with 5 different concentrations of green GQDs, ad examined after 24h and 48h. b) Neo-Fibroblasts and Y201 MSCs incubated with 5 different concentrations of industrial GQDs, ad examined after 24h and 48h. cells stained green are viable; red ones are dead. Scale bar 50 μm. ....	51
Figure 3.7 Metabolic activity of Fibroblasts incubated 48h with (a) green GQDs and (b) industrial GQDs. Metabolic activity of Y201 MSCs incubated 48h with (c) green GQDs and (d) industrial GQDs. Statistical analysis is represented: p<0.0001 ****; p<0.001 ***; p<0.05 * ....	52

Figure 3.8 Confocal microscope images taken after 24 h of incubation of cells and GQDs. A) Fibroblast cultured with 0.2 mg/mL GQDs concentration B) Y201 seeded with 0.05 mg/mL GQDs concentration.....	53
Figure 3.9 SEM pictures of the CaCO <sub>3</sub> microparticles synthesised after 2,5,10 min of precursor mixing and after drying at RT and 37°C. Scale bar Figure A = 5µm; Scale Bar B-F = 10 µm .....	54
Figure 3.10 SEM pictures of CaCO <sub>3</sub> particles with PSS at RT and with and without PSS at 35°C. The temperature changes the morphology of the particles, while the only addition of PSS generates a product with only spheres.....	55
Figure 3.11 SEM pictures showing the microparticles morphology after immersion in water without A) and with PSS addition in the precursors solution B). C & D) synthesis temperature set at 35°C without and with PSS respectively.....	56
Figure 3.12 SEM pictures A and B show the coated particles after 3 layers deposited. C and D show the particles after 15 layers deposited. ....	57
Figure 3.13 Average particles' diameters are represented. a) comparison between the microparticles with and without outer shell. b) comparison between coated particles with and without GQDs.....	57
Figure 3.14 A) the internal structure of a microparticle; B) microparticle after the LbL assembly, with the external PEs shell highlighted .....	58
Figure 3.15 SEM picture of the CaCO <sub>3</sub> particles after the LbL process incorporating GQDs onto the surface.....	58
Figure 3.16 Particles morphology after EDTA core dissolution procedure. A) Microcapsule without GQDs B) with GQDs. ....	59
Figure 3.17 SEM pictures displaying microparticles, with circular shape and an average size of 1.7 µm. ....	59
Figure 3.18 SEM picture showing the product of the tests aiming to reduce the particles' size. a) 2 and 50 min. reaction conducted in 83% of glycerol without PSS. b) 50 min. reaction in 83% of glycerol with the addition of PSS. Red arrows are indicative of particles with diameters of 320 nm up to 810nm.....	60
Figure 3.19 Graph representing the average diameters of the microparticles obtained with three different reactions. There is a decreasing trend, confirmed by the statistical analysis....	60
Figure 3.20 Frequency (below) and energy dissipation (above) shifts resulted from the deposition of PEs (Grey) and PEs with GQDs (Orange).....	61
Figure 3.21 Mass change in response to the adsorption of the layers. ....	62
Figure 3.22 multilayer thickness obtained after 15 layers of a) only PEs) and b) PEs with GQDs. ....	62
Figure 3.23 FITR spectra of the CaCO <sub>3</sub> obtained after the same reaction conducted for different durations (2,5,10 min). The peaks highlighted indicate the presence of vaterite and calcite. The enlargement shows the intensity of the cited peaks. ....	63
Figure 3.24 Spectra of the synthesis conducted with the addition of PSS or changing the reaction temperature. The peaks highlighted are characteristic of vaterite and calcite phases. ....	64
Figure 3.25 FTIR spectra of a) particles after being dissolved 4h in water; b) particles after 3 layers deposited. ....	64

Figure 3.26 FTIR spectra of PAH (green), PSS (yellow) and functionalized particles after the adsorption of 15 layers. The zoomed picture highlights the vaterite and calcite peaks. ....	66
Figure 3.27 FTIR spectra before the core dissolution (green) and after the core dissolution (blue). ....	67
Figure 3.28 XPS survey spectra of the microparticles and microcapsules. ....	68
Figure 3.29 Zeta potential trend during LbL assembly. a) 100 mg of microparticles b) 50 mg of microparticles. Polyelectrolyte concentration was kept at 2 mg/mL in a total of 10 mL and the duration of each coating step was set at 10 min. ....	70
Figure 3.30 PEs concentration was set at 5mg/mL. a) deposition time of 10 minutes. B) deposition time of 15 minutes. ....	71
Figure 3.31 Zeta potential trends illustrating the deposition of the PEs. a) 100 mg of CaCO <sub>3</sub> b) 300 mg of CaCO <sub>3</sub> . ....	72
Figure 3.32 Picture a) & b) showing the particles after LbL without and with GQDs respectively. Picture c) showing the product after core dissolution. ....	72
Figure 3.33 Optical microscope images showing that Y201 MSCs internalize the GQDs-functionalized CaCO <sub>3</sub> microparticles, without showing sign of death, being 70/80% confluent, 24h after the seeding. ....	73
Figure 3.34 Confocal microscope pictures. The two groups of pictures show cells cultured with microparticle and microcapsules, functionalized with GQDs, at different concentrations (0.2 mg/mL and 0.5 mg/mL). Red indicates cytoskeleton; green and blue indicate the fluorescent devices, with excitation-dependent emission. Bar: 40 μm. ....	74

## List of tables

Table 1.1 Different theranostic platforms and their strategy in cancer treatment.....	9
Table 1.2 Various carbon-based QDs source and the respective manufacturing methodology.	22
Table 1.3 Different polyelectrolytes deposited on various substrates through LbL electrostatic assembly.....	27
Table 3.1 Scheme of the chemical bonds and the respective wavenumber.....	47
Table 3.2 Zeta potential values of the GQDs at different pH.....	48
Table 3.3 Ratio between the intensities of vaterite and calcite peaks, obtained after the synthesis, after being immersed 4 h in water and after the adsorption of 3 layers.....	65
Table 3.4 Percentage content of the element constituting the microparticles obtained through different routes and after the functionalization and when the inner core was removed.....	69
Table 3.5 Zeta potential of naked CaCO <sub>3</sub> microparticles at different pH. The results show a high negative charge regardless of the reaction and the pH.....	70

## List of abbreviations

LbL – Layer by Layer  
CaCO<sub>3</sub> – Calcium Carbonate  
Na<sub>2</sub>CO<sub>3</sub> – Sodium Carbonate  
CaCl<sub>2</sub> – Calcium chloride  
QDs – Quantum Dots  
GQDs – Graphene Quantum Dots  
CDs – Carbon Dots  
CdSe – Cadmium-Selenium  
CdTe – Cadmium-Tellurium  
PEs - Polyelectrolytes  
PSS - Polystyrene sulfonate  
PAH - Polyallylamine hydrochloride  
MSCs – Mesenchymal Stem Cells  
SPIONs – Super Paramagnetic Iron Oxide Nanoparticles  
MRI – Magnetic Resonance Imaging  
DOX - Doxorubicine  
PET – Positron Electron Tomography  
HA – Hyaluronic Acid  
DMEM – Dulbecco’s Modified Eagle’s Medium  
DH<sub>2</sub>O - distilled Water  
FTIR-ATR – Fourier Transformed Infrared spectroscopy - Attenuated Total Reflectance  
XPS – X-ray Photoelectron spectroscopy  
EDTA - Ethylenediaminetetraacetic acid  
TEM – Transmission Electron Microscopy  
SEM – Scanning electron Microscopy  
QCM-D – Quartz Crystal microbalance with Dissipation monitoring  
PL – Photoluminescence  
FL – Fluorescence  
UV – Ultraviolet  
UV-Vis – Ultraviolet-Visible  
FA – Folic Acid  
FR – Folate Receptor  
EPR – Enhanced Permeation and Retention  
PEG – Poly ethylene glycol  
MMP – Matrix Metalloproteinases  
RGD – Arginine-Glycine-Aspartate  
NIR – Near InfraRed  
PEI - Polyethylenimine  
ROS – Reactive Oxygen Species  
AFM – Atomic Force Microscopy  
DLS – Dynamic Light Scattering  
PFA - Paraformaldehyde



# Chapter 1. Introduction

---

## 1.1 Cancer

### 1.1.1 Cancer general features

Cancer is a term used to indicate a group of diseases, characterized by abnormal cell growth and the ability to invade other tissues. The latter is the main difference with what is considered a benign tumour. Normally, cells divide, form new cells and replace those which have died. In a malignant tumour this process breaks down: cells tend to survive when they should die but at the same time their proliferation goes on, forming a tissue of damaged and old cells continuously growing (Golub et al. 1999)

Cancers can invade other tissues: this may happen in the area surrounding the mass, or some diseased cells may enter the blood circulation or lymphatic system and start a new tumour in a completely different part of the body, far from the origin. This process is known as Metastasis and the new mass is called metastatic cancer (Figure 1.1). This mechanism is considered the main cause of mortality, so an early detection is necessary to reduce the risks of death of the patient (Choi et al. 2012).

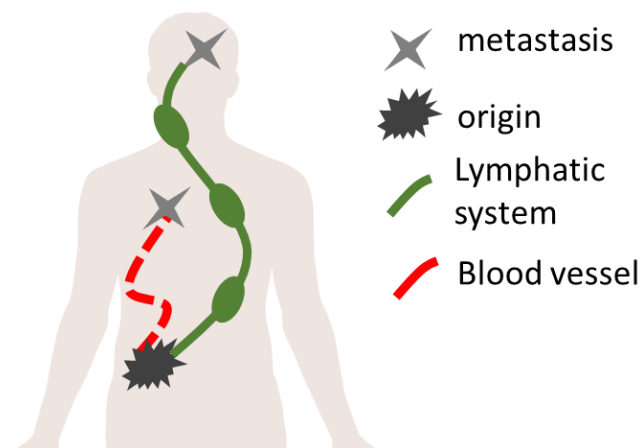


*Figure1.1 Metastasis formation: cancer cells spread through blood vessels or lymphatic system, reaching different areas of the body.*

An important difference between normal and cancer cells is that the latter are less specialized and do not have a distinct and specific function compared to the former, in

fact these do not mature into a specialized tissue.

The main cause of cancer formation is of genetic origin; alterations in the DNA can be inherited from parents but also it can arise during a person lifetime.

These changes affect genes regulating cells' growth and division, as well as the suppression of abnormal proliferation and those genes able to fix DNA damages (Futreal et al. 2004).

### 1.1.2 Cancer Hallmarks

During tumour development, the cells tend to evolve and progressively acquire biological capabilities, enabling growth and metastatic cancer, called Hallmarks, that are the actual requirement for a mass to be considered a malignant tumour (Hanahan and Weinberg 2011) .

These are: *Sustaining proliferative signaling, Evading growth suppressor, Resisting cell death, Enabling replicative immortality, Inducing Angiogenesis, Activating invasion and metastasis* (Figure 1.2).

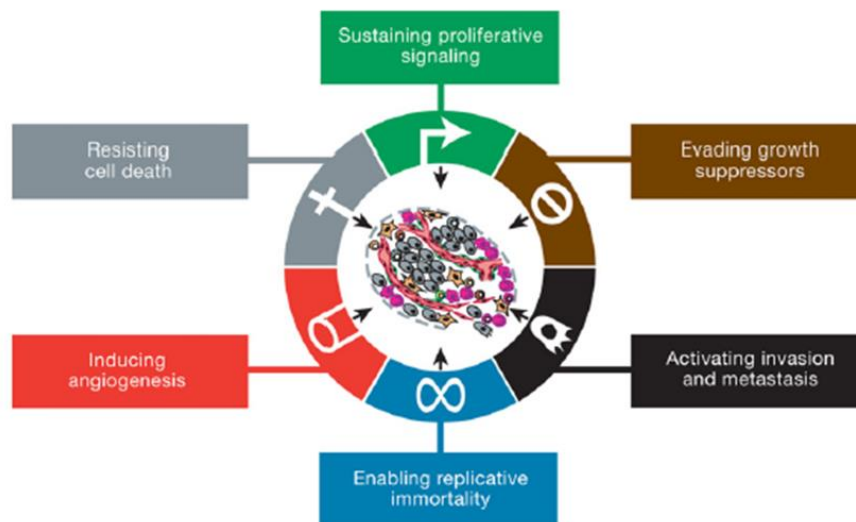


Figure 1.2 The six cancer hallmarks (Hanahan and Weinberg 2011)

The first two are bound together as the first describes how cancer cells sustain a continuous proliferation and the second describes how cancer cells grow in such abnormal way, without stopping and without incurring in those signals supposed to interrupt the cell division.

Moreover, as mentioned before, tumour cells with respect to healthy ones do not tend

to go through apoptosis, because they activate different strategies to avoid programmed death. Healthy cells have a finite number of divisions beyond which chromosomes start to get damaged, so they go through a process that will kill them; tumour cells activate a sort of immortal status, allowing themselves to divide constantly.

The growth of the mass is highly dependent on the surrounding vasculature, so upregulation of angiogenic growth factors and downregulation of inhibitors create an abnormal and disorganized system of vessels surrounding the tumour. In fact, some may lack endothelial cells or basement membranes, and they have fenestrations of higher diameter with respect to a healthy vasculature (Dai et al. 2017).

Finally, as a malignant tumour main feature is the ability to spread, the metastatic process activates initially the invasion of nearby tissues, then through vasculature development cancer cells start moving around the body and settle to form a metastatic cancer.

The new cancer treatments where the research is moving aim to inhibit one of these hallmarks, in order to limit cancer growth and spreading, destroying one of the many pathway that leads to the formation and strengthening of the pathologic tissue (Hanahan and Weinberg 2000).

### 1.1.3 Cancer statistics

Based on demographic and economic data, it's been estimated that by 2030 globally there will be 20.3 million of new cancer cases, compared to 12.7 million in 2008.

Moreover the predicted death rate will rise from 7.6 million in 2008 to 13.2 million by 2030 (Bray et al. 2012).

In UK in 2016 almost 400,000 new cancer cases were registered with a survival rate of more than 10 years of 50% (Figure 1.3). ([www.cancerresearchuk.org](http://www.cancerresearchuk.org))

Given these alarming data, it is very important to find a way to detect cancer at an early stage, before metastasis occurs. So far the technology is not selective enough, having a poor rate of success, although when lung cancer, for instance, is found early the survival rate is 53%, but if this does not happen the percentage decreases to 4% (Choi et al. 2012).

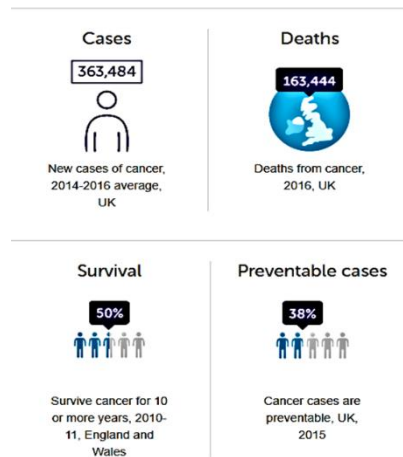


Figure 1.3 UK Cancer statistics  
([www.Cancerresearchuk.org](http://www.Cancerresearchuk.org))

## 1.2 State of the art: New advanced approaches for cancer treatment

### 1.2.1 Theranostic approach

#### Concept and strategies

Nowadays, the research is focusing on the investigations of different strategies to integrate in a single nanometer-sized platform a therapeutic compound and an imaging agent, in order to obtain a specific and more personalised cancer therapy (Y. Ma et al. 2016). The interest is rapidly growing, as demonstrated by the constant increase in publications (Figure 1.4).

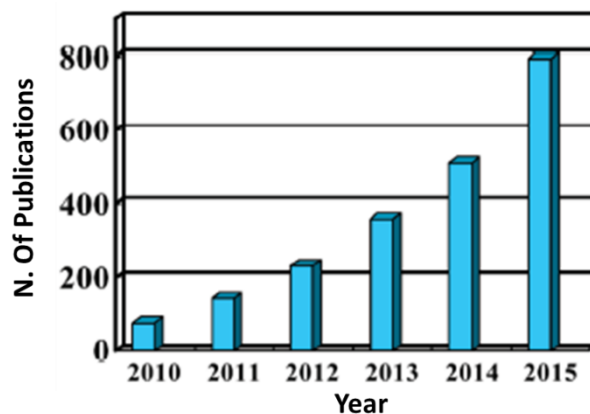
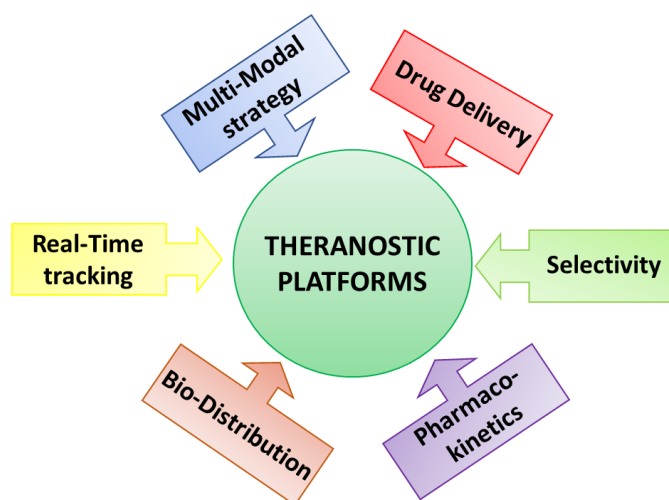


Figure 1.4 Growing number of publications regarding theranostic systems between 2010 and 2015 (Y. Ma et al. 2016)

Most conventional anticancer drugs do not possess the necessary sensitivity and selectivity, fundamental to achieve the desired effect: chemotherapeutics, poorly bio-distributed throughout the body, can affect indistinctly sick and healthy tissue cells, moreover the biggest part is quickly cleared and expelled from the organism, causing the task to not be completely fulfilled. The assumption dose is consequently very low, allowing a small therapeutic window and a low rate of success. (Cui and Wang 2016, Choi et al. 2012, Masood 2016).

The development of nanotechnology in the medicine field allowed the creation of new theranostic platforms which aim to overcome these problems, so to achieve a better selectivity and bio-distribution. Improvements in pharmaco-kinetics are accomplished, managing to overcome drug resistance mechanisms that cancer cells activate in response to chemotherapeutics and conventional therapies (Figure 1.5) (Masood 2016).



*Figure 1.5 Advantages of Theranostic platforms. Improvements in drug delivery and bio-distribution are achieved; it's possible to track the system and to combine various therapeutics in the same vehicle.*

Many researchers have studied the different properties of drug carriers, particularly they investigated several materials and their ability to load a drug and respond to various external stimuli, such as pH change, temperature and light (X. Q. Liu and Picart 2016a).

Polymer nanoparticles, lipid-based systems, metallic, colloidal, amphiphilic are all carriers adopted in nanomedicine. These systems can act as drug carrier on their own,

with a necessary functionalization step in order to impart targeting abilities to them. In other cases, they can be incorporated in bigger vehicles, which cargo will be released *in situ* (Choi et al. 2012).

For example, amphiphilic self-assembled micelles are widely used as drug delivery system, thanks to their hydrophilic and hydrophobic domains; moreover, their nanometer size allow a long circulation and extravasation in tumour tissue. The hydrophobic core is perfect for loading hydrophobic drugs, such as paclitaxel, and the external shell allows blood circulation and potentially targeted delivery.

Natural polymers such as hyaluronic acid, chitosan and chondroitin sulphate are used for manufacturing nano-sized micelles (Sabra et al. 2018).

The theranostic approach brought improvements in all the phases of a therapy: drug delivery and distribution, drug release and clearance; the therapeutic window is larger compared to the conventional therapies, and cancer prevention is better.

Furthermore, the potential to be stimuli-responsive gives the drug carrier the ability to control where and when to release the cargo, or to activate other treatment therapies. Chiu et al (Chiu et al. 2016) loaded doxorubicin onto Carbon Dots functionalized with Folic Acid to actively target cells (Figure 1.6). The loading efficiency was 80%, and the drug release profile was pH dependent: the group investigated the system behaviour at pH 7.4 and 5 in PBS buffer, determining a 62 % release at acidic pH after 72h compared to 25% at physiological conditions.

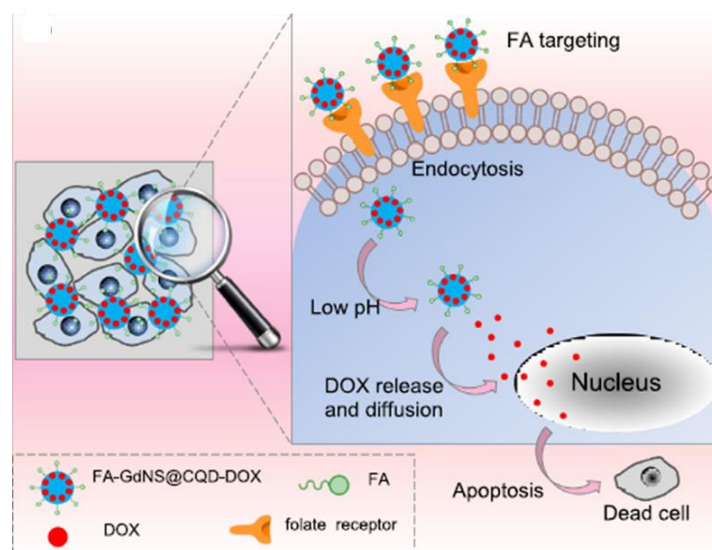


Figure 1.6 Illustration of the pH-responsive drug releasing mechanism of the Folic Acid functionalized theranostic system: when reaching the cancer environment the ligand-receptor interaction allows the internalization of the drug carrier, which releases the cargo thanks to the acidic pH in the cytoplasm (Chiu et al. 2016)

As previously mentioned, a theranostic system includes a therapeutic compound in combination with an imaging probe. In fact, a major challenge is tracking the distribution of the drug carriers in the body: this strategy allows a non-invasive imaging thus to visualize the devices, the body distribution and the mechanism of cellular uptake as well as of drug release (Melancon, Stafford, and Li 2012).

Fluorescent organic dyes have been largely used to follow them, although they do not possess a strong and stable fluorescence and they do not allow a specific and precise tracking having a broad light emission range.

Given these drawbacks, semiconductor quantum dots have attracted a lot of attention as imaging agents, thanks to their tuneable and narrow wavelength light range emission in relation to the radius, their photostability and strong fluorescence (Goryacheva et al. 2015a).

Han et al (Han et al. 2017) fabricated a gemcitabine drug-carrier for pancreatic cancer therapy, functionalizing the surface of CdSE/ZnS core-shell quantum dots, so to track their circulation in *real-time*.

This is an example of how QDs can be used directly as drug delivery vectors, by engineering their surface with various coating strategies; in other studies the QDs are incorporated into the core of a vehicle (Q. Ma et al. 2007) or bound to the nanoparticle surface (Abdelhamid et al. 2018).

Also Magnetic Resonance Imaging (MRI) contrast agents and Positron Emission Tomography (PET) imaging agents have been adopted for applications in theranostic systems.

The theranostic strategy using nanostructures allows also a multi-modal approach, with the purpose to achieve a better result, a more precise selectivity, a better therapeutic window, and an *in vivo* tracking ability (Silva et al. 2019).

The synergistic action of multiple therapeutics and various clinical approaches helps to overcome the drug resistance mechanisms that cancer cells develop; conventional therapies do not assure the arrival of different compounds in the same site, at the same moment and at a good dose to result effective.

Abdelhamid et al (Abdelhamid et al. 2018) combined the effects of two hydrophobic drugs, celecoxib and rapamycin, inside the oily core of a nano-capsule. Their synergistic work would inhibit the exponential proliferation of breast cancer cells, enhancing the

cytotoxicity of the single drugs.

Moreover, the surface of the carrier was functionalized with gelatin conjugated with CdTe QDs as diagnostic agent. A similar principle was adopted by Mattu et al (Mattu et al. 2018) where polyurethane nanoparticles were manufactured and, by exploiting hydrophilic and hydrophobic domains, they co-encapsulated Doxorubicin Hydrochloride (hydrophilic) and Docetaxel (hydrophobic). The results showed a higher accumulation of both the molecules in the cancer environment with respect to the drugs injected without carrier. In this case the imaging properties relied on Iron Oxide nanoparticles for MRI imaging.

When talking about multi-modal strategy, it's important to consider also those platforms that include a therapeutic agent and a clinical approach like hyperthermia or photothermal therapy.

Some theranostic systems have incorporated magnetic particles, which can be targeted following a magnetic field and can also be used for hyperthermia treatment and imaging. For example, Zhang et al used Superparamagnetic Iron Oxide Nanoparticles (SPIONs), that possess targeting abilities, and that can also be used for hyperthermia and even allow a triggered drug release (Ming Zhang et al. 2016).

In the same device, Gold nanoparticles were embedded so to achieve photothermal therapy that significantly enhanced the drug final effect, inducing apoptosis via temperature, as well as targeted delivery and imaging in the Near infrared region.

*In vivo* studies showed an accumulation of the carriers in the diseased area, thanks to the particle size and the active targeting abilities. Bwatanglang et al (Bwatanglang et al. 2016) compared the therapeutic effect of free drug and Folic acid functionalized drug carrier, noticing that in the latter the tumour mass decreased more than if treated with bare drug.

This finding confirmed previous research proposed by Dreaden et al (Dreaden et al. 2014) who managed to specifically target the cancer by exploiting the hypoxic environment and the Hyaluronan-CD44 ligand-receptor interaction. In fact, both *in vitro* and *in vivo* results show a high localization of the nanoplatforms in the tumoral environment, as well as a good cellular uptake thanks to the active targeting approach.

Table 1.1 Different theranostic platforms and their strategy in cancer treatment

DRUG	THERAPY	VEHICLE	IMAGING AGENT	REFERENCE
Gemcitabine	/	CdSe/ZnS QDs	CdSe/ZnS QDs	(Han et al. 2017)
Doxorubicine/Docetaxel	Synergistic action	Polyurethan Nanocapsule	SPIONs for MRI Photoacoustic Imaging	(Mattu et al. 2018)
Celecoxib/Rapamycin	Synergistic action	Polymeric Nanocapsule	CdTe QDs	(AbdElhamid et al. 2018)
DOX	/	PEG-ZnO QDs	ZnO QDs	(Cai et al. 2016)
Paclitaxel	/	Lipid carrier	CdTe/CdS/ZnS QDs	(Olerile et al. 2017)
DOX	PhotoThermia, Photodynamic therapy	Nanoparticle	Photosensitizer (MRI & NIRFI)	(Xue et al. 2018)
DOX	/	Carbon Dots	Carbon Dots & MRI	(Chiu et al. 2016)
5-Fluorouracil	/	Chitosan-Mn-ZnS QDs	Mn-ZnS QDs	(Mohammad et al. 2016)
Paclitaxel	Hyperthermia	PEO-b-PCL nanocapsule	SPIONs/ Gold NPs	(Ming Zhang et al. 2016)
Paclitaxel	/	SiO <sub>2</sub> nanocapsules	ZnSe:Mn/ZnS QDs	(T. Zhao et al. 2017)

### Passive and Active targeting

The main aim of the theranostic approach is a better selectivity, in order to achieve an improved and efficient delivery, avoiding side-effects, as well as to accomplish a better therapeutic result.

The drug carrier requires some features to be actually considered “targeted”: to reach the interested area these systems need to circulate in the vasculature for an extended

period of time; also they have to be able to extravasate and accumulate in the cancer tissue and, finally, be able to release the drug in a controlled period of time, without incurring in burst release (Bae and Park 2011a).

Nanocarriers can reach the interested area in two ways, passively and/or actively, and consequently the drug can be released in the outside cell environment or inside the living cell, after being internalize.

Passive targeting is based on the leaky vasculature typical of a tumour, compared to the one of a healthy tissue (Figure 1.7).

### Passive targeting: EPR Effect

-  Endothelial cell
-  Nanoparticle
-  Cancer cell

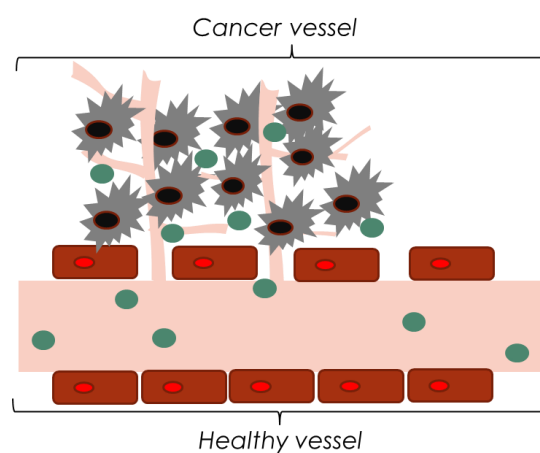


*Figure 1.7 Illustration of the EPR effect: the nanoparticles manage to extravasate and enter the tumor environment thanks to the leaky vasculature, typical of the cancer vessels. A healthy vessel has a compact endothelial wall, prohibiting the particles' passage.*

The latter has in fact a very compact endothelial tissue, slightly porous, which does not allow particles to pass through, while cancer tissue blood vessels are more porous, with interstitial spaces ranging from 100 nm to 800 nm, permitting the accumulation of nanocarriers in the tumoral environment. Moreover, a very slow and weak clearance helps the retention of the drug carrier. It has been proved that smaller particles (50 ÷ 300 nm range) tend to avoid more easily the clearance (Bae and Park 2011a), compared to bigger ones.

This concept is called Enhanced Permeation and Retention (EPR) Effect.

For instance Feng et al (Feng et al. 2016) fabricated a carbon dots (CDs) – based drug delivery system coated with negatively charged PEG that allows a longer circulation time, avoiding clearance by the immune system and, at the same time, preventing a premature cell internalization. The CDs manufactured have an average diameter of

7nm. This platform is able to convert its surface charge in response to the more acidic pH in tumour extracellular environment. In fact, it's been proven that the external charge plays an important role in order to enhance the cellular uptake of the nano-carriers, being the cell membrane highly negative (around -70mv): studies have indeed focused to impart a positive charge to the particles (Poon et al. 2011).

PEG has been widely used as antifouling agent, allowing a longer blood circulation time, without getting eliminated by the immune system.

Moreover it's cleavable at acidic pH and good for further functionalization thanks to its surface chemical groups (Xue et al. 2018).

The second approach to enhance the selectivity of carriers is the Active Targeting which uses active ligands, bound on the surface of the nano-vehicles, in order to precisely target the diseased cells with more specificity (Figure 1.8). The particles are in this way able to enter the cells and release the cargo directly into the cytoplasm or the nucleus.

#### Active targeting: Ligand-receptor interaction

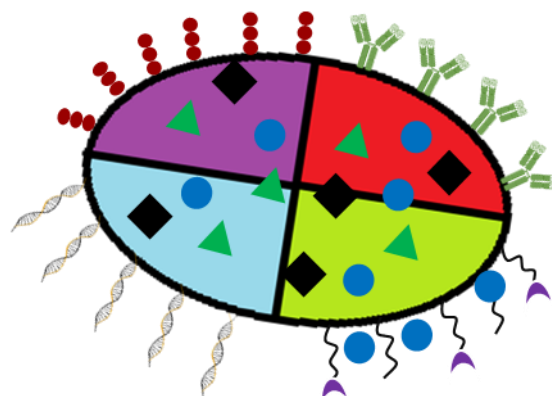
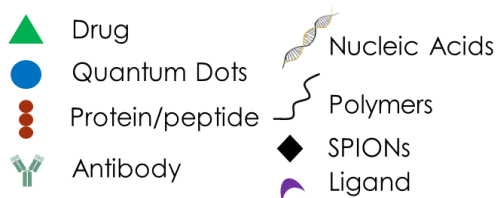


Figure 1.8 active targeted nanoparticle. The surface can be functionalized with peptides, antibodies, nucleic acids, polymers and ligands. Therapeutic compounds and imaging agents can be loaded into the carrier or deposited on the external surface.

It has been demonstrated that a ligand-conjugated nanoparticle is facilitated to reach the tumour extracellular environment and, successively, enter the cell with respect to a carrier not functionalized (Cai et al. 2016).

From a general point of view, cells express on their membrane different receptors, proteins, antibodies, peptides; this expression varies according to the type of cell and, specifically, cancer cells over-express specific receptors: these peculiar features can be exploited, so to avoid non-specific binding (Masood 2016).

Ligands can be peptides (Han et al. 2017), antibodies (Melancon, Stafford, and Li

2012), polysaccharides (AbdElhamid et al. 2018), Folic acid (T. Zhao et al. 2017) and other biological molecules.

These surface functionalization strategies enhance the cellular uptake of the drug carrier. As example, Bwatanglang et al (Mohammad et al. 2016) noted that cell viability decreased when the membrane expressed Folate receptor (FR), ligand good for binding with Folic acid (FA), which they functionalized nanoparticles with. They suggested that the superior cellular uptake of breast cancer cells expressing FR was causing the cell viability to decrease with respect to normal cells not expressing FR.

Furthermore, common use in research is the interaction exploitation between Hyaluronic Acid (HA) and CD44; at this regard Al-Nahain *et al* (Abdullah-Al-Nahain et al. 2013) delivered Doxorubicin by conjugating it onto Graphene QDs, functionalized with Hyaluronan, able to bind to overexpressed CD44 receptor of cancer cell lines.

Another widely used targeting ligand is biotin, able to recognize biotin receptors over-expressed by cancer cells (Iannazzo et al. 2017). The functionalisation resulted in an enhanced cellular internalization, with consequent drug release inside the cell.

Finally, the combination of both passive and active targeting would improve the drug delivery, imparting different properties to the vehicle. For instance Han et al (Han et al. 2017) have coated nanoparticles with an external PEG layer, allowing long circulation but, when tumour tissue is reached, Matrix Metalloprotenases (MMPs) would shield the PEG layer so to expose the Arginine-Glycine-Aspartate (RGD) peptide, used as active targeting ligand.

## 1.2.2 Quantum dots

Quantum Dots (QDs) are defined as semiconductor nanostructures, *discovered in 1981* but used for the first time in biomedical imaging in 1998.

These devices have very peculiar optical and electronic properties, which allow them to be used for solar cells, computing and as imaging probes like LEDs, photodetectors and in bioimaging (Matea et al. 2017).

Semiconductor materials are described by the band theory: they have a Valence Band, a Conduction Band and a Band Gap (Figure 1.9) (Jasieniak, Califano, and Watkins 2011). When a photon hits the quantum dot, the energy gain will cause the electron to jump from the valence band to the conduction band, leaving a hole where it initially was and generating an electron-hole pair. When the hole and the electron recombine, a photon is emitted, at a wavelength proportional to the size of the band gap (Freeman and Willner 2012).

The small size of the particle allows the energy band levels to be quantized, giving them atom-like properties, which makes the tuning of the optical properties possible in relation to the diameter of the quantum dot (Matea et al. 2017).

This is known as Quantum Confinement Effect.

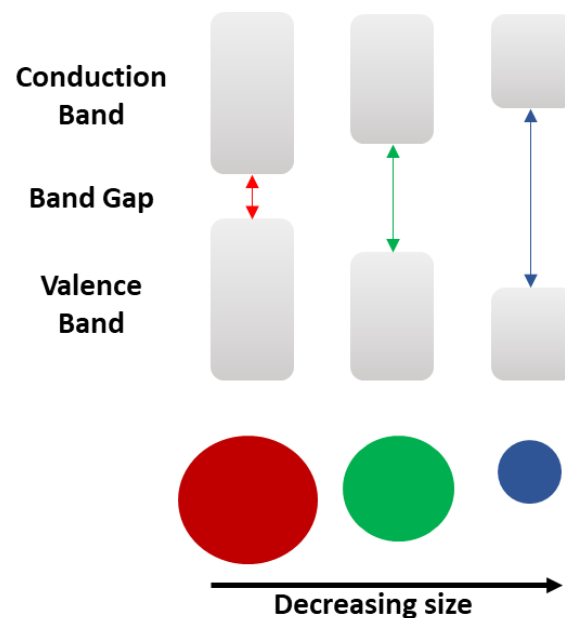


*Figure 1.9 Band Theory of semiconductor materials, Quantum Confinement Effect and light emission mechanism. As the QD diameter decreases the Band Gap Increases, emitting more energetic photons.*

The higher is the diameter, the smaller is the band gap, so the energy (light) emitted is less or at higher wavelength and there is a shift towards the red of the spectrum. On

the other hand, the smaller is the diameter, the wider is the band gap so the energy required to the electron to jump in the conduction band is higher, and consequently more energetic, or at a lower wavelength, will be the photon emitted (shift towards the blue of the spectrum) (Jasieniak, Califano, and Watkins 2011).

The main semiconductors used to produce Quantum dots are Cadmium, Selenium, Tellurium and they can have a single core structure or a core-shell structure. The former is easier and quicker to synthesize, although there might be surface defects that can cause energy 'leaks' (Cao et al. 2013) affecting the quality of the light emission; the latter provides some advantages, such as a higher quantum yield, solving the problem previously described, superior photoluminescence and protection against the environment.

Another solution to enhance the semiconductor QDs properties is doping them with metallic ions such as Manganese ( $Mn^{2+}$ ) or Cadmium ( $Cd^{2+}$ ) that would improve the nanoparticles fluorescence abilities as well as avoid self-quenching effect (Mohammad et al. 2016).

Derfus et al (Derkus, Chan, and Bhatia 2004) showed that by capping CdSe semiconductor quantum dots, highly toxic if subjected to oxidation, with ZnS shell, the cell viability increased, without affecting the fluorescence properties. The functionalisation acts as a protection against the oxidative environment, but it does not eliminate completely the toxic effect under UV-light.

On one side, semiconductor quantum dots have very attractive optical and electrical properties, on the other hand they have an inherent toxicity, due to their heavy metal composition.

This drawback limits their application in the biomedical field as imaging probes. In fact, these materials tend to release free radicals that causes cell death, hence their cytotoxicity (Chiu et al. 2016).

Cadmium is a heavy metal commonly used to fabricate semiconductor quantum dots, in conjugation with Tellurium or Selenium (CdSe, CdTe) or other metals. As mentioned previously, these nanocrystals are not biocompatible, as Cd<sup>2+</sup> ions tend indeed to accumulate in the liver. Moreover, if illuminated by UV light the cell viability decreases as function of both QDs concentration and UV exposure time (Figure 1.10) (Derfus, Chan, and Bhatia 2004).

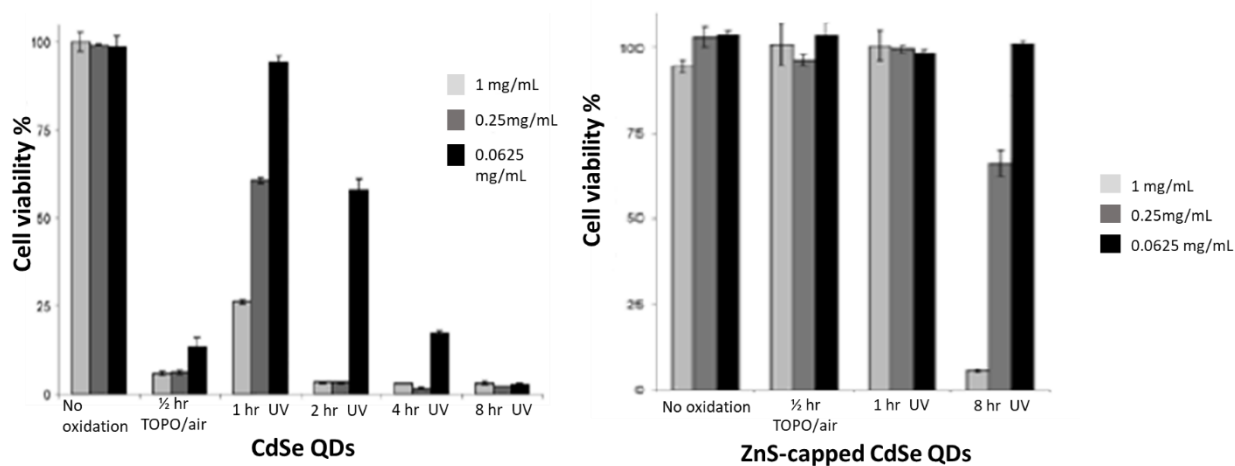


Figure 1.10 Cell viability comparison between bare CdSe and ZnS-capped CdSe: when coated the QDs' cytotoxic effects decrease. The UV exposure increases the ROS production, decreasing the cell viability (Derkus, Chan, and Bhatia 2004).

Currently bioimaging is mainly performed via organic dyes, that bind to a specific biological molecule, so to color it.

These fluorophores show a broad wavelength emission range and an instable fluorescence: consequently, the emission spectra of these staining tend to overlap, limiting the number of different fluorophores present in the same sample. Organic dyes also suffer of photobleaching and the self-fluorescence of some tissue may interfere with the detection (Sharma et al. 2006).

With their size-tuneable emission, semiconductor QDs have improved this aspect showing a broad absorption wavelength range, so nanoparticles with different sizes can be excited by the same light, but would emit at different wavelengths (Nair et al. 2017).

The simultaneous detection of various analytes is an important target that research is trying to accomplish since organic fluorophores (FITC, GFP and others) do not allow this application.

Through LbL assembly Qiang *Ma et al* (*Q. Ma et al. 2007*) created multicolor microspheres, functionalized with different antigens, able to recognize specific antibodies: two types of CdTe QDs emitting at different wavelength, 600nm (orange) and 650nm (red), are incorporated onto the surface of polystyrene microparticles for immunoassays. The strength of this device is the ability to emit at the same time three different wavelengths at 520 nm (FITC), 600 nm and 650 nm (QDs), when excited with the same light at 488 nm.

Semiconductor QDs have also been embedded in a single system with the purpose to improve their fluorescence and increase the emission intensity (Constantine et al. 2003); they have also been largely used in studies concerning drug delivery system, as carrier themselves or as imaging probes belonging to a bigger platform (Bwatanglang et al. 2016; Cai et al. 2016).

### Carbon-based nanostructures

The drawbacks of Semiconductor QDs, such as their cytotoxic effect, have pushed the research to look for new and biocompatible systems for imaging living organisms.

Recently, nanoscale configurations of carbon have gained a lot more attention, thanks to their biocompatibility and their luminescent properties comparable, if not better, to those of semiconductor quantum dots (Lim, Shen, and Gao 2015; Ding, Zhu, and Tian 2014).

The latter have been, and still are, a huge topic of research given their wide applicability and versatility, but particularly their tuneable optical properties, good for biosensing and bioimaging. Unfortunately, their metallic core induces cytotoxic effects, damaging tissues and prohibiting clinical applications.

To tackle this fundamental problem, but obviously to maintain the same qualities, carbon-based nanostructures have been widely investigated. These materials exist in various morphologies and they are fullerenes, nanotubes, nanohorns, nanodiamond, nanodots and graphene derivatives (Figure 1.11).

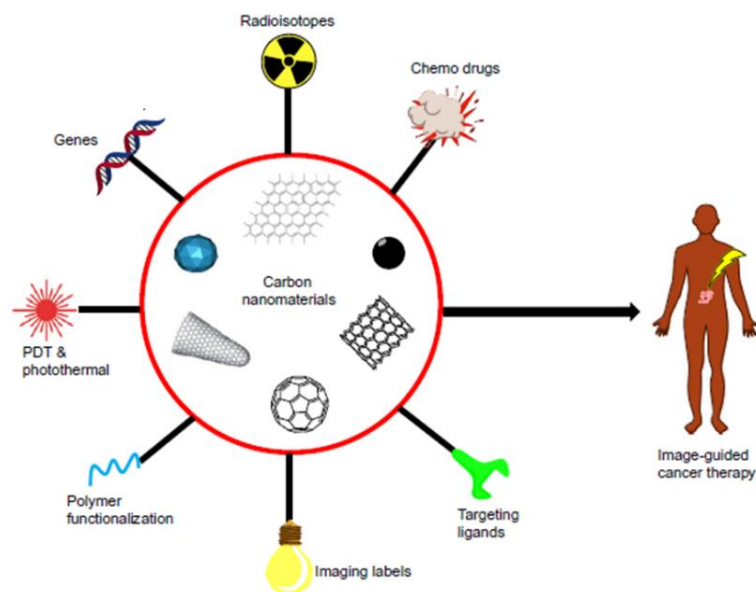


Figure 1.11 Different Carbon-based nanomaterials and the potential applications (Chen et al. 2015)

Being carbon-based, these materials requires a functionalization or passivation step in order to impart them hydrophilic moieties, so being accepted by the whole organism, and enhance their fluorescence qualities (Ding, Zhu, and Tian 2014a). Carbon nanotubes are intrinsically able to emit light because of the presence of energy bandgaps dependent on their diameter (Cao et al. 2013), this is why their fluorescence abilities have been largely used in Biomedicine and cancer detection, compared to the fullerenes which most used imaging method is the MRI (D. Chen et al. 2015). Moreover, they can be used in photothermal therapy (PTT) of cancer, given their absorption in the infrared or near Infrared. These different structures are also a great tool for delivery a cargo, especially a drug, to a specific destination, creating a biocompatible theranostic system, thanks to their large surface area and surface functional chemical groups good for embedding biomolecules and for covalent bindings.

### Carbon and Graphene Quantum Dots

Graphene quantum dots (GQDs) and Carbon Dots (CDs) are zero-dimensional carbon structures with fluorescent properties, as well as water solubility and photostability (Lim, Shen, and Gao 2015) and like semiconductor QDs, their optical properties are related to quantum confinement effects.

Their light emission has been widely studied by many researchers, who suggested two different emission mechanisms: bandgap transitions between conjugated  $\pi$ -domains and surface and edge defects on the particles (Lim, Shen, and Gao 2015; Zheng et al. 2015; Cao et al. 2013).

The former is based on the creation or induction of isolated  $sp^2$  islands in order to exploit bandgap transitions between  $\pi$ -electrons. To this regard, a single graphene sheet is not photoluminescent because connections between  $\pi$ -domains in  $sp^2$  islands tend to quench any emission; if it gets cut in smaller nano-sized pieces, the quantum confinement and the features above mentioned would make them fluorescent (Cao et al. 2013; Z. Wang et al. 2016).

The latter relies on non-perfect  $sp^2$  and  $sp^3$  domains that act as energy traps able to absorb and release light. Together these two mechanisms make carbon-based QDs useful as imaging tools in various applications.

However, the quantum confinement has not been completely defined for this class of material. What is clear, is that the final product is often very heterogeneous for what concerns the size, consequently GQDs and CDs properties are highly influenced from the fabrication procedure (Zheng et al. 2015).

Both nanoparticles have surface functional groups and defects that depend on the synthetic procedure, which can consequently affect their morphology and physicochemical properties (Figure 1.12) (Zheng et al. 2015; Cao et al. 2013).

An important feature that makes them attractive for application in biomedicine is the ability to emit in the Near Infrared (NIR) region which is the wavelengths range where

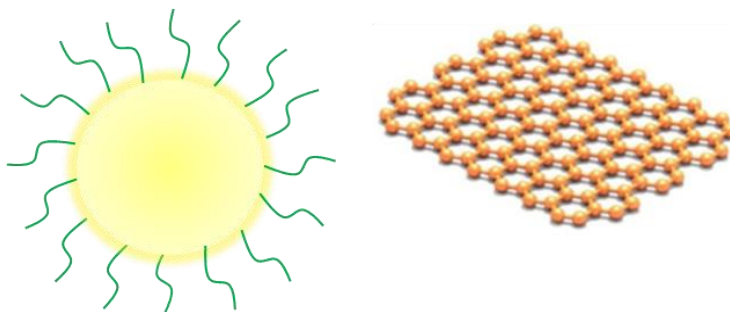


*Figure 1.12 Carbon Quantum Dot, sphere-shaped with surface passivation to enhance fluorescence. Graphene Quantum Dots with the peculiar honeycomb structure like graphite.*

the light has its maximum depth of penetration in tissues (Sharma et al. 2006).

Another interesting aspect of both nanoparticles is their excitation-wavelength

dependent emission spectra: compared to semiconductor QDs, that emit different colors in relation to their radius, carbon-based materials change emission in response to the exciting light (Figure 1.13 a).

However, uniform sized GQDs have been synthesized and they do not possess excitation wavelength dependent photoluminescence (Mo Zhang et al. 2012;Chiu et al. 2016).

Also, Iannazzo et al (Iannazzo et al. 2017) achieved a similar result, suggesting that the like semiconductor QDs, the uniform size would limit the emission wavelength range.

In fact, when exciting with light ranging from 340 nm to 410 nm, the emission remained unshifted (Figure 1.13 b).

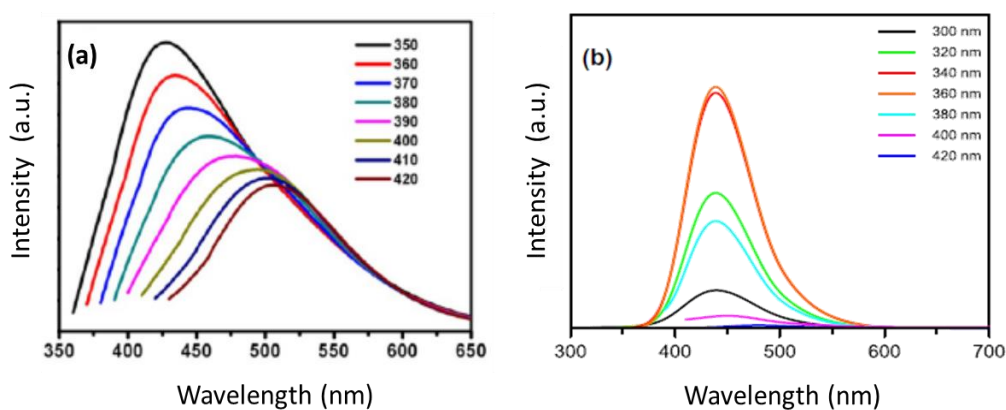


Figure 1.13 Photoluminescence spectra of carbon-based QDs. a) excitation-dependent emission (Nair et al. 2017) b) excitation independent emission (Chiu et al. 2016)

In literature is possible to find red (Zifei Wang et al. 2017), blue (Pan et al. 2010), yellow (Mo Zhang et al. 2012), green (Lei Wang et al. 2014) emitting carbon-based QDs; although the same quantum dot is able to emit at different wavelength, even when phagocytosed by a cell (S. Zhao et al. 2015) (Figure 1.14).

CDs and GQDs possess similarities, especially chemically, but they are structurally dissimilar, being the first quasi spherical particles, while the second are quite similar to graphene sheet, although they can have more than one layer (Zheng et al. 2015).

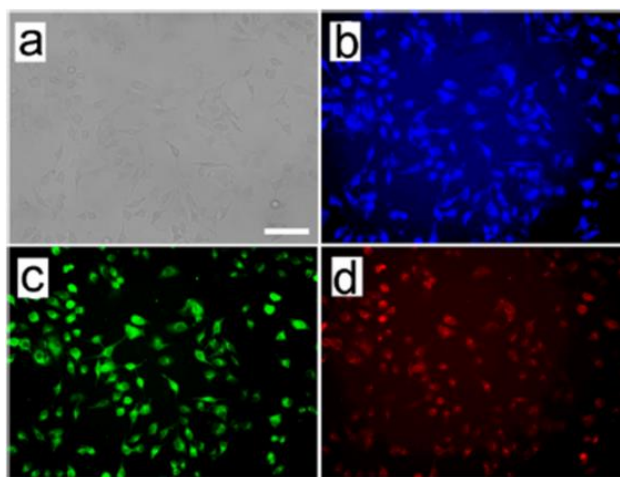


Figure 1.14 CDs internalized by cells and excited at different wavelengths. a) brightfield image b) 330-385 nm c) 450-480 nm d) 510-550 nm. Scale bar: 50  $\mu\text{m}$  (S. Zhao et al. 2015)

The synthetic routes to obtain Carbon Dots and GQDs are basically two: Top down and Bottom up (Figure 1.15).

The first one consists into cutting large carbon domains into smaller particles, starting from graphene sheets (Pan et al. 2010), graphene oxide (Nair et al. 2017a), carbon fibres (Abdullah-Al-Nahain et al. 2013), carbon nanotubes (MWCNT) (Iannazzo et al. 2017) and other precursors.

The Bottom Up route is conducted by pyrolysis or carbonization of organic molecules, such as citric acid (Pierrat et al. 2015a) or glycerol (C. Liu et al. 2012).

However, these methods do not allow a large-scale production and cannot assure a narrow size distribution; moreover, these cannot guarantee the quality of the produced particles regarding edge and surface defects, which influence the final optical and electronic properties of the QDs (Liang Wang et al. 2016a).

Furthermore, bare CDs possess a relatively weak light emission, compared to semiconductor QDs and GQDs, but through a surface passivation step, usually conducted after the nanoparticle synthesis, their fluorescence is sensibly enhanced (Cao et al. 2013).

Many researchers in order to improve the optical properties and at the same time optimizing the synthesis of CDs, have proposed a single step synthetic approach, which saves time imparting different moieties to the nanoparticles during the fabrication process. For instance, Liu et al (C. Liu et al. 2012) manufactured CDs passivated with Polyethylenimine (PEI) through microwave assisted pyrolysis of Glycerol in the

presence of PEI. In this way time was saved, the produced nanoparticles are already passivated and possess bright and excitation-dependent fluorescence, good for biolabeling.

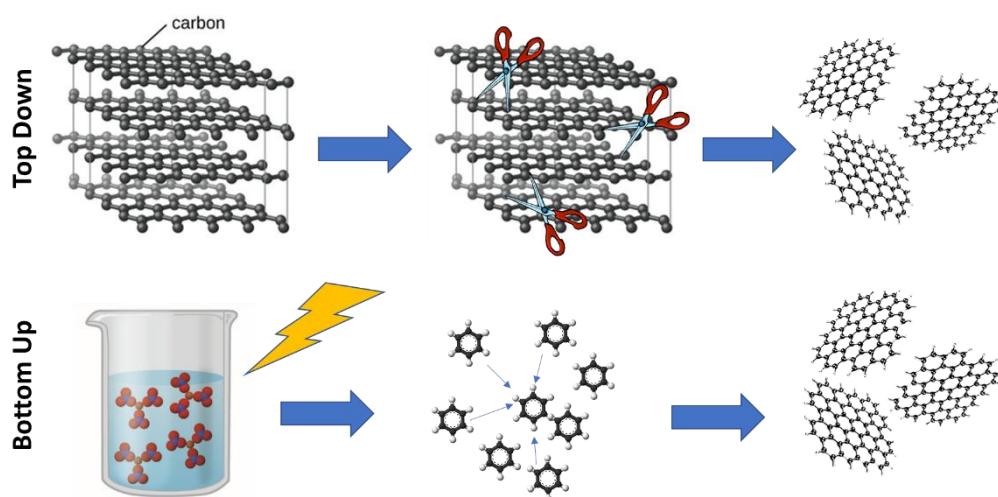


Figure 1.15 Schematic illustration of Top Down and Bottom Up methods. The former uses a large carbon source that gets cut in small nanostructures. The latter begins from an organic precursor, irradiated with energy that leads to nucleation and synthesis of QDs.

Different agents have been consequently used to functionalize these particles, PEG<sub>1500N</sub> (Anilkumar et al. 2013), polyallylamine (PAA) and PropionylEthyleneImine-co-EthyleneImine (PPEI-EI) (Y. Wang et al. 2011).

Wang et al (Zonghua Wang et al. 2013) have passivated green-emitting GQDs with PEG, in order to enhance their PhotoLuminescence (PL), obtaining a final quantum yield of 18.8%. They also demonstrated that by binding PEG, the surface area increases, which would make the nano-particles able to load high amount of drug. Moreover, PEG improved their solubility and without it, the emission peaks did not move but decreased in intensity. Other studies demonstrate the high internalization of these systems, but the PEI and PPEI-EI passivation increase the cytotoxic effect (Y. Wang et al. 2011).

A new wave of synthetic routes, so called “Green Routes”, consists in a combination of the two approaches, bottom up and top down, while starting from food waste such as rice husk, garlic or coffee. The basic idea is to create sp<sup>2</sup> carbon sheets via bottom up

method and subsequently cut them into QDs via top down (Zhaofeng Wang et al. 2016).

This procedure avoids the use of toxic reagents, thus being completely environmentally friendly.

As said before, the synthetic process applied to fabricate carbon quantum dots influences the final properties of the product: electrochemical, sonochemical, hydrothermal approaches have been applied in the production (Table 2).

The properties that these different methods influence are especially the surface functional groups of the particles, which can make them water soluble or more or less good for further functionalization.

*Table 1.2 Various carbon-based QDs source and the respective manufacturing methodology.*

<b>PRECURSORS</b>	<b>METHODS</b>	<b>REFERENCE</b>
Citric Acid	Thermal Pyrolysis	(Feng et al. 2016)
Citric Acid & bPEI25k	Microwave pyrolysis	(Pierrat et al. 2015a)
Glycerol & bPEI25k	Microwave Pyrolysis	(C. Liu et al. 2012)
MWCNT	Acid Exfoliation	(Iannazzo et al. 2017)
Graphite	Electrochemical	(Mo Zhang et al. 2012)
Coffee	Hydrothermal	(Liang Wang et al. 2016a)
Garlic	Hydrothermal	(S. Zhao et al. 2015)
Rice husk	Hydrothermal	(Zhaofeng Wang et al. 2016)
Graphene Oxide (GO)	Photo-Fenton reaction Sonochemical	(Wu et al. 2013a); (Nair et al. 2017a)

For instance, via hydrothermal method, QDs were synthesized from rice waste and thanks to the introduction of oxygen containing groups, like epoxide, these carbon dots show very good aqueous stability long term: it has been proven that there is no sign of precipitation after 3 months of water dispersion. The PL properties are also largely affected by reagents and temperatures: quantum yield and the color emission

depends on it (Lei Wang et al. 2014).

Zhang et al (Mo Zhang et al. 2012) fabricated GQDs of 5 to 10 nm average size, adopting an electrochemical method. Starting from graphite electrolysis first and then treating the product with hydrazine hydrate at room temperature, they produced uniform sized, water soluble and yellow fluorescent nanoparticles: these properties have been associated with the creation of hydrazide groups on the surface, as consequence of the reduction of oxygen-containing groups. The hydrazide groups act as light absorbers and do not allow an excitation-dependent emission, alongside the uniform size, but allow a stable and strong photoluminescence.

GQDs, given to their extraordinary properties, have an enormous potential in the biomedical field as imaging probes alone or in a theranostic system in anticancer therapies.

These carbonaceous materials are perfectly suited for application in nanomedicine, in combination with therapeutic compounds: their high surface-area, mechanical strength, photoluminescence and possibility to be chemically modified attract lot of interest (D. Chen et al. 2015).

GQDs can enter the cell, accumulate in the ER and eventually getting inside the nucleus, given the fact that the ER is a contiguous with the nuclear membrane. It's been also proven that the main pathway that GQDs take to pass through the cell membrane is via caveolae-mediated endocytosis, finally also entering the nucleus (Wu et al. 2013a). Furthermore, it was assessed the cytotoxicity of GQD, comparing them with graphene oxides sheets, via flow cytometry and MTT assay: the former is less toxic, due to a lower introduction in the cells of Reactive Oxygen Species (ROS), compared to the latter (Wu et al. 2013a).

Surface functionalization of CDs and GQDs is an attractive strategy to impart targeting moieties to the nanocarriers, and surface-active groups make this approach particularly suitable. Nahain et al (Abdullah-Al-Nahain et al. 2013) functionalized GQDs by conjugating them with HA, so to actively target cancer cells via CD-44 ligand-receptor interaction. The HA was previously conjugated with Dopamine so to improve the anchoring between the nanoparticles and the Glycosaminoglycan (GAG): by analysing confocal microscope images, the group assessed that the functionalization improves dramatically the cellular uptake of the GQDs, particularly for cancer cell lines.

Drugs like Doxorubicin (DOX) have been loaded onto the particles, conjugating through electrostatic and hydrophobic interactions (Chiu et al. 2016). Cell viability assays were conducted to understand the cytotoxicity of bare GQDs, functionalized GQDs and drug loaded: concentration dependent toxicity was demonstrated as well as the efficacy of DOX loading and release.

### 1.2.3 Layer by layer technology

#### General features and different LbL-based technologies

Surface chemical modification is a very important step in order to improve a substrate optical, electrical and mechanical properties, as well as biomaterials and medical devices interaction with the surrounding environment and consequently their performance, without affecting other tissues (Joseph J. Richardson et al. 2016).

A procedure that has received a lot of interest in the past few decades is the Layer by Layer (LbL) assembly, a process based on the alternative deposition of polyelectrolytes (Pes), oppositely charged, creating on a substrate surface nanofilms of controlled thickness (Figure 1.16). These materials have indeed an electrolyte group that, following its dissociation in water, imparts them a charge, positive or negative.

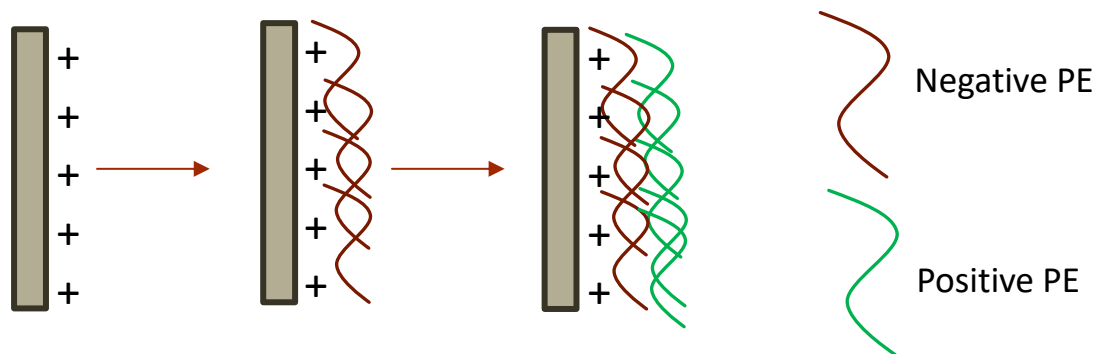


Figure 1.16 Alternative deposition of oppositely charged polyelectrolytes on a pre-charged substrate

In a general LbL process, a pre-charged substrate is immersed in the oppositely charged PE which is adsorbed on its surface in small quantity. This is followed by a washing step in water, to remove any unbound polymer and to avoid cross-contamination between the solutions. Subsequently the material is dipped in the solution of the second PE, creating the first bilayer and then again in water. This procedure is repeated as many times as number of bilayers are required (Figure 1.17).

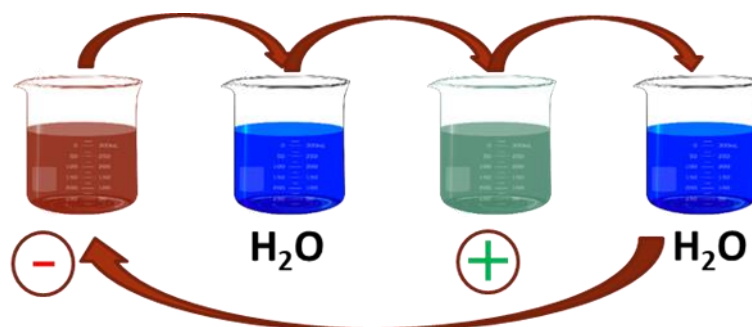


Figure 1.17 Illustration of the Immersive Layer by Layer

The simplicity and versatility of this procedure is what makes it particularly attractive, confirmed also by the numerous fields in which it is utilized: catalysis, optics, energy, membranes and biomedicine (J. J. Richardson, Bjornmalm, and Caruso 2015). The layers deposited have a controlled thickness in the nanoscale, which ensure the efficacy of the functionalization without sensibly affecting the substrate size.

The kinds of substrate that can be coated by electrostatic LbL are different: planar and curved ones, micro and nanoparticles and fibers as well.

For instance, Xiankai Li et al (X. Li et al. 2018) engineered spider silk fibers by alternating deposition of positive Bovine Serum Albumin (BSA) and negative Graphene sheats, in order to create a motion and humidity sensor, sensitive to the smallest vibrations, able to translate those mechanical stimuli in electrical signals.

In another work Gai et al (Gai et al. 2018) used a Polystyrene substrate, moulded on a PDMS master, as a sacrificial template on which oppositely charged materials are deposited to generate a free-standing self-assembly structure.

There are different factors influencing the final output of the LbL deposition and the multilayer growth. For example Chai et al (Chai et al. 2017a) coated PLGA nanoparticles with multilayers of Chitosan and Alginate, deposited by dissolving the sphere in solutions of the PEs, and washing through various centrifugation cycles.

They assessed the amount of bound PE in relation with the adsorption time, determining that after 20 minutes the remaining alginate in the supernatant is the less.

They have also studied the coating weight changing PE concentrations, NaCl molarity and temperature, reporting that multilayer growth increases with polyelectrolyte concentration as well as NaCl concentration and that at physiological temperature the

deposition achieves better results than lower temperature. The solutions' pH is an important parameter that would influence the layer thickness, and an increase or a reduction in pH depending on the polyelectrolyte charge density would change the ionization state of the polymers (Saqib and Aljundi 2016).

The versatility is also extended to the kind of materials deposited, with respect to the application: polymers, proteins, lipids, nucleic acids, nanoparticles can all be used as surface coatings.

*Table 1.3 Different polyelectrolytes deposited on various substrates through LbL electrostatic assembly*

<b>POSITIVE</b>	<b>NEGATIVE</b>	<b>SUBSTRATE</b>	<b>REFERENCE</b>
BSA	Graphene sheats	Silk fibers	(X. Li et al. 2018)
Chitosan	Alginate	PLGA NPs	(Chai et al. 2017a)
PEI, Chitosan, PLA	siRNA	Polystyrene NPs	(Z. J. Deng et al. 2013)
PLL	Hyaluronan (HA)	Polystyrene NPs	(Dreaden et al. 2014)
PAH	PSS	CaCO <sub>3</sub> MPs	(Volodkin et al. 2004)
PLL/Chitosan	HA/Dextran Sulfate/PAA	Polymeric NPs	(Morton et al. 2013)
PAH	PSS & CdTe QDs	Polystyrene NPs	(Q. Ma et al. 2007)
PEI/Chitosan	CdTe/oligodeoxyynucleotide	MWCNT	(Jia et al. 2007)
PLL	CdSe/PSS	Polyacrolein MPs	(Generalova et al. 2011)

Deng et al (Z. J. Deng et al. 2013) engineered polystyrene nanoparticles for cancer treatment by alternating the deposition of negatively charged siRNA and a polycation (Figure 1.18). The group studied different combination, in order to exploit the gene and drug delivery: Polyethyleneimine (PEI), Chitosan, poly-β-amino ester and poly-arginine were all investigated, finding in the last one the best siRNA loading.

Also, different works exploited the charge of nanoparticles, depositing them on different substrate for various applications like biomedicine and chemistry (Ghosh and Bürgi 2013; Constantine et al. 2003).



Figure 1.18 A) Scheme of the drug-loaded nanoparticle coated through LbL, using siRNA as polyanion and various materials as polycation. B) TEM images clearly showing the core-shell structure. (Deng et al. 2013)

The big drawback of this methodology is the fact that is very time-consuming and operator dependent: scaling up the process and advancing to automated systems is being an important research topic in this decade (J. J. Richardson, Bjornmalm, and Caruso 2015).

These limitations pushed the research groups to find new tools that aim to manufacture multilayer nanofilms on different-shaped surfaces, but in a quicker and more reproducible process. These methods can be summarized in 4 categories: Spray, Spin, Electromagnetic and Microfluidic Layer by Layer.

A new strategy to deposit oppositely charged PEs on substrate is spraying the materials directly on the surface, alternating each step with a washing one spraying deionized water (Figure 1.19).

This technique is much faster than the dip coating method, allowing the deposition for just few seconds compared to the minutes of the other approach. (Dierendonck et al. 2014; J. J. Richardson, Bjornmalm, and Caruso 2015)

The results are very similar to those obtained with the more used immersive LbL, covering the surface homogeneously and almost instantly, and it has demonstrated that even without washing is possible to obtain well organized and regular multilayers, although the rinsing step makes them thicker, probably due to a sort of rearrangement of the polymer chains (Dierendonck et al. 2014; J. J. Richardson, Bjornmalm, and Caruso 2015).

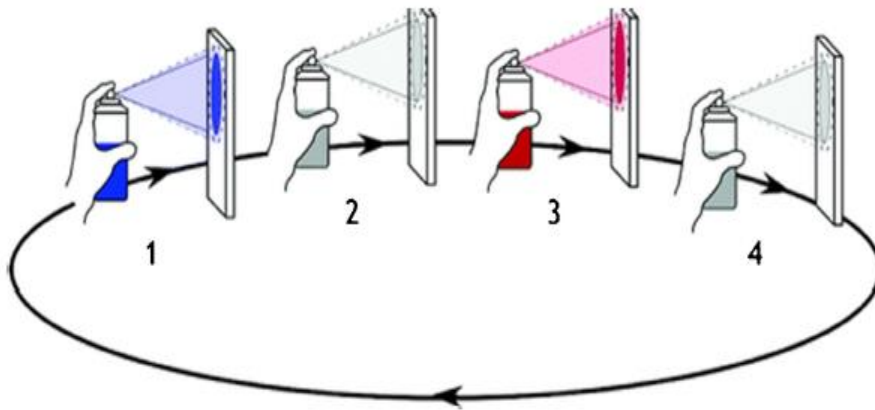


*Figure 1.19 Scheme of the Spray LbL technique (Saqib and Aljundi 2016) . Steps 1 and 3 illustrate the polyelectrolytes deposition, while steps 2 and 4 the rinse passages.*

Morton and coworkers (Morton et al. 2013), for example, used the spray technique to coat PLGA nanoparticles stored on a planar polyester support film, depositing Hyaluronan and PLL. Each deposition step took only 3 seconds, with 3 seconds of washing. The film deposition was confirmed by Atomic Force Microscopy (AFM) and Dynamic Light Scattering (DLS), that showed the maintenance of particle shapes with an increase in height of ~5 nm. Moreover, they observed that a conformal coating surrounding was achieved around the entire NP, even if a side of the particles was not accessible.

Spray technique can also be used in combination with the dip-coating method (Gai et al. 2018), but as already demonstrated by many different researches, the advantage of the latter is the quick polyelectrolyte deposition and rinsing (seconds) compared to the other method (minutes).

The Spin LbL is an innovative approach consisting into using a spin coater to rapidly rotate the substrate on which the polyelectrolyte sequence is injected. This allows a very quick film deposition, in the order of seconds (J. J. Richardson, Bjornmalm, and Caruso 2015; Vozar et al. 2009; Saqib and Aljundi 2016).

The structure that the spin LbL allows to achieve are highly organized in comparison with the traditional dip coating process and the spray technique (Figure 1.20).

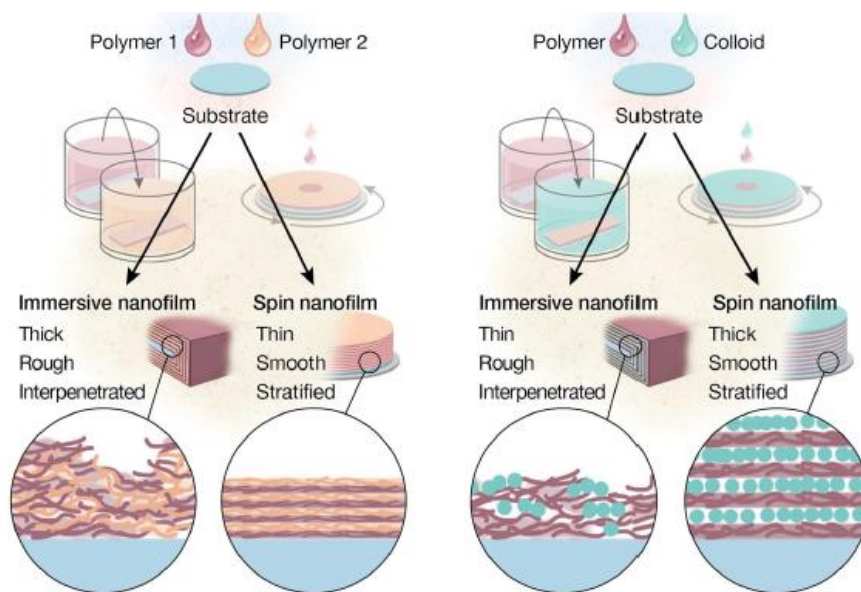


Figure 1.20 Comparison between the layer deposition in the immersive and Spin LbL. The former creates a disorganized structure in which the polyelectrolytes mix together. The latter instead creates a well organized architecture with the final film well stratified (J. J. Richardson, Bjornmalm, and Caruso 2015).

This is explained by analyzing the different forces governing the deposition, from centrifugal and viscous forces and electrostatic attractions [LbL\_review2016]. In fact, the quick removal of water from the polyelectrolyte solutions allows a better organization of the chains and a smoother substrate. Furthermore, the high speed allows a control over the thickness and the final surface morphology.

Electromagnetic and fluidic LbL are two very attractive approaches regarding the applications, allowing new methods of assembly; unfortunately, the equipment is difficult to possess, and the expertise are needed.

The coating mechanism adopted by the former is based on the application of an electric or magnetic field in an electrolytic cell; the force produced would move the charged polymer that deposits on the oppositely charged electrode. This is known as electrodeposition (Xiao et al. 2016) (Figure 1.21 a). Like immersive LbL, the electrodes are subsequently washed and introduced in the other polyelectrolyte solution.

Also magnetic particles may be used as building blocks (Joseph J. Richardson et al. 2016).

The fluidic LbL assembly (Figure 1.21 b), like the electromagnetic technology, is an attractive method to coat different substrates with nano-sized layers and high-throughput, but the equipment is expensive and hard to fabricate.

Vacuum or pressure are the two main methods to move fluids in tubes or microfluidic devices, often manufactured “on chip”; capillary forces are also used to move the solutions, easy to implement given the absence of active devices like pumps, but it doesn’t allow a dynamic control over the deposition. It’s an interesting methodology that can coat surfaces placed inside fluidic channels or even deposit multilayers on the capillary walls (J. J. Richardson, Bjornmalm, and Caruso 2015; Xiao et al. 2016). Beside the applications just mentioned, microfluidic assembly has also been used in the fabrication of artificial-cells, coating droplets containing biomolecules with lipids which would constitute the membrane (Elani 2016).

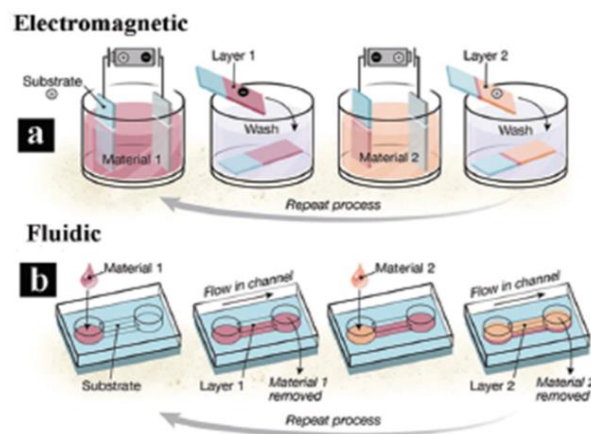


Figure 1.21 Representation of the electrodeposition and microfluidic LbL. (XIAO et al. 2016)

### LbL application in Nanomedicine

LbL has been widely studied in the biomedical field, but only recently this technique has been applied in nanomedicine, improving nano-materials stability and interaction with the living organism at the nanoscale.

This technology is also a great tool for giving active targeting abilities to nanoparticles, as well as allowing these to release a cargo like a specific drug in a controlled way (Poon et al. 2011). These nanoplatforms and implants need to be hidden from the immune system, which would recognize them as foreign bodies and consequently rejected.

Applications in the theranostic field are very attractive: Dreaden et al (Dreaden et al. 2014) deposited poly-L-lysine (PLL) and Hyaluronic Acid (HA) on polystyrene

nanoparticles, conferring to them targeting abilities; in fact, hyaluronan, and other GAGs, selectively bind to cell-surface receptor CD44 overexpressed by cancer cells. By controlling the number of layers deposited, it's possible to control the amount of drug loaded as well as the consequent release.

Investigations are focusing on creating controlled drug release systems, which allow a more specific therapeutic effect avoiding premature drug release which can damage healthy tissue and, obviously, will decrease the amount of agent reaching the tumour and the final efficacy (X. Q. Liu and Picart 2016a).

Some works used LbL assembly to incorporate in scaffold proteins, like grow factors such as Bone Morphogenetic Protein 2 (BMP-2) with the duty to direct progenitor cells to create bone (Macdonald et al. 2011). In fact, the LbL allows a higher amount of biomolecules to be entrapped, so to prolong the effect with a sustained release and improve the efficacy.

Vascular prosthesis is a class of devices that requires a careful surface engineering, in order to avoid thrombogenicity and infections, and it must resist to numerous mechanical stresses. The LbL imparts all these different requirements to the implant, by combining different materials and their properties (Rinckenbach et al. 2008).

Thanks to the versatility of the LbL technology, the substrates have different shapes, different material and may be coated with various polyelectrolytes and building blocks. Jia et al (Jia et al. 2007) functionalized multi walled carbon nanotubes (MWCNT) via electrostatic LbL, with antisense oligodeoxynucleotides, in order to down regulate the expression of some genes, and CdTe QDs for tracking the distribution of the platform real time. The system cell internalization was examined via confocal microscope: the device was found in the cytoplasm (without the nucleic acid) and in the nucleus (with the nucleic acid). This demonstrated the suitability of the LbL to delivery biomolecules for gene therapy, in order to inhibit protein expression.

LbL allows the creation of a shell sensitive to different stimuli: chemical, such as PH, solvents and electrochemistry and physical, such as temperature, light and others. Indeed, it's well known that the tumour environment has a slightly acidic pH (6.5) (Dreaden et al. 2014) compared to the rest of the body (7.4), so it's possible to exploit this variation by giving to drug delivery systems the ability to degrade when pH gets lower.

Poon et al (Poon et al. 2011) deposited PLL and poly(ethylene glycol) (PEG) on a negative charged nanoparticle, via electrostatic assembly, exploiting the neutravidin-  
iminobiotin bond. This linkage would decompose at acidic pH, allowing a charge-based cellular internalization between the positive PLL and the negative cell membrane. The deposition of nano-films over a sacrificial template is an interesting application of the electrostatic LbL: after the coating deposition the template is dissolved leaving a shell of alternatively charged polyelectrolytes (Figure 1.22).

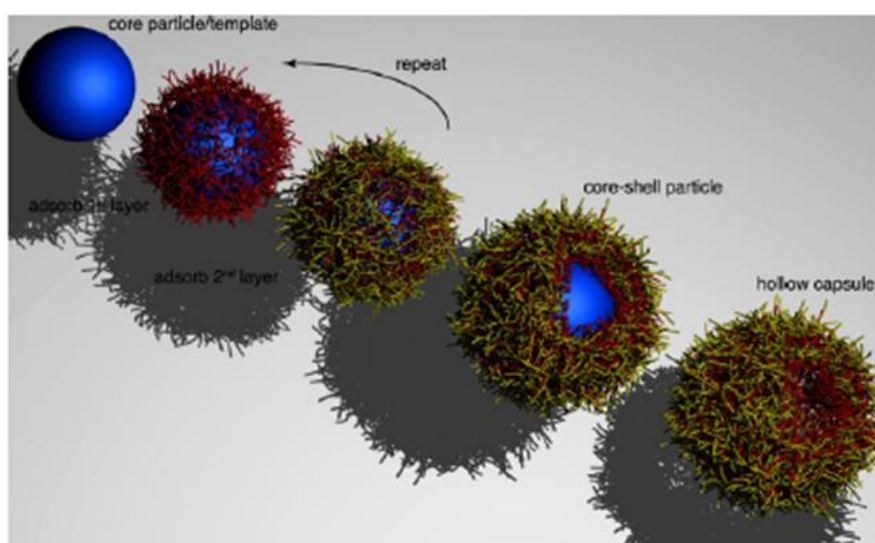


Figure 1.22 Coating process of a particle that in the last step is dissolved, leaving a hollow capsule (Johnston et al. 2006)

This strategy has been largely applied on particles, in order to obtain micro and nanocapsules, with controlled size, composition, porosity and stability (Johnston et al. 2006).

Cadmium carbonate, manganese carbonate (Antipov et al. 2003), calcium carbonate (Volodkin et al. 2004; Won et al. 2010) and other colloidal particles were used as the sacrificial template that, after being covered by a multilayer film, is selectively removed when suspended in a peculiar solution of EDTA or other acids.

This approach creates a sort of environment separated from the rest, so the cargo can be protected from any kind of degradation, giving more time the vehicle to reach the target, improving the solubility in water environment and potentially impart the ability to be tracked (Volodkin, Larionova, and Sukhorukov 2004; Kittitheeranun et al. 2015).

The microcapsules can be loaded with different compounds and agents. In fact, some studies have incorporated in the core QDs for bioimaging (Liao et al. 2016) or drugs like

Curcumin (Kittitheeranun et al. 2015) and, thanks to hydrophobic interactions, diffusion and a large surface area. Interesting is the use of biomolecules as polyelectrolytes, so to potentially use a multi-modal strategy by incorporating also a drug inside the capsule.

Different polyelectrolytes have been investigated: PAH/PSS bilayers are definitely the most used, Poly(diallyldimethylammonium chloride) PDMAC as polycation (Kittitheeranun et al. 2015) and also DNA strands (Liao et al. 2016) able to degrade at acidic pH and allowing the exit of the cargo.

### 1.3 Aim and Objectives of the work

The main aim of this project is to use the immersive LbL technology in order to coat  $\text{CaCO}_3$  microparticles in combination with GQDs, as imaging probes and drug release systems for the development of a suitable theranostic platform.

The work is overall based on exploiting the efficacy of the LbL technique, in order to create a core-shell structure in which the core is finally dissolved through EDTA, creating a hollow capsule (Figure 1.23).

Finally, we aimed to optimize the synthesis protocol of the  $\text{CaCO}_3$  particle in order to obtain stable nanometer-sized spheres, good for a potential passive targeting effect.

**OBJ1:** Assessing the chemical, physical and optical properties of GQDs. Elements and surface functional group were investigated by FTIR-ATR and XPS as well their fluorescence and absorbance. The morphology and size were analysed via TEM.

**OBJ2:** GQDs cytocompatibility assessment to make sure that the imaging probes did not cause any cytotoxic effect. Live/Dead cell viability assay and Presto Blue Viability assay were performed at different time points with different GQDs concentrations seeded with Y201 Immortalised Mesenchymal Stem Cells (MSCs) and Fibroblasts.

**OBJ3:** Optimisation of the  $\text{CaCO}_3$  microparticles synthesis process, in order to create stable sphere-shaped structures. The creation of nanoparticles has also been conducted, in order to prove the suitability of this strategy for a potential drug delivery system with passive targeting abilities.

**OBJ4:** LbL assembly as a coating strategy for micro & nanoparticles functionalisation, with the purpose to create a strong shell that would protect the inner cargo when the core is finally dissolved and to impart tracking abilities to the particles with the GQDs.

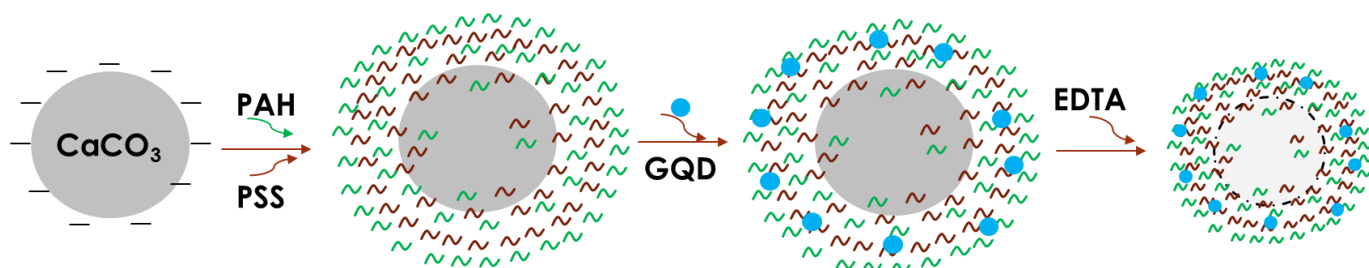


Figure 1.23 Schematic illustrations of the  $\text{CaCO}_3$  functionalisation with PAH and PSS, the incorporation within the layers of the GQDs and the final inner core dissolution

## Chapter 2: Manufacturing protocols and characterisation

---

### 2.1 Materials

All the reagents, if not differently stated, were purchased from Sigma Aldrich (UK).

Calcium Carbonate ( $\text{CaCO}_3$ ) has been synthesised from Sodium Carbonate ( $\text{NaCO}_3$ ),

Calcium Chloride ( $\text{CaCl}_2$ ). One of the synthesis process was conducted in Glycerol.

For the multilayer deposition, the polycation poly(allylamine hydrochloride) (PAH, *Mw* 120,000 Da), the polyanion poly(sodium 4-styrenesulfonate) (PSS *Mw* 70,000 Da),

Sodium Chloride ( $\text{NaCl}$ ), Chloridric Acid ( $\text{HCl}$ ), Sodium Hydroxide ( $\text{NaOH}$ ),

(Ethylenedinitrilo)tetraacetic acid (EDTA) have been used. Graphene Quantum Dots

(Pr. Number 900708) have been purchased as comparison with the in-house GQDs.

For cells culture, Dulbecco's Modified Eagle's Medium (DMEM) supplemented with 10%

fetal bovine serum (FBS), 5000 U/mL penicillin/streptomycin and 1% Glutamine (Lonza,

UK) and Dulbecco's phosphate-buffered saline (PBS).

### 2.2 Manufacturing Methods

#### 2.2.1 $\text{CaCO}_3$ microparticles synthesis

Following a previous protocol reported in literature (Volodkin et al. 2004), Calcium Carbonate microparticles have been fabricated using  $\text{CaCl}_2$  and  $\text{Na}_2\text{CO}_3$  as precursors at the same molarity, 0.33 M, and with same volume. The reagents were initially solubilized in deionised water ( $\text{dH}_2\text{O}$ ) separately and the solution of  $\text{Na}_2\text{CO}_3$  was rapidly poured into the  $\text{CaCl}_2$  solution under constant and intense mixing, over a magnetic hot plate at room temperature (RT).

This reaction was conducted for three different time points: 2, 5 and 10 minutes.

When the process was concluded, the product was left to rest for 60 seconds, poured into a falcon tube and centrifuged three times in  $\text{dH}_2\text{O}$  in order to separate the  $\text{CaCO}_3$  from the supernatant and to clean it from any unreacted residuals. Subsequently the final product was left to dry at RT or in incubator at  $37^\circ\text{C}$ .

In another synthesis procedure, PSS (1mg/mL) (Imai et al. 2012) was dissolved into the  $\text{Na}_2\text{CO}_3$  before the reaction. Different temperatures have been also investigated (RT and  $35^\circ\text{C}$ ).

In this optimised protocol the stirring was carried out for 100 seconds without resting phase, but immediately centrifuging and washing the product in  $\text{dH}_2\text{O}$ .

### 2.2.2 Nanoparticles synthesis

As a proof of concept, the fabrication of particles with a smaller size range, potentially nanoparticles, has been conducted. The same reaction explained in the par 2.2.1 has been carried out and the precursors solution were prepared at higher molarity (1M). In order to obtain particles with a nanometric size, we investigated as well the influence of glycerol as reported in literature (Trushina, Bukreeva, and Antipina 2016). The salt concentration adopted was 0.1M, with 83.3% v/v of the polyol and two different stirring times (2 and 50 minutes). One synthesis was carried out with the addition of PSS (dissolved in  $\text{Na}_2\text{CO}_3$ ) at 1 mg/mL concentration for 50 minutes. The first centrifugation was conducted for 5 minutes at 4000 rpm, while the 3 subsequent in  $\text{dH}_2\text{O}$  for 2.5 minutes at 900 rpm. The final product was dried in incubator at  $37^\circ\text{C}$ .

### 2.2.3 Polyelectrolyte deposition

Aqueous solutions of both polyelectrolytes (PSS and PAH) were prepared in 0.5M NaCl. The washing steps were carried out in 0.05 M NaCl water solution and the pH of all the solutions was titrated at 6.5 with the addition of NaOH and HCl (0.1M and 0.5M). The LbL-assembly procedure (shown in Figure 2.1) was conducted changing different parameters: polyelectrolytes concentrations (2 mg/mL and 5 mg/mL); time and method of deposition; amount of material (25mg, 50mg, 100mg); number of centrifugation steps and the respective durations and rpm. The  $\text{CaCO}_3$  microparticles were dissolved in the polyelectrolyte solutions (10 mL every 100 mg of  $\text{CaCO}_3$  powder), starting with the polycation (PAH) for 15 minutes of immersion; then a first centrifuge of 2 minutes at 1200 rpm was carried out to remove

the excess polyelectrolyte followed by two washing steps (2.5 minutes at 1200 rpm) in dH<sub>2</sub>O.

Before the last centrifugation step a small amount of functionalized powders was removed in order to measure the corresponding Zeta potential.

After the LbL procedure the obtained product was dried at 37°C and then kept in the fridge for further tests.

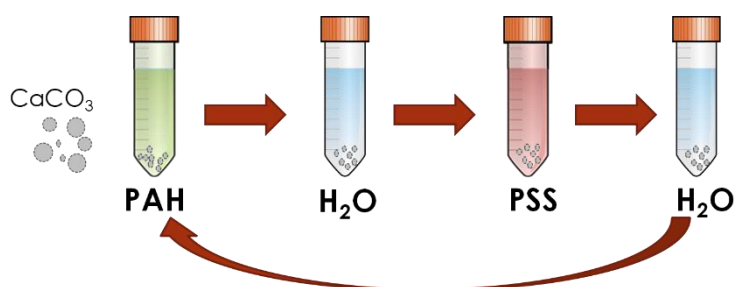


Figure 2.1 Schematic illustration of the LbL functionalization. A total of 7.5 cycles were conducted

#### 2.2.4 Graphene-based QDs synthesis

GQDs were synthesised as described in previous work (Roy et al. 2014). Briefly 250 mg of tea waste and 10 ml of ultrapure water were boiled in water at 80°C for 1 hour, followed by centrifugation at 12 000g for 10 min to remove any remaining solid residues. Subsequently the supernatant was filtered through a 0.22 mm membrane and then stirred and sonicated for 30 min at room temperature (25°C). This solution was then reacted in an autoclave at a temperature of 250°C for 8 h. The precipitate was carefully discarded after being cooled down to RT and then centrifuged at RCF 25 000g for 20 min, and the supernatant was collected and washed twice. Dialysis was then performed (cutoff 3.5 kDa) for a duration of 3 h and the product was dried overnight at 60°C in an oven, to obtain pure GQDs.

The product was then dissolved in water and freeze dried for further evaluations.

#### 2.2.5 Combining the CaCO<sub>3</sub> microparticles and the GQDs via LbL assembly

The GQDs were dissolved in PSS at a concentration of 0.33 mg/mL. The first 9 layers were deposited as previously described (par. 2.2.3). The 10<sup>th</sup>, 12<sup>th</sup> and 14<sup>th</sup> layers were deposited using the solution of GQDs, in order to incorporate the nanoparticles onto the calcium carbonate within the layers (Figure 2.2).

The parameters for the QDs deposition were the same and the obtained product was dried at 37°C and then kept in the fridge for further tests.

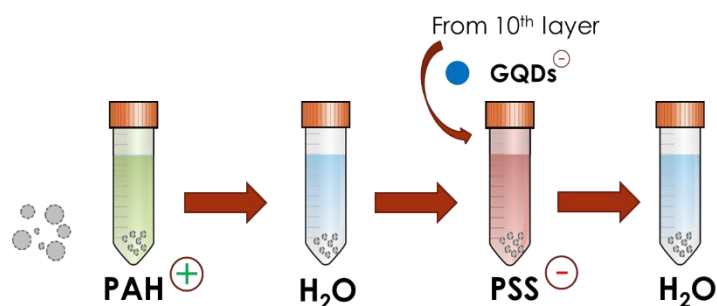


Figure 2.22 LbL process with the addition of GQDs from the 10<sup>th</sup> layer

## 2.2.6 Microcapsules fabrication

The obtained microparticles, after the LbL film was deposited, was suspended into an EDTA solution, at 0.1M, to selectively dissolve the inner core of the spheres. The solution pH was adjusted at 7, by adding NaOH (5M).

The suspension was vigorously magnetically stirred for 30 minutes, at RT, and then poured in various Eppendorf for centrifuging (3 total centrifuges in EDTA for 5 min at 5000 rpm) thus to discard the calcium carbonate and other residuals. Other 3 centrifuging steps were carried out in dH<sub>2</sub>O.

The final product was suspended in dH<sub>2</sub>O and stored at 4°C or dried in incubator for further tests.

## 2.3 Characterisation methods

### 2.3.1 GQDs characterisation

#### 2.3.1.1 Physico-chemical analysis

##### 2.3.1.1.1 *Fourier Transformed Infrared spectroscopy (FTIR-ATR)*

To assess the surface functional groups of the GQDs FTIR-ATR analysis was conducted. Measurements were obtained with a Spectrum Two PE instrument equipped with a horizontal attenuated total reflectance (ATR) crystal (ZnSe) (PerkinElmer Inc., USA).

Data are collected in Absorbance mode, with wavenumber values ranging from 4000 cm<sup>-1</sup> to 550 cm<sup>-1</sup>. Each spectrum was the result of the average of 16 scans with 4 cm<sup>-1</sup>

resolution. After each scan a baseline correction is performed.

All the samples examined were in the form of powder.

#### *2.3.1.1.2 X-ray photoelectron spectroscopy (XPS)*

X-ray Photoelectron Spectroscopy is an exceptionally sensitive tool to investigate the chemical elements constituting the outermost layer of a surface approximately up to 200Å. Thus, the samples were examined by a scanning microprobe Kratos Axis Ultra-DLD XPS spectrometer (EPSRC Harwell XPS Service Cardiff, UK), equipped with a monochromatised AlK $\alpha$  X-ray radiation source. The base pressure in analysis chamber was 10<sup>-9</sup> mbar. Samples were analysed in High Power mode with an X-ray take-off angle of 45° (scanned size ~1400 × 200 μm). For each specimen, survey scans (Fixed Analyser Transmission mode, binding energy (BE) range 0–1200 eV, pass energy 117.4 eV) and high-resolution spectra (FAT mode, pass energy 29.35 eV) were acquired of C<sub>1s</sub>. Atomic concentration (At.%) on the survey scan was performed using the built-in CasaXPS software package and in order to detect the Binding Energy (BE) representing the chemical binding states of the each elements within the films, the XPS spectra for the chemical elements detected from the films were subjected to peak deconvolution using the same software.

#### *2.3.1.1.3 Zeta Potential*

To measure the surface charge of GQDs a Zetasizer Nano ZS Instrument (Malvern Panalytical Ltd) was used. The samples were diluted in dH<sub>2</sub>O to reach a concentration of 25 μg/ml.

The final value is calculated as average of three measurements, each obtained after a maximum of 100 runs.

#### *2.3.1.1.4 Absorbance*

The absorbance pattern of GQDs was investigated through UV-Visible (UV-Vis). The colloidal aqueous solution was excited on a whole wavelength range. Where the light was absorbed the pattern would slightly change, showing a hump on the specific wavelength. A double-beam UV-Vis spectrophotometer (Cintra 10e, GBC) was used to this purpose.

#### *2.3.1.1.5 Fluorescence*

Fluorescence spectra of GQDs were recorded through Cary Eclipse PL spectrophotometer (Varian CA, USA). The water suspension of the nanoparticles was excited at a wavelength range from 300 nm to 400 nm. The emission was then analysed and plotted on a range from 300 nm to 600 nm.

### 2.3.1.2 Morphological analysis

#### *2.3.1.2.1 Transmission Electron Microscopy (TEM)*

Transmission Electron microscopy has been performed on a Philips CM 100 Compustage FEI, HV = 100.0 kV, and digital images were collected using an AMT CCD camera (Deben) with a range of magnification up to 130,000x, with the purpose to analyse the morphology and size of the GQDs.

A small drop of GQD solution was deposited on a copper grid (Agar Scientific) and waited for the water to evaporate; the pictures were taken after few minutes and again after few hours.

#### 2.3.1.3 Cytotoxicity Evaluation

In order to assess the biocompatibility of GQDs produced from tea leaves we followed the international standard ISO 10993 (Goode 2016) (A. Deng et al. 2017). A comparison with industrial GQDs was carried out following the same protocols.

Human TERT immortalised bone marrow stromal cell line were supplied by Prof P. Genever (York University) (Y201) at passage 84 and cultured as already described (James et al. 2015). Fibroblasts were adopted as well and cultured with the same protocol. Briefly, cells were grown at 37°C, 5% CO<sub>2</sub>, in Dulbecco's Modified Eagle

Medium (DMEM, Sigma) with low glucose content, supplemented with 10% fetal bovine serum, 2mM L-glutamine and a 1% penicillin-streptomycin mixture (100U/mL). Cells were seeded in a 96- well plate at a density of 5000 cells/well (figure 2.3 b) and in a 24-well plate (on 13 mm diameter coverslips) at a density of 120000 cells/well (Figure 2.3 a) and incubated for 24h in culture medium. Then, the culture medium was removed and replaced with GQDs solution at different concentrations (50,200,500,1000  $\mu\text{g}/\text{mL}$ ). Cytocompatibility has been evaluated after 24 h and 48 h through live/dead assay on 24-well plate seeded coverslip and after 48 h through PrestoBlue on 96-well plate seeded cells. The results were then compared with control wells, where cells were cultured with normal media.

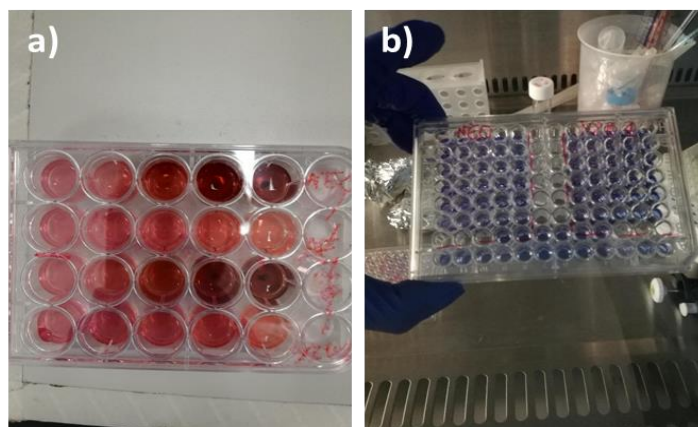


*Figure 2.3 Image displaying the well-plates used for the cytocompatibility tests. a) 24 well-plate for Live/Dead, cell cultured with various GQDs-based medium concentrations. b) 96 well-plate for Presto Blue, solution already poured and ready for scanning*

#### **2.3.1.3.1 Live/dead**

Live/Dead assay (LIVE/DEAD<sup>®</sup> Cell Imaging Kit, Life Technologies, Thermo Fisher Scientific, UK) was used according to the manufacturer's instructions. This fluorescence-based kit combines calcein AM and ethidium bromide to yield two-color discrimination of the population of live cells (green) from the dead cells (red) one. Each cell culture condition was washed twice with PBS before incubation with stainings. Briefly, 4  $\mu\text{M}$  ethidium homodimer-1 and 10  $\mu\text{M}$  calcein dilute in PBS, were incubated

in the dark with the cell-seeded and the cells encapsulated samples for 30 min at 37 °C (Montalbano et al. 2018). For the Live/Dead images, a fluorescence microscope (Nikon A1R inverted confocal microscope) was used.

#### *2.3.1.3.2 PrestoBlue*

The PrestoBlue assay was exploited to test the metabolic activity of cells seeded in the 96-well plate at 48h of culture. Culture medium was removed and samples were washed with pre-warmed PBS at 37 °C. PrestoBlue™ reagent (Thermo Scientific, USA) was warmed up and diluted in DMEM (1:10) protected from light; 250µL of solution was added to each well with the gel and incubated for 2.30 hours at 37°C, 5% CO<sub>2</sub>. Then, 100µL of each well solution (in duplicate) was transferred to a white bottom 96-well plate and a LS-50B Luminescence Spectrometer (Perkin Elmer, Waltham, MA) was used to measure the fluorescence (560 nm excitation and 590 nm emission).

The obtained values were corrected subtracting the average fluorescence of control wells with only PrestoBlue solution.

### 2.3.2 CaCO<sub>3</sub> Characterisation

#### 2.3.2.1 Physico-chemical analysis

CaCO<sub>3</sub> microparticles and microcapsules were characterised via FTIR-ATR, XPS and Zeta potential using the same protocols described previously (paragraph 2.3.1.1).

##### *2.3.2.1.1 Quartz Crystal Microbalance (QCM)*

QCM is a versatile and sensitive tool to investigate the deposition of thin films over a piezoelectric quartz sensor. These microgravimetric measurements were carried out via QCM with dissipation monitoring Q-Sense (QCM-D, Biolin Scientific) equipped with a piezoelectric Au/quartz crystal electrode, with 5MHz fundamental resonance frequency and static module. The shifts in frequency and dissipation were recorded continuously at 25°C, for all the 7 harmonics, in particular the 5<sup>th</sup> was considered for the following analysis. Briefly, 300 µL of PE solution were poured and left for 15 minutes, alternating every deposition with 4 minutes in LbL washing solution. We examined the LbL assembly with and without the incorporation of GQDs. The data

were then processed and the mass deposited was calculated applying the Sauerbrey model:

$$\Delta M = C \frac{\Delta f}{n}$$

C=17.8 ng/cm<sup>2</sup>/Hz is a constant of the equipment; n is the overtone (number of the harmonic considered). The multilayer thickness was measured using the Qsense Dfind software.

### 2.3.2.2 Morphological analysis

#### 2.3.2.2.1 *Scanning Electron Microscopy (SEM)*

SEM analysis were performed with a JEOL JSM-5600LV Scanning Electron Microscope model. The Calcium Carbonate sample in powder was deposited on the metallic support, sputtered with gold to make it conductive and subsequently analysed at a working distance of 6mm, an operation voltage of 10 EkV and at different magnifications. The pictures were analysed through the software ImageJ.

#### 2.3.2.3 Cellular uptake analysis

Y201 MSCs were cultured as previously described (par. 2.3.2.3). After the expansion, they were used between passage 86 and 90 and seeded at a concentration of 50000 cells are seeded into a 24 well-plate over 13mm glass coverslips and incubated for 24h in Medium and incubated at 37°C, 5% CO<sub>2</sub>.

Then, the Medium was taken out from the wells and replaced with a solution made of Media and GQDs at different concentrations and incubated for 24 h. We assessed the cytotoxicity of the QDs when the concentration is equal or above to 500 µg/mL, so we decided to check the bioimaging properties at 50 and 200 µg/mL.

After 24h of culture in the QDs-based solution, this solution was removed, the wells washed with PBS, and the cells fixed with 4% w/v paraformaldehyde (PFA).

When assessing the bioimaging abilities of the GQDs-functionalized CaCO<sub>3</sub> microparticles, the cells (1x10<sup>5</sup>) were seeded in 24 well plate and after 24 h of incubation, the particles before and after the core dissolution were added at

concentrations of 200 µg/mL and 500 µg/mL.

The cells are then stained in Phalloidin so to dye the cytoskeleton: cells were permeabilised using 0.1% v/v Tween20® (Sigma, Life Science) in PBS for three washes. Phalloidin was prepared using 1:100 dilutions of phalloidin-tetramethylrhodamine B isothiocyanate (Sigma) in 0.1% PBS/Tween20® for 20 min at room temperature, covered from light. Residue of phalloidin-rhodamine was removed by washing samples with 0.1% PBS/Tween20® solution three times. The samples were imaged using a Nikon A1R inverted confocal microscope at 20x magnification

### 2.3.3 Statistical analysis

Tests were performed at least in triplicate for each sample. The results were represented as mean ± standard deviation. Differences between groups were determined using One-way analysis of variance (ANOVA) with Tukey's multiple comparison test using levels of statistical significance of  $p < 0.05$  (\*),  $p < 0.01$  (\*\*),  $p < 0.001$  (\*\*\*), and  $p < 0.0001$  (\*\*\*\*).

## Chapter 3. Results

---

### 3.1 Graphene Quantum Dots

#### 3.1.1 Morphological characterisation

The morphological characterisation of GQDs at nanoscale was performed via TEM. The shape of the nanoparticles looked round and the diameter ranges from 4.5 nm to 100 nm (Figure 3.1 A-D). The pictures showed the variety of the structure size, without modifying the shape; moreover, when left for few hours on the grid before being seen at the microscope, the GQDs showed a tendency to agglomerate (Figure 3.1 E&F).

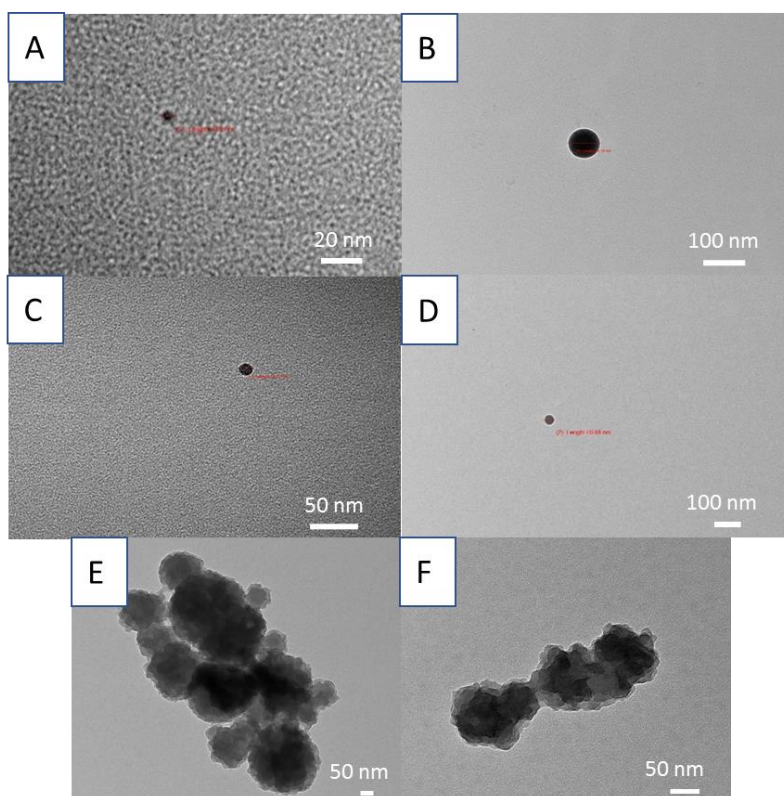


Figure 3.1 TEM pictures of GQDs, with a wide size distribution, ranging from 4.5 nm to 100 nm. Pictures E & F) show the tendency of the structures to agglomerate in water.

### 3.1.2 Physico-chemical characterization

The FTIR-ATR spectrum (Figure 3.2) identified the functional groups present on the GQDs surface; indeed, a broad band with peaks centered at  $3230\text{ cm}^{-1}$  and  $3355\text{ cm}^{-1}$  was characteristic of the stretching vibrations of O-H and N-H.

The narrow band with a peak at  $2988\text{ cm}^{-1}$  was assigned to the stretching vibrations of C-H. The peak at  $1619\text{ cm}^{-1}$  was considered to be characteristic of the vibration of C=C bond in the benzene ring (S. Zhao et al. 2015; Nair et al. 2017). The small peak at  $1394\text{ cm}^{-1}$  indicate the existence of the carboxyl group on the GQDs surface (Liang Wang et al. 2016).

The most intense peak, centered at  $1052\text{ cm}^{-1}$ , was attributed to the vibration absorption of the epoxy group C-O-C (Pan et al. 2010). Table 3.1 schematically recaps the functional groups and the respective wavenumbers.

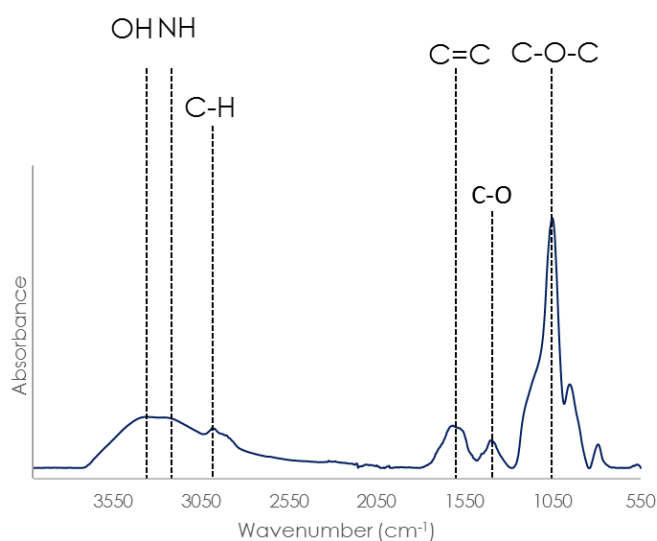


Figure 3.2 FTIR-ATR spectrum of GQDs and their highlighted surface functional groups.

Table 3.1 scheme of the chemical bonds and the respective wavenumber

Wn ( $\text{cm}^{-1}$ )	Functional group
1052	C-O-C (epoxy)
1394	C-O (carboxy)
1619	C=C (benzene ring)
2988	C-H
3230	NH
3355	OH

The XPS analysis was conducted to study the elements and the bonds constituting the GQDs surface. The analysis was conducted on the whole survey and high resolution of Carbon ( $\text{C}_{1s}$ ) with the deconvoluted spectrum displayed in Figure 3.3. As expected, there was a high content of Carbon (70.7%) and Oxygen (22.3%), which indicated the presence of hydroxyl and carboxyl groups. The detection of Nitrogen (4.8%) revealed the existence of amines on the GQDs surface, consistently with the FTIR results. A very low amount of Silicon was found (2.2%).

The high resolution XPS examined the bonds of C<sub>1s</sub>, revealing the already cited groups: 284.7 eV the C-C bond, 285.3 eV attributed to the C-N binding energy, 286.3 eV of C-O characteristic of epoxides and 288.6 eV of C=O carbonyl bond. The C-C bond was clearly the most intense, and its content was calculated to be the 56.1% of the C<sub>1s</sub> element. The other bonds were present at a similar percentage, as the C-O and C=O bonds were recorded to be, respectively, 13.6% and 14.1%. Interesting was the high presence of the C-N bond (16.2%), which was indicative of the abundance of amine groups in the GQDs.

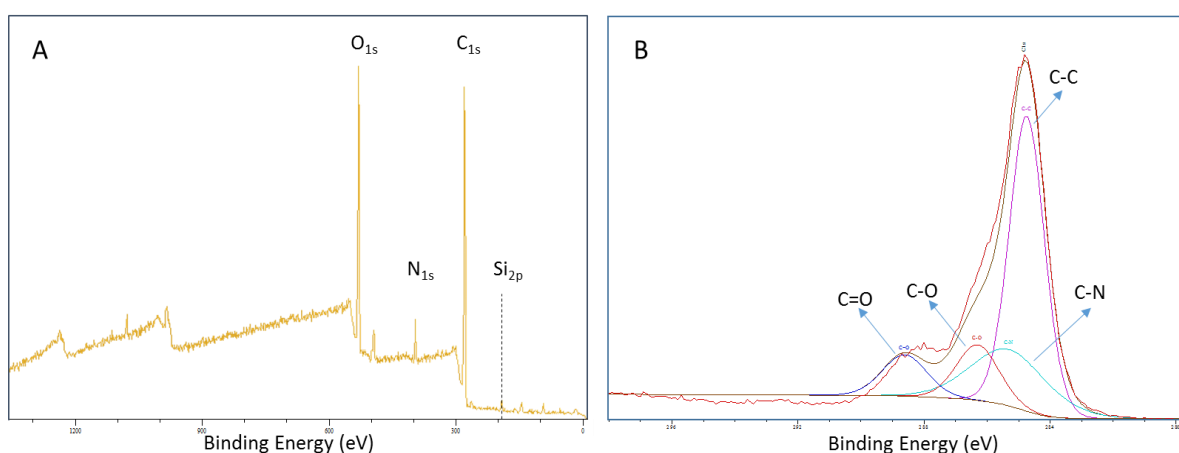


Figure 3.3 A) XPS survey spectrum of the GQDs; B) High resolution spectrum of the C<sub>1s</sub> element in GQDs

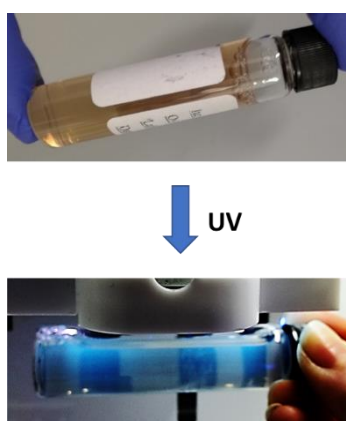
The GQDs Zeta potential was measured in order to understand the surface charge, with the purpose to exploit it for the subsequent LbL assembly. Table 3.2 reports the results obtained from different tests, conducted changing the pH of the GQDs-solution. GQDs possessed a highly negative surface charge, suitable to be used as polyanion and the change in pH did not influence the value.

Table 3.2 Zeta potential values of the GQDs at different pH.

pH	Zeta potential (mV)
5.1	-16.6 ± 1.4
7	-13.4 ± 0.8
10.1	-16.9 ± 1.2

### 3.1.3 Optical properties

The optical properties of the QDs were investigated through UV-Vis and Fluorescence (FL) tests. The former was conducted in order to understand the absorbance abilities of the GQDs, the latter, instead, to study their emission behaviour, in response to different excitation wavelength. An initial test was to excite the cuvette containing the GQDs with UV light: in these conditions the solution turned into bright blue, starting from a normal yellowish color demonstrating qualitatively that the GQDs possessed optical properties (Figure 3.4).



*Figure 3.4 color shift of GQD water-based solution under exposure to UV light*

As the pictures display (Figure 3.5), the FL properties were investigated by exciting the structures from 300 nm to 400 nm.

There were two strong peaks centered at 380/400 nm, consequence of the 320 nm and 330 nm excitations. When the wavelengths increased, the emission intensity got lower and shifted towards the red of the spectrum, showing excitation-dependent emission. The GQDs absorbance trend decreased for most of the wavelengths, but there were two pronounced edges around 280 and 320 nm, in the UV range, which indicated a stronger ability of the nanoparticles to absorb energy at those wavelengths. These results were consistent with the information deduced from the FL spectra.

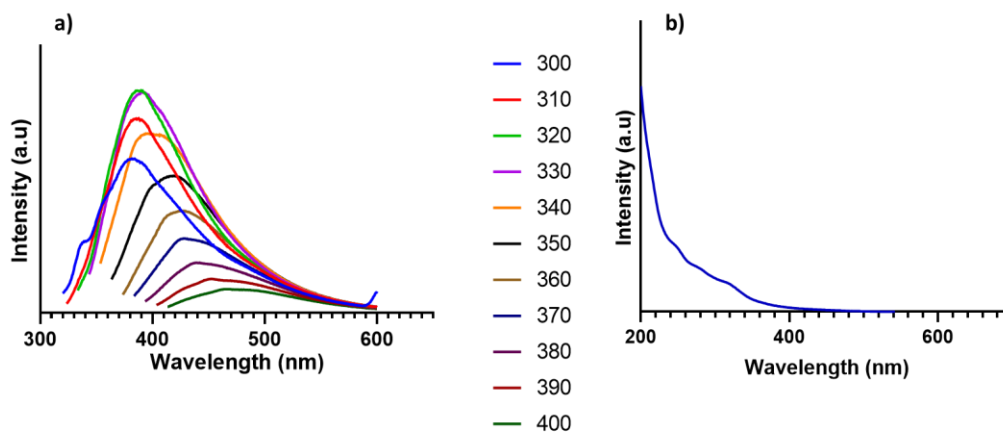


Figure 3.5 a) Fluorescence and b) absorbance patterns of the GQDs. The former shows a typical excitation dependent behavior; the latter displays two shoulders centered at 280nm and 320 nm.

### 3.1.4 Cytocompatibility assessment

Cytocompatibility studies were conducted to assess if the presence of GQDs in cell culture would induce their apoptosis.

Figure 3.6 shows the results of the Live/Dead viability assay at two time points (Day 1 and Day 2): green stained cells indicated the live cells while the red stained the dead cells. The analysis was based only from a qualitative assessment. Regardless of the cell line, of the quality of the GQDs and the time point, cells were alive and confluent, with an elongated structure, for concentration below or equal to 200  $\mu\text{g}/\text{mL}$ . Red stained cells were very few compared to the total amount. At 500  $\mu\text{g}/\text{mL}$  of GQDs concentration it was possible to notice the difference between the manufacturers: in fact, the GQDs produced from tea waste did not induce death, while the commercial of QDs showed cytotoxic effects.

The Y201 MSCs cultured with 500  $\mu\text{g}/\text{mL}$  of industrial GQDs showed a different behaviour after 24h of incubation, as they were live and confluent.

At 1000  $\mu\text{g}/\text{mL}$  the cells were clearly dead, even after 24h of incubation: the shape of the cells was indeed round and at a very low density.

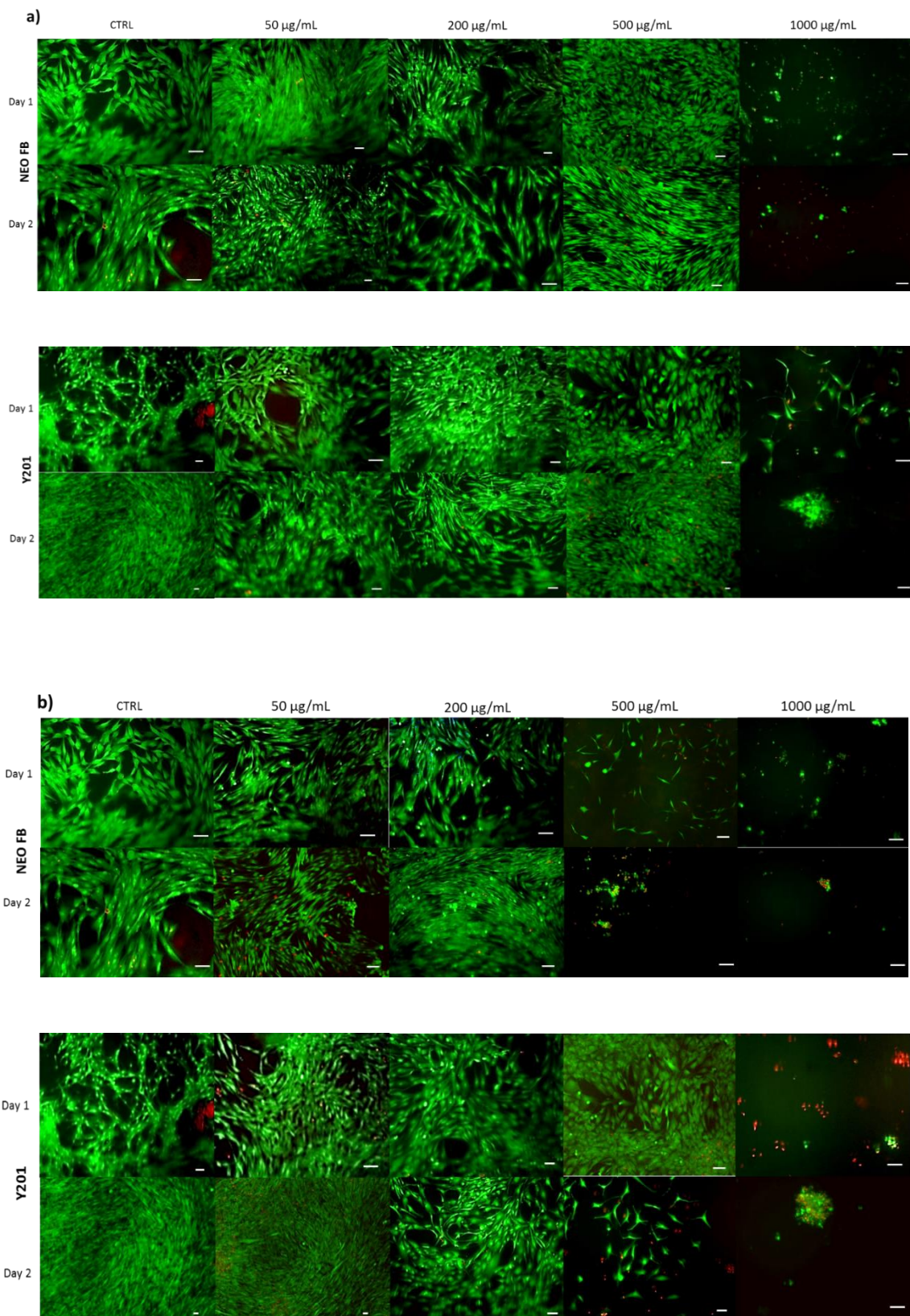


Figure 3.6 Live/Dead fluorescent microscope pictures. a) Neo-Fibroblasts and Y201 MSCs incubated with 5 different concentrations of green-route GQDs, ad examined after 24h and 48h. b) Neo-Fibroblasts and Y201 MSCs incubated with 5 different concentrations of industrial GQDs, ad examined after 24h and 48h. Cells stained green are viable; red ones are dead. Scale bar: 50  $\mu\text{m}$ .

The cells metabolic activity was evaluated via Presto Blue assay at 48 h; the cells were cultured in the same conditions and with the same GQDs concentrations that were used in the previously described test.

The graphs confirmed what already was found in the previous analysis. In fact, at the highest concentration (1000 µg/mL) the cells, regardless of the line, were not active, and there was a clear decreasing trend when the concentration reached 500 µg/mL for both the GQDs kinds, although the cells cultured with the green QDs looked more metabolic active than those cultured with the industrial nanoparticles. This behaviour was consistent with the Live/Dead findings. Significant differences were registered between both cell lines incubated with the green GQDs (Figure 3.7) at the highest concentration and the rest ( $p < 0.001$ ). The metabolic activity of the cells (both Y201 and Fibroblasts) results completely different at 500 µg/mL and 1000 µg/mL compared with every other concentration ( $p < 0.0001$ ) (Figure 3.7).

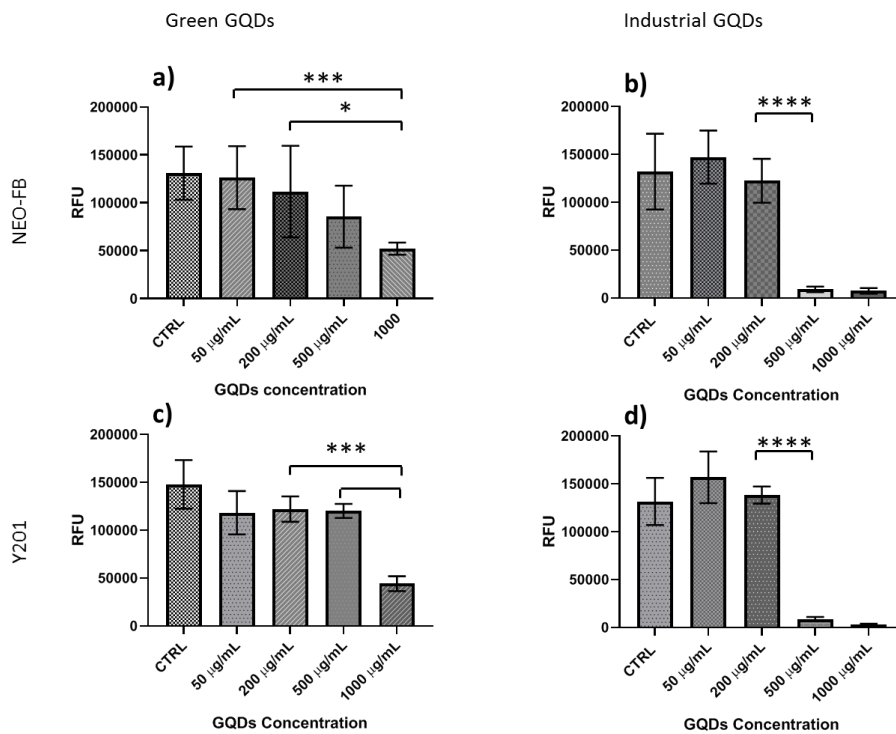
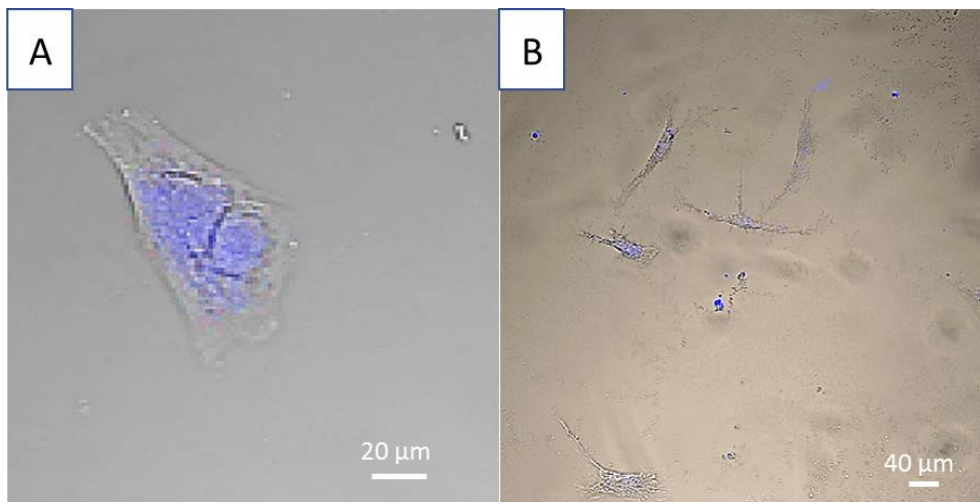


Figure 3.7 Metabolic activity of Fibroblasts incubated 48h with (a) green GQDs and (b) industrial GQDs. Metabolic activity of Y201 MSCs incubated 48h with (c) green GQDs and (d) industrial GQDs. Statistical analysis is represented:  $p < 0.0001$  \*\*\*\*;  $p < 0.001$  \*\*\*,  $p < 0.05$  \*

As Figure 3.8 displays, the nanoparticles regardless of the cell line and of the seeded amount, managed to be internalized and, when excited with UV, were able to emit blue light (408 nm). Moreover, it was possible to assess that their negative charge did not affect the internalization.

It also seemed that the intensity of the emission depended on the quantity of GQDs entering the cytoplasm, as some cells in figure 3.8 B looked brighter than others.



*Figure 3.8 Confocal microscope images taken after 24 h of incubation of cells and GQDs. A) Fibroblast cultured with 0.2 mg/mL GQDs concentration B) Y201 seeded with 0.05 mg/mL GQDs concentration*

## 3.2 CaCO<sub>3</sub> synthesis and functionalisation

### 3.2.1 Morphological characterisation

SEM analysis was conducted to analyse the morphology of the produced particles, at each step of the synthesis including the LbL polyelectrolytes deposition and the microcapsules obtainment after the core dissolution.

The final product of the CaCO<sub>3</sub> microcapsule synthesis showed an increasing quantity of cubic-shaped crystals as the mixing time increases from 2 to 10 minutes in both stirring conditions.

Furthermore, it was also noticeable that after drying at room temperature the presence of crystals resulting from the transformation of the microcores, as some of the particles were not completely turned into the new morphology, but showed a combination of both (Figure 3.9 A-C).

However, when the powders were dried at 37°C, the presence of round-shaped particles was higher in all the batches at different mixing times (Figure 3.9 D-F).

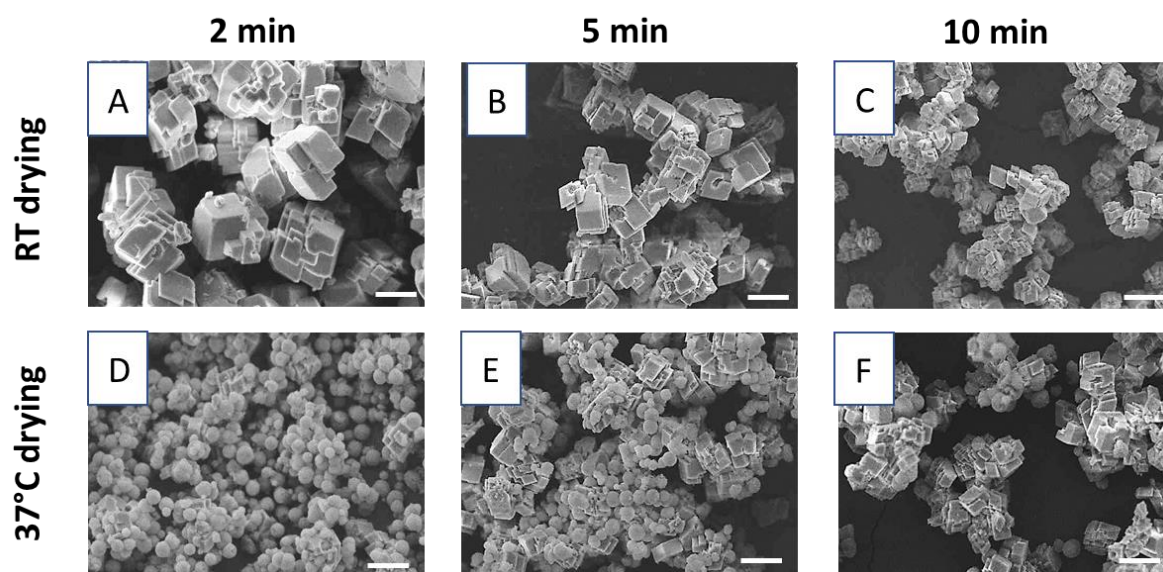
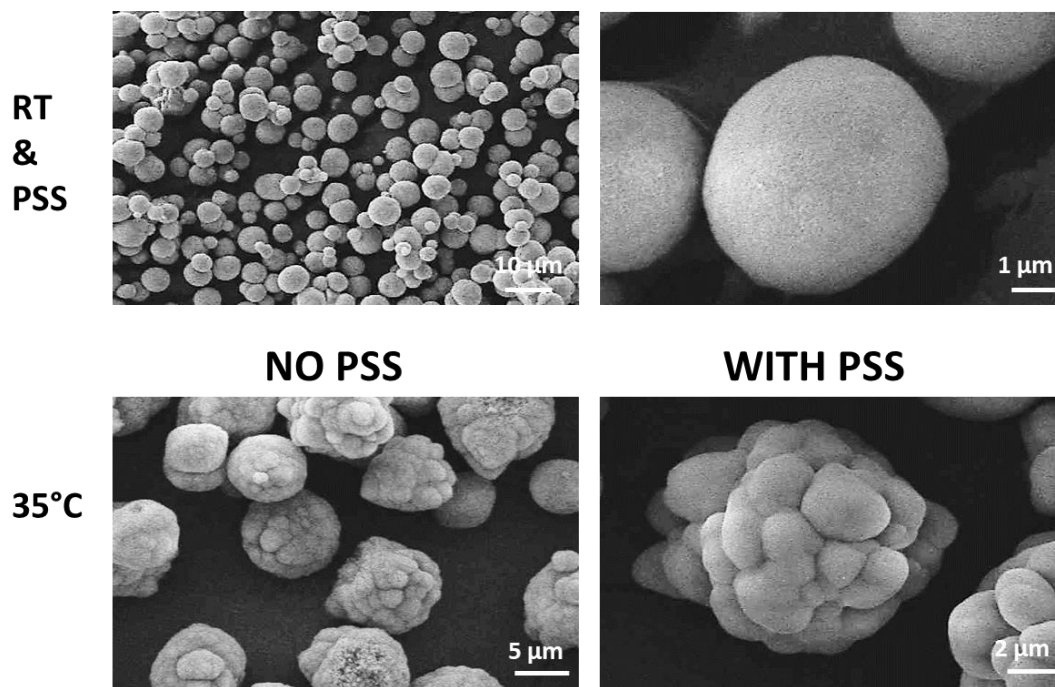


Figure 3.9 SEM pictures of the CaCO<sub>3</sub> microparticles synthesised after 2,5,10 min of precursor mixing and after drying at RT and 37°C. Scale bar Figure A = 5 μm; Scale Bar B-F = 10 μm

The PSS addition led to the obtainment of microspheres only, without the presence of rhombohedral crystals; moreover a higher reaction temperature (35°C) allowed a morphological change of the microparticles, in a cauliflower-like shape as showed in

figure 3.10.

The average size of the particles was  $3.49 \pm 1.09 \mu\text{m}$  with a highly porous surface.



*Figure 3.10 SEM pictures of  $\text{CaCO}_3$  particles with PSS at RT and with and without PSS at 35°C. The temperature changes the morphology of the particles, while the only addition of PSS generates a product with only spheres*

The subsequent analysis aimed to understand if the immersion in an aqueous solution would affect the morphological aspect of the prepared microparticles. The synthesis conducted with the addition of PSS and the increase of reagent solutions' temperature allowed the maintenance of the microparticles shape (Figure 3.11 B-D). Figure 3.11 A displays the product obtained after 30 minutes of immersion in water without the initial addition of PSS in the precursors solution: in this scenario the sphere-shaped microparticles transformed into smooth and clustered cubes.

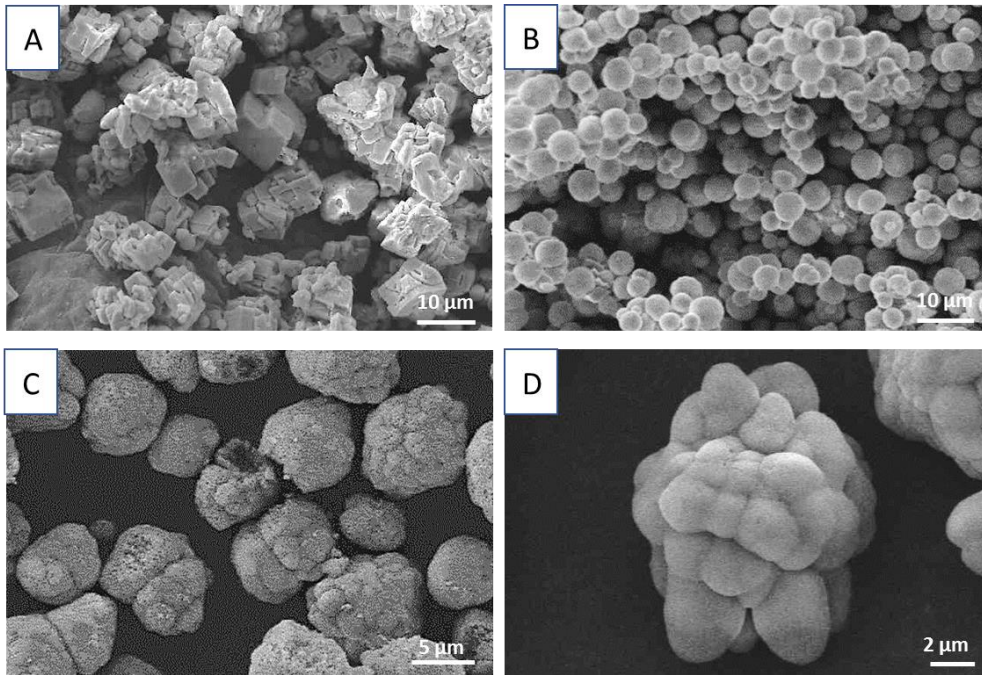


Figure 3.11 SEM pictures showing the microparticles morphology after immersion in water without A) and with PSS addition in the precursors solution B). C & D) synthesis temperature set at 35°C without and with PSS respectively.

All the subsequent synthesis were performed with PSS and at RT and for 100 seconds.

### 3.2.1.1 LbL-Functionalisation of CaCO<sub>3</sub> Microparticles

The next step was the functionalisation of the manufactured particles alternating the deposition of two polyelectrolytes, PAH (positive) and PSS (negative) through LbL assembly. After three layers, the particles' surface looked very rough and porous and the particles' shape remained circular (Figure 3.12 A & B). When the process was concluded and 15 layers were deposited (Figure 3.12 C & D), more homogeneous and smoother surface were found compared to a lower number of layers.

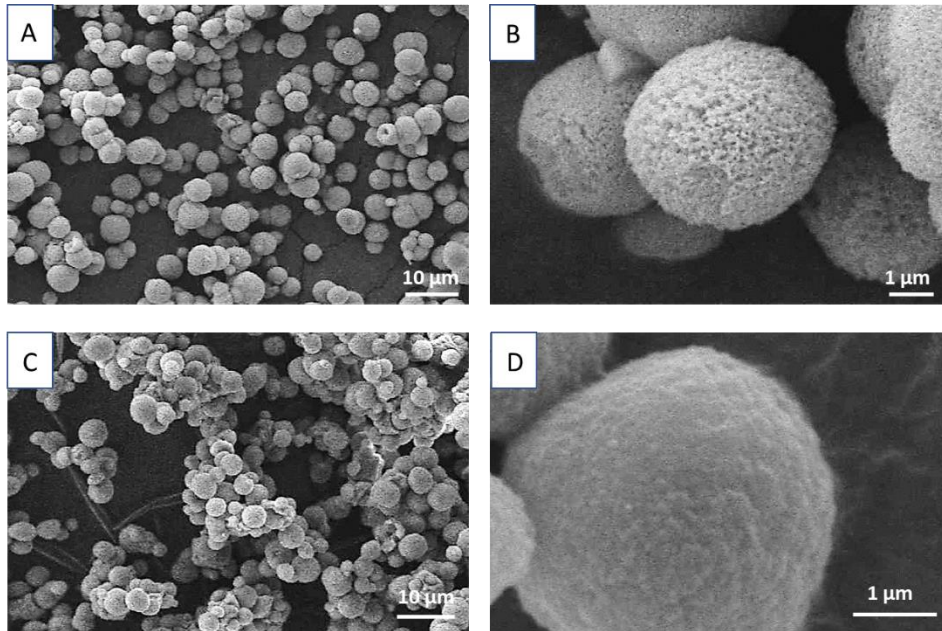


Figure 3.12 SEM pictures A and B show the coated particles after 3 layers deposited. C and D show the particles after 15 layers deposited.

Through the software ImageJ was possible to calculate the average diameter of the  $\text{CaCO}_3$  microparticles and to compare the bare ones with those obtained after being coated: the particles increased from an average diameter of  $3.49 \pm 1.09 \mu\text{m}$  to an average diameter of  $3.77 \pm 0.81 \mu\text{m}$ , after 15 adsorbed layers (Figure 3.13 a).

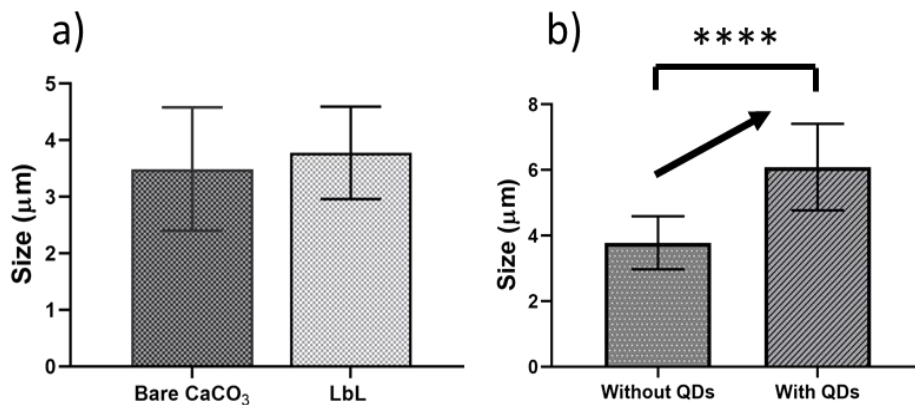


Figure 3.13 Average particles' diameters are represented. a) comparison between the microparticles with and without outer shell. b) comparison between coated particles with and without QDs

The image displays the internal structure of a microparticle, which presented a channel-like architecture moving towards the center of the sphere (Figure 3.14 A).

The nanocoating, after the deposition of 15 layers, resulted in a disorganized film, with

an average thickness of  $0.45 \pm 0.11 \mu\text{m}$  (Figure 3.14 B). The red arrow indicates the external PEs-multilayer film of a broken particle.

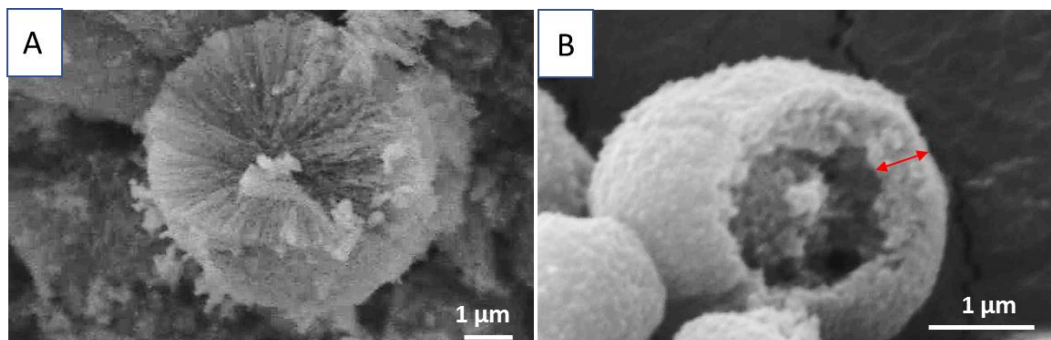


Figure 3.14 A) the internal structure of a microparticle; B) microparticle after the LbL assembly, with the external PEs shell highlighted

The incorporation of the GQDs (Figure 3.15) did not compromise the homogeneity and the smoothness of the nanocoating compared with the microparticles functionalised without their addition. It was noticed statistical significant increase in the size up to  $6.1 \pm 1.32 \mu\text{m}$  compared to those ones functionalized without GQDs within the layers ( $p < 0.0001$ ) (Figure 3.13 b).

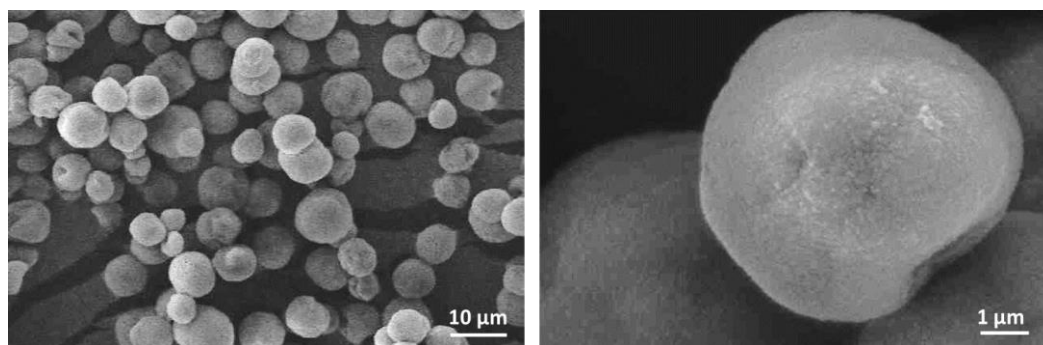


Figure 3.15 SEM picture of the  $\text{CaCO}_3$  particles after the LbL process incorporating GQDs onto the surface

The final effect on the particles was the removal of the  $\text{CaCO}_3$  which constituted the core, leaving the polyelectrolyte film outside, thus manufacturing a hollow microcapsule. The surface morphology of the newly fabricated microdevices presented holes and folds, confirming the absence of the inner particle and the efficacy of the EDTA immersion. This effect was visible for both the films deposited (Figure 3.16 A, B). The multilayer composed by PEs and GQDs, looked thicker and smoother.

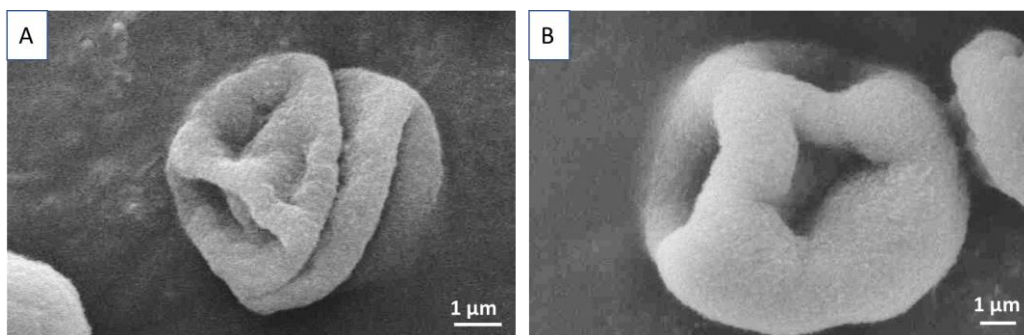


Figure 3.16 Particles morphology after EDTA core dissolution procedure. A) Microcapsule without GQDs B) with GQDs.

### 3.2.1.2 CaCO<sub>3</sub> Nanoparticles synthesis

Due to the increase in the molarity of the precursor solutions (1M), the particles showed a trend of size reduction with a homogeneous spherical shape (Figure 3.17 A). It was possible to notice at higher magnification the porous structure of the colloids and their small diameter (Figure 3.17B). This procedure enabled the reduction of the initial size, achieving an average diameter of  $1.7 \pm 0.4 \mu\text{m}$ .

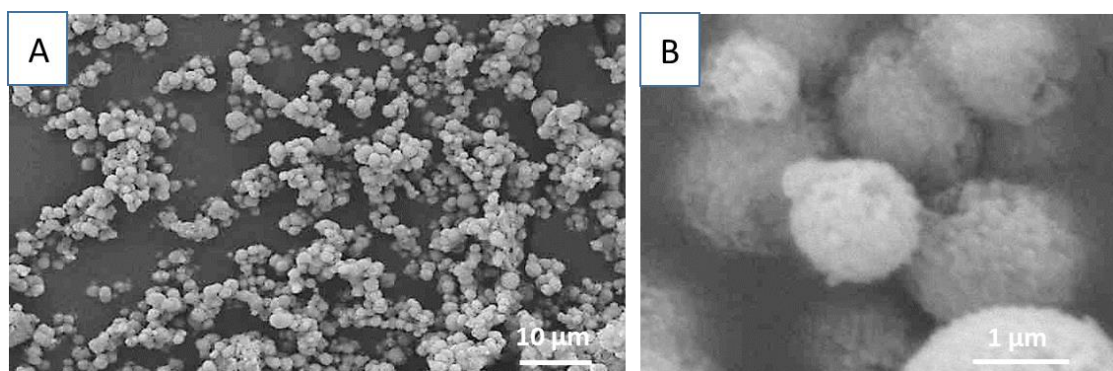


Figure 3.17 SEM pictures displaying microparticles, with circular shape and an average size of  $1.7 \mu\text{m}$ .

The use of glycerol (83.3% v/v) was investigated with two process durations (2 and 50 minutes), with and without PSS. When the synthesis was carried out without it, cubic-shaped crystals appeared in the sample and no spherical particles were found (Figure 3.18 a).

The addition of PSS resulted in the formation and stabilization of the spherical particles with an average diameter of  $720 \pm 18$  nm. The smallest particles found had a diameter reaching 320 nm (Figure 3.18 b). The red arrows in Figure 3.18 b show the nano-sized diameters achieved with the use of glycerol.

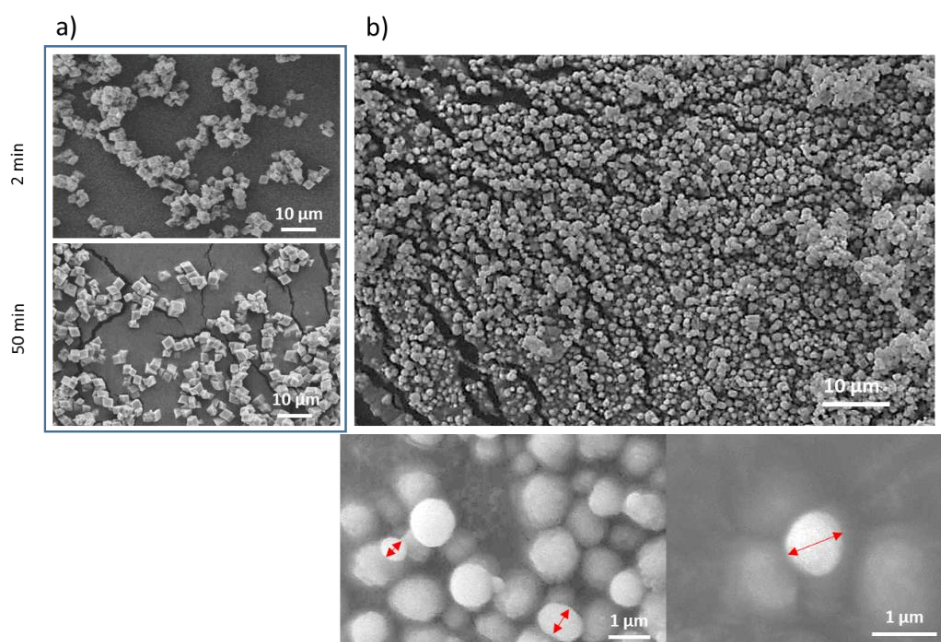


Figure 3.18 SEM picture showing the product of the tests aiming to reduce the particles' size. a) 2 and 50 min. reaction conducted in 83% of glycerol without PSS. b) 50 min. reaction in 83% of glycerol with the addition of PSS. Red arrows are indicative of particles with diameters of 320 nm up to 810nm

Figure 3.19 shows the size-decreasing pattern obtained from raising the reagents concentration to 1 M (from the initial 0.33M) and then the use of glycerol-based solutions, in order to achieve the nanoscale. Comparison was conducted via statistical analysis: the results are statistically different ( $p < 0.0001$ ), confirming that the size reduction was effectively accomplished.

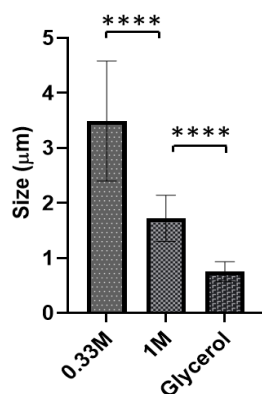


Figure 3.19 Graph representing the average diameters of the microparticles obtained with three different reactions. There is a decreasing trend, confirmed by the statistical analysis.

## 3.2.2 Physico-chemical characterisation

### 3.2.2.1 Quartz crystal microbalance

Figure 3.20 displays the frequency and energy dissipation shifts consequently the deposition of the two PEs with and without the GQDs adsorption. For what concerned the frequency, no significant difference was evident, with a total shift of almost 3000Hz obtained after the deposition of 15 layers. At each injection, almost immediately a sudden change in resonance frequency was recorded. The washing step had the effect of shifting the frequency in the opposite direction. The energy dissipation instead showed some differences from the 10<sup>th</sup> layer for the two tests: in fact, the slope increased in response to the addition of the GQD into the PSS solution; interestingly the first layer constituted by PSS and GQDs did not show any energy dissipation. From then on it grew quicker than when only PEs were injected.

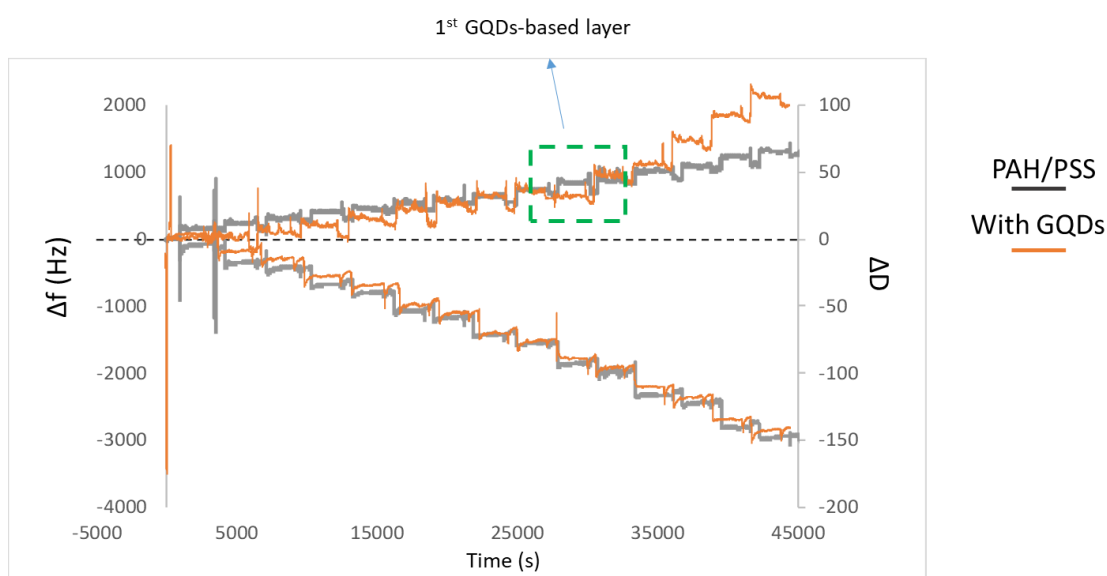


Figure 3.20 Frequency (below) and energy dissipation (above) shifts resulted from the deposition of PEs (Grey) and PEs with GQDs (Orange).

By applying the Sauerbrey model it was possible to calculate the total mass deposited and the multilayer thickness and no difference could be noticed. The mass calculated reached almost 10  $\mu\text{g}$  for either the tests (Figure 3.21); the thicknesses went over 100 nm for both the deposition, with an average thickness of 7nm per layer (Figure 3.22).

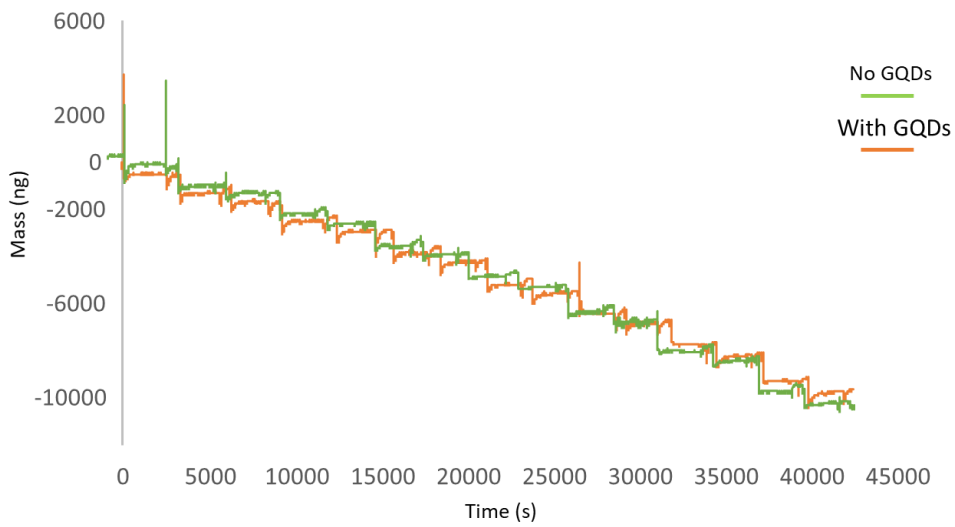


Figure 3.21 Mass change in response to the adsorption of the layers.

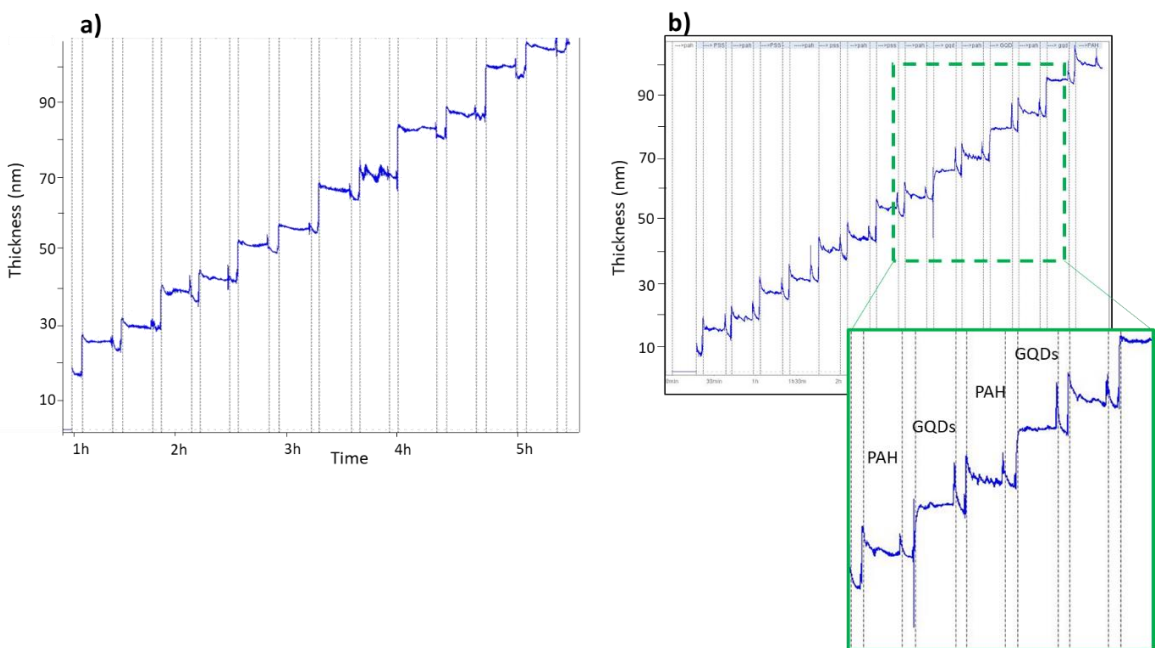


Figure 3.22 multilayer thickness obtained after 15 layers of a) only PEs) and b) PEs with GQDs.

### 3.2.2.2 FTIR-ATR and XPS analysis

Figure 3.23 shows the three spectra obtained from the synthesis conducted in the same conditions (reagents in aqueous solution at the same molarity and the same volume) but different duration.

Calcium Carbonate was characterized by 2 main peaks, at  $1404\text{ cm}^{-1}$  and at  $875\text{ cm}^{-1}$  attributed to the  $\nu_3$ -asymmetric stretching vibrations and the Ca-O stretching vibrations of the  $\text{CO}_3^{2-}$ . More precisely band at  $1404\text{ cm}^{-1}$  was related to the presence of Amorphous Calcium Carbonate (ACC) (X. Wang et al. 2009).

The peaks at  $744\text{ cm}^{-1}$  and at  $711\text{ cm}^{-1}$  were characteristic of the vibrations of the  $\text{CO}_3^{2-}$  of vaterite and calcite respectively. The latter was clearly more intense than the former, with the highest value resulting after 10 minutes process duration.

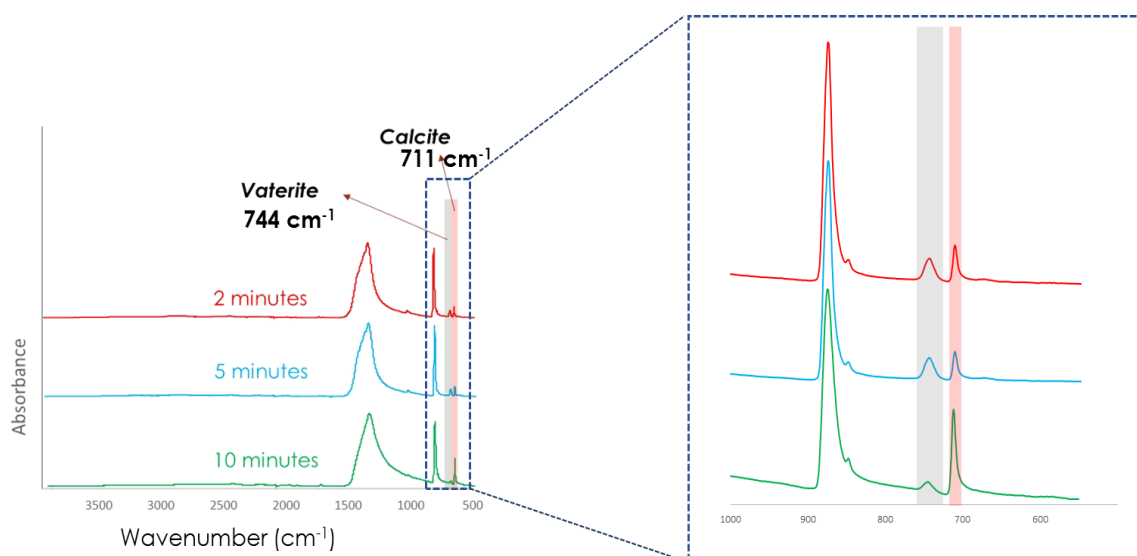


Figure 3.23 FTIR spectra of the  $\text{CaCO}_3$  obtained after the same reaction conducted for different durations (2,5,10 min). The peaks highlighted indicate the presence of vaterite and calcite. The enlargement shows the intensity of the cited peaks.

Similarly the spectra of the particles manufactured by changing the synthesis protocol showed common peaks but with some important differences (Figure 3.24). The addition of PSS was confirmed by the peaks at  $2987\text{ cm}^{-1}$  and  $2902\text{ cm}^{-1}$ ; moreover, a band centered at  $1100\text{ cm}^{-1}$  appeared, highlighting the presence of the polyanion, especially when combined with higher temperature (purple and green spectra). As expected, these bands were not present in the samples without PSS (black spectrum).

Peaks at  $1404\text{ cm}^{-1}$  and at  $875\text{ cm}^{-1}$  were presented well intense, highlighting the ACC and the general  $\text{CaCO}_3$  presence.

The peak at  $744\text{ cm}^{-1}$  was higher than  $711\text{ cm}^{-1}$  peak, due to the fact that the presence of vaterite form was higher than the calcite one. This trend was visible in the zoomed image, for all three samples.

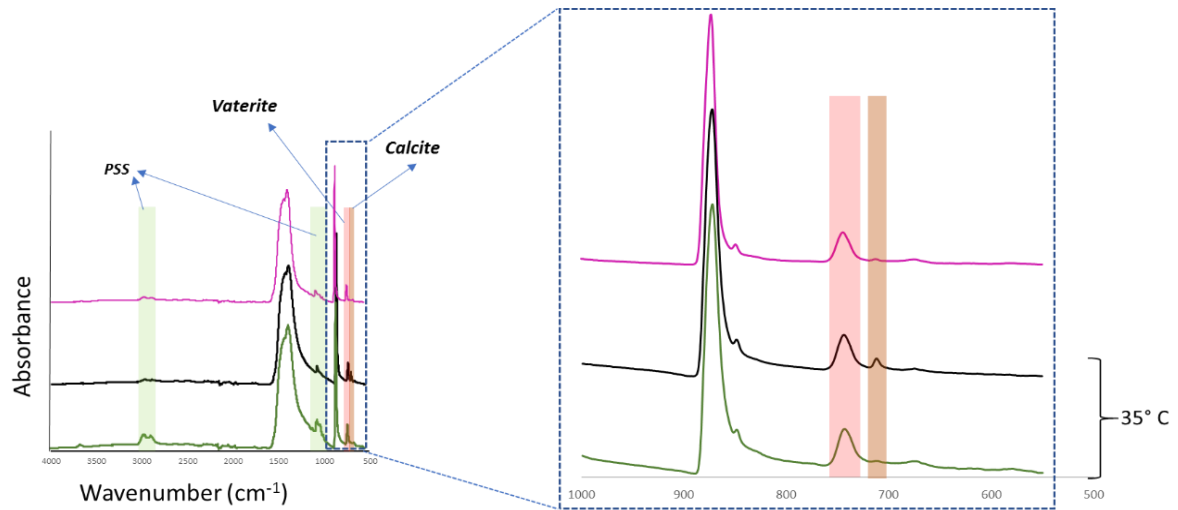


Figure 3.24 Spectra of the synthesis conducted with the addition of PSS or changing the reaction temperature. The peaks highlighted are characteristic of vaterite and calcite phases.

Figure 3.25 shows the spectra of the  $\text{CaCO}_3$  when left for 4h in water (a) and when 3 layers were deposited (b). The calcite peak seemed to increase in intensity (compared to Figure 3.24), although the vaterite peak at  $744\text{ cm}^{-1}$  was still present. The main  $\text{CaCO}_3$  peaks previously mentioned, at  $1404\text{ cm}^{-1}$  and  $874\text{ cm}^{-1}$  were not influenced by the immersion in aqueous environment.

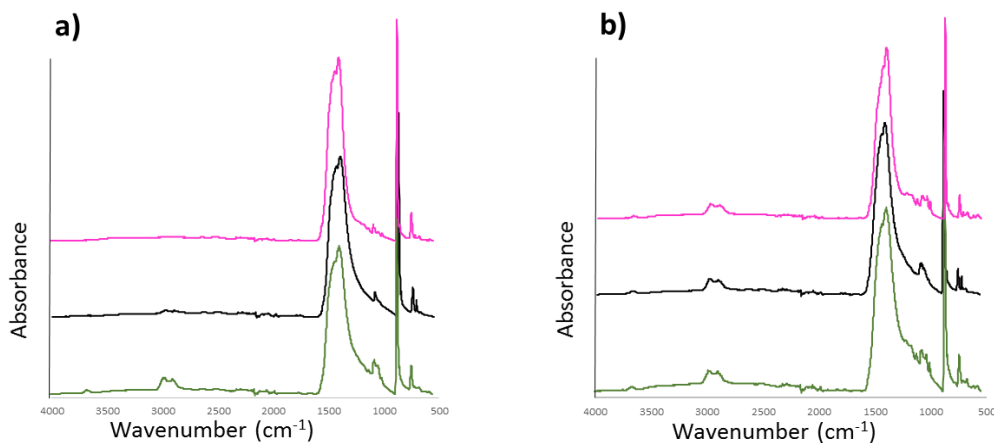


Figure 3.25 FTIR spectra of a) particles after being dissolved 4h in water; b) particles after 3 layers deposited.

Table 3.3 shows the ratio between the intensities of vaterite ( $I_v$ ) and calcite ( $I_c$ ), obtained from the tests previously described. Higher values were indicative of higher content of vaterite with respect to the calcite. Regardless of the reaction protocol, the ratios decreased when the particles were immersed in water environment and during LbL coating assembly.

*Table 3.3 Ratio between the intensities of vaterite and calcite peaks, obtained after the synthesis, after being immersed 4 h in water and after the adsorption of 3 layers.*

Synthesis CaCO <sub>3</sub>		$I_v/I_c$
Bare microparticles	PSS, RT	4.477
	PSS, 35°C	3.003
	Without PSS, 35°C	2.232
After 4h in water	PSS, Room T	3.68
	PSS, 35°C	2.84
	Without PSS, 35°C	1.60
After 3 layers	PSS, RT	2.8
	PSS, 35°C	2.485
	Without PSS, 35°C	1.3769

The spectra of the particles coated by of 15 layers showed peaks of both polyelectrolytes as well those typical of the CaCO<sub>3</sub>. The peaks of ACC and CO<sub>3</sub><sup>2-</sup> group were both present and highlighted. In particular the peak at 1404 cm<sup>-1</sup> shifted of few wavenumbers settling at 1407 cm<sup>-1</sup>, broadened and presented small shoulders, due to PAH adsorption on the microparticles surface, in particular the peak at 1501 cm<sup>-1</sup>, assigned to the N-H bending vibration of the polycation (Paltrinieri et al. 2017). The adsorption of PSS was clearly visible with various peaks belonging to a wide band between 1000 cm<sup>-1</sup> and 1200 cm<sup>-1</sup>. Particularly the peak at 1035 cm<sup>-1</sup> and 1183 cm<sup>-1</sup> were the symmetric stretching vibration of the SO<sub>3</sub><sup>-</sup> group; while the peak at 1602 cm<sup>-1</sup> was related to the asymmetric stretching vibration of the SO<sub>3</sub><sup>-</sup> group (Kittitheeranun et al. 2015).

The vaterite resulted still more intense with respect to the calcite, although the latter had an increase in intensity (Figure 3.26).

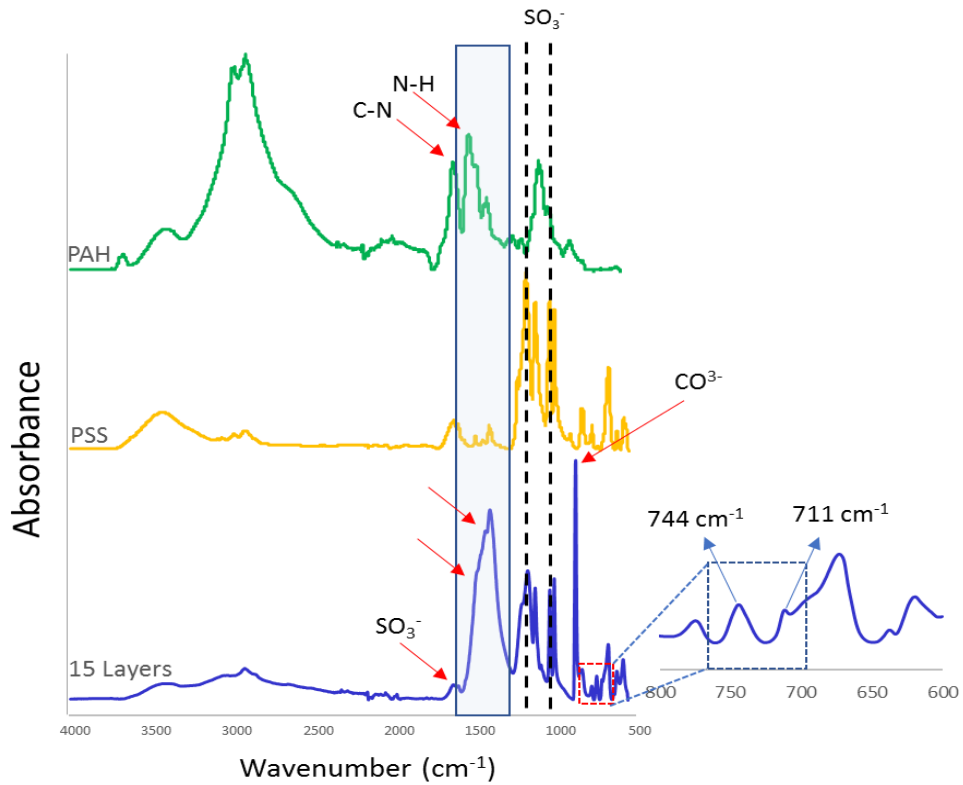


Figure 3.26 FTIR spectra of PAH (green), PSS (yellow) and functionalized particles after the adsorption of 15 layers. The zoomed picture highlights the vaterite and calcite peaks.

A final comparison between the surface chemical groups was performed between the spectra obtained after the nanocoating deposition and after the fabrication of the microcapsule (Figure 3.27).

The two main peaks of CaCO<sub>3</sub> completely disappeared, confirming the dissolution of the inner particle. The peaks described before, typical of the polyelectrolytes did not show any transformation or shift.

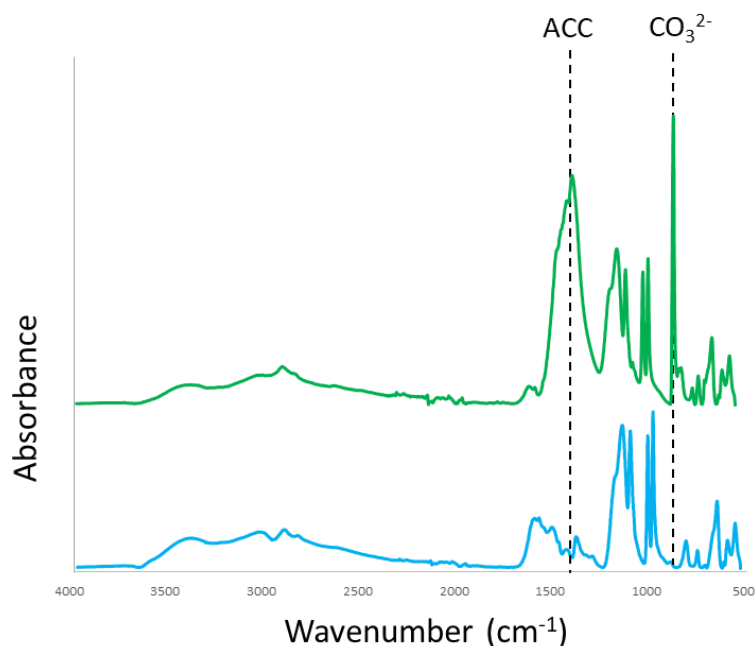


Figure 3.27 FTIR spectra before the core dissolution (green) and after the core dissolution (blue).

The surface chemical composition of the microparticles before and after the LbL procedure and subsequently the core dissolution, was investigated through XPS analysis as well.

The bare microparticles with and without PSS in the structure were compared, and the appearance of the Sulfur ( $S_{2p}$ ) peak ensured the addition of the polyanion ( $CaCO_3$  no PSS and  $CaCO_3/PSS$ ). The formation of the  $CaCO_3$  is evident thanks to the presence of Carbon ( $C_{1s}$ ), Oxygen ( $O_{1s}$ ) and Calcium ( $Ca_{2p}$ ) peaks. The first two constituted the majority of the element content of the microparticles, having an atomic percentage of 46.3% and 40.5% respectively; the synthesis carried out with PSS increased the amount of  $C_{1s}$  which reached 52.4%.

The PEs adsorption was examined in two conditions: after three layers (3L) and at the end of the functionalization (15L). Figure 3.28 shows that the  $C_{1s}$  and  $O_{1s}$  peaks were more intense compared to the other components, while the calcium was hardly detected as the layer deposition proceeded. At the same time Nitrogen ( $N_{1s}$ ) was measured and highlighted in the spectrum, due to the adsorption of the PAH; the sulfur increased its intensity, since the layers of PSS were building up.

The  $\text{CaCO}_3$  inner core was selectively removed leaving the polyelectrolyte outer shell. The calcium peak is absent, while still present are those of  $\text{C}_{1s}$ ,  $\text{O}_{1s}$ ,  $\text{N}_{1s}$  and S (especially  $\text{S}_{2p}$ ) as expected. Being mainly constituted of carbon, the GQDs' signal overlapped with the  $\text{C}_{1s}$  peak of the microparticles and the polyelectrolytes themselves, which rendered very difficult their detection. The  $\text{Si}_{2p}$  peak disappeared.

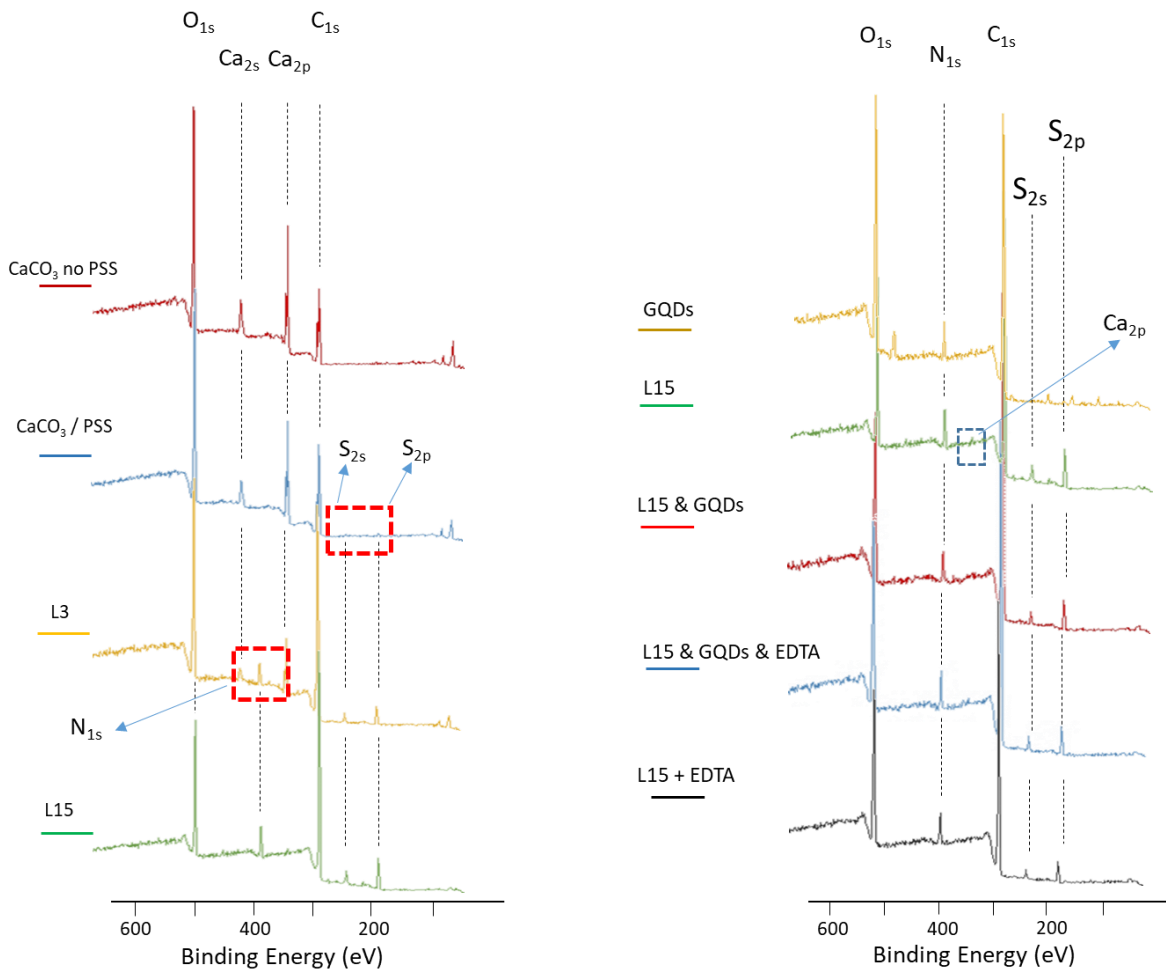


Figure 3.28 XPS survey spectra of the microparticles and microcapsules.

This trend was summarised in table 3.4 that reports the content percentage of each element. Initially S<sub>2p</sub> was absent, but the addition of PSS brought it at 0.8%. Subsequently there was an increase in the percentage values of both S<sub>2p</sub> and N<sub>1s</sub>, which rise from 3.0% and 5% after 3 layers (L3) respectively, to 5.8% and 7.5% with the process conclusion (L15). At the same time the Ca ranged from 10.8% to 0.3%, before completely disappearing after the EDTA step. The other elements remained present, but both S<sub>2p</sub> and N<sub>1s</sub> decreased to 2.9% and 5.5% respectively. The content of O<sub>1s</sub> showed a decreasing pattern along with an increasing trend of the C<sub>1s</sub>.

*Table 3.4 Percentage content of the element constituting the microparticles obtained through different routes and after the functionalization and when the inner core was removed.*

<b>SAMPLE</b>	<b>C<sub>1s</sub> (%)</b>	<b>O<sub>1s</sub> (%)</b>	<b>Ca<sub>2p</sub> (%)</b>	<b>S<sub>2p</sub> (%)</b>	<b>N<sub>1s</sub> (%)</b>
<i>CaCO<sub>3</sub> no PSS</i>	46.3	40.5	13.2	/	/
<i>CaCO<sub>3</sub>/PSS</i>	52.4	35.9	10.8	0.8	/
<i>L3</i>	65.08	23.2	3.7	3.02	5
<i>L15</i>	70.6	15.4	0.3	5.8	7.5
<i>L15 + EDTA</i>	72.8	18.8	/	2.9	5.5

The Zeta Potential was recorded to determine the surface charge of the bare CaCO<sub>3</sub> microparticles as well as to examine the alternation of PEs deposition during the LbL coating process. The colloidal particles showed a constant negative surface charge, regardless of the pH, with values of  $-18.9 \pm 1.42$  mV and  $-21.3 \pm 0.4$  mV; the addition of PSS did not significantly change the zeta potential value, given its negative charge: in this case the value measurement indicated a charge of  $-18.2 \pm 0.75$  mV.

Table 3.5 Zeta potential of naked CaCO<sub>3</sub> microparticles at different pH. The results show a high negative charge regardless of the reaction and the pH

CaCO <sub>3</sub> sample	pH	Zeta Potential (mV)
2 minutes	6.5	- 18.9 ± 1.4
2 minutes	8.5	-21.3 ± 0.4
5 minutes	8.5	-13.6 ± 2.5
PSS addition	8.1	-18.2 ± 0.8

Initially the amount of powder to be coated and introduced in the solution of PAH, at a concentration of 2 mg/mL was 25 mg: the zeta potential went from negative to a positive value of  $13 \pm 1.49$  mV and, following the PSS (2 mg/mL) deposition, it returned to  $-30.5 \pm 2.57$  mV, showing the expected alternate trend.

The amount of microparticles was subsequently raised to 50 and 100 mg for further tests, and the results are displayed in figure 3.29: the zeta potentials showed no positive value when 100 mg were used, although the interaction between the surface and the polymers was occurring, given the increased (less negative) value of zeta potential after depositing the polycation. When the LbL was conducted with 50 mg of CaCO<sub>3</sub> the zeta potential slightly went above the neutral value, reaching  $1.5 \pm 1.1$  mV.

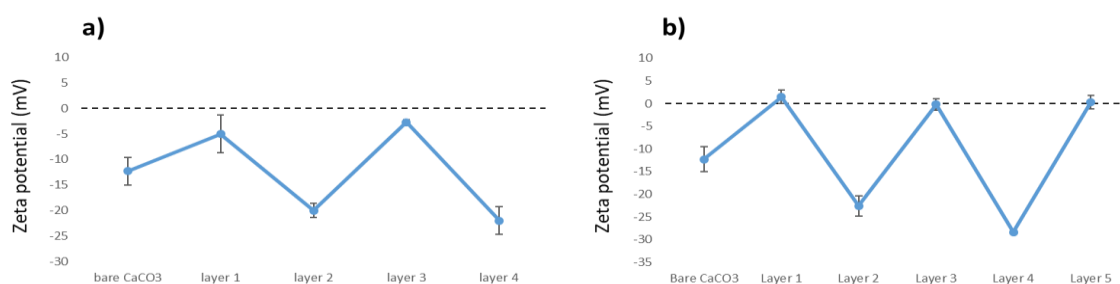


Figure 3.29 Zeta potential trend during LbL assembly. a) 100 mg of microparticles b) 50 mg of microparticles. Polyelectrolyte concentration was kept at 2 mg/mL in a total of 10 mL and the duration of each coating step was set at 10 min.

Figure 3.30 illustrates the zeta potential patterns obtained after 5 layers, after an increase in PEs concentration (5 mg/mL) and in deposition duration (15 minutes): both showed a positive charge after the first PAH film, but the third layer showed a negative

zeta potential, inconsistently with the results previously reported. The weight of the powder coated was 50 mg each. For these experiments, stabilized vaterite microparticles were used and the results showed no significant change between the tests carried out previously.

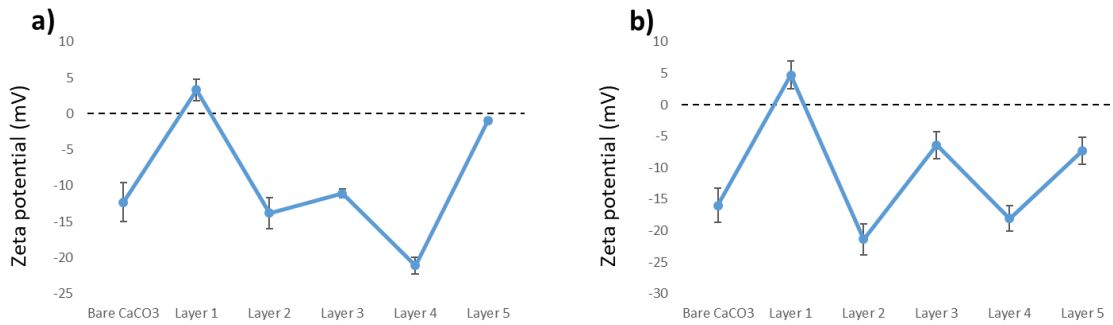


Figure 3.30 PEs concentration was set at 5mg/mL. a) deposition time of 10 minutes. B) deposition time of 15 minutes.

The trends displayed in Figure 3.31 showed a LbL assembly conducted for a higher number of steps; the zeta potential reached the positive value of  $9.7 \pm 2.1$  mV only at the 9<sup>th</sup> layer. The next test was conducted for 15 layers (Figure 3.20 b), as the quantity of powder was raised to 300 mg (so 30 mL of PAH/PSS solutions were used). The multilayer formation took place as depicted in the graph, and the surface charge showed an up and down trend just since the 11<sup>th</sup> layer, before that the zeta potential was not positive.

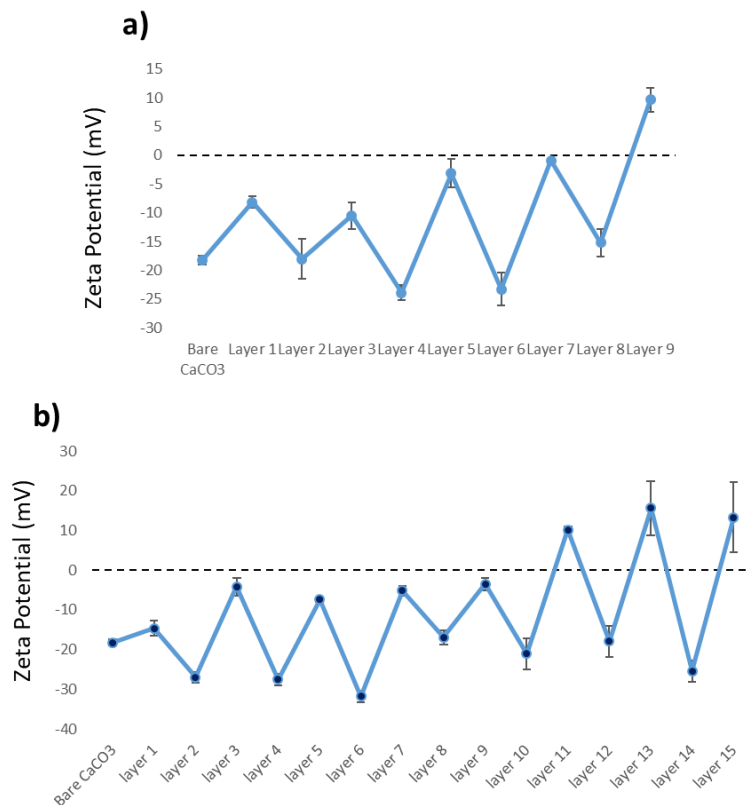


Figure 3.31 Zeta potential trends illustrating the deposition of the PEs. a) 100 mg of CaCO<sub>3</sub> b) 300 mg of CaCO<sub>3</sub>.

The QGDs deposition was qualitatively confirmed comparing the powder obtained subsequently to the PEs adsorption in the two assembly: in fact, as Figure 3.21 b shows, the color was brownish, with respect to the white (Figure 3.21 a) of the particles without the imaging probes incorporated. Same behaviour was displayed in the Figure 3.21 c, taken after the core dissolution and the manufacture of microcapsules.

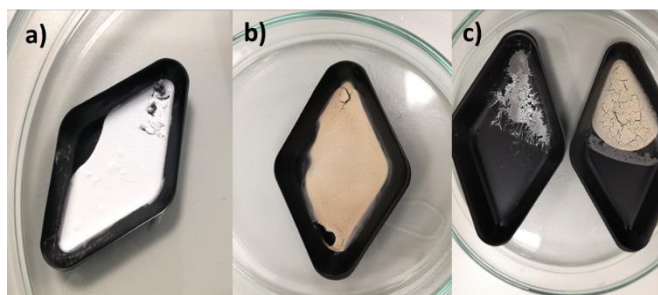
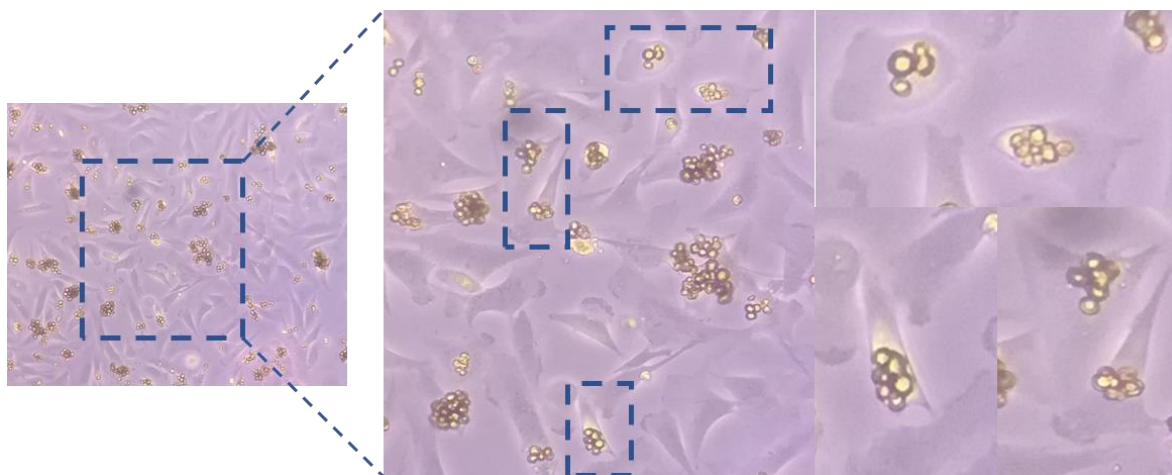


Figure 3.32 Picture a) & b) showing the particles after LbL without and with QGDs respectively. Picture c) showing the product after core dissolution

### 3.2.3 Cellular uptake studies

The Figure 3.33 highlights the ability of the stem cells to internalize the particles without breaking the membrane, regardless of the number of spheres and their size.



*Figure 3.33 Optical microscope images showing that Y201 MSCs internalize the GQDs- functionalized  $\text{CaCO}_3$  microparticles, without showing sign of death, being 70/80% confluent, 24h after the seeding.*

The emission of surface-functionalized microparticles and microcapsules at specific concentration was examined at the confocal microscope. Figure 3.34 confirms the incorporation of the GQDs within the layers and their excitation-dependent emission, given the blue and green color, both at concentration of 0.2 mg/mL and 0.5 mg/mL after 24h of incubation with Y201 MSCs. The cytoskeleton of the cells was stained with Phalloidin (labelled in red) to identify them.

The cells looked highly viable in all the conditions analysed. The pictures confirmed what was stated previously from the optical microscope images analysis, as the particles were found inside the cells, at both concentrations.

It was possible to notice the tendency of the spheres and capsules to agglomerate at higher concentration, enhancing their fluorescent properties.

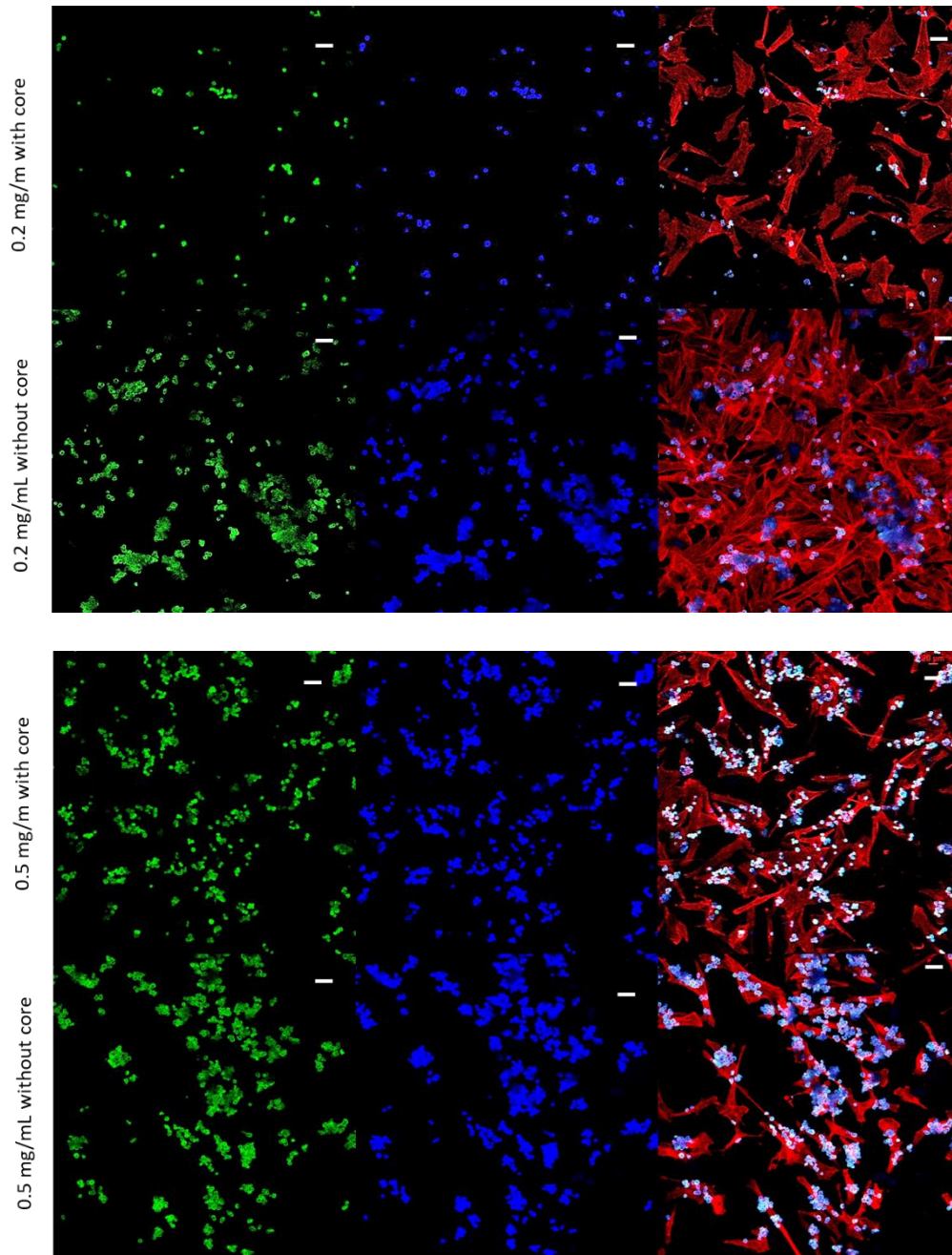


Figure 3.34 Confocal microscope pictures. The two groups of pictures show cell cultured with microparticle and microcapsules, functionalized with GQDs, at different concentrations (0.2 mg/mL and 0.5 mg/mL). Red indicates cytoskeleton; green and blue indicate the fluorescent devices, with excitation-dependent emission. Bar: 40  $\mu\text{m}$

## Chapter 4. Discussion

---

The combination of a therapeutic compound and an imaging probe in a single nano-sized platform would improve the chemotherapeutic effect of the drug, releasing it selectively and in controlled way, and it allows the real time tracking of the device in the body. The nano-size of the device is necessary to exploit the EPR effect and to maximize the final result of the treatment. A theranostic strategy is the encapsulation of a cargo inside an external nano-shell, that shields it from the action of the organism, which recognises it as foreign, and vice versa, so preventing a premature diffusion of the drug which would cause side-effects. The LbL allows to engineer the properties of the shell, its size and composition, allowing the incorporation of biomolecules, targeting ligands and even the imaging probes themselves.

### 4.1 Graphene Quantum Dots

Semiconductor QDs were widely investigated in the biomedical field as imaging probes in theranostic platforms, in order to track real time drug carriers injected throughout the human body. Indeed, their inherent fluorescent properties due to quantum confinement effects, narrow emission spectra and photostability made them an attractive tool for bioimaging and biolabeling in cancer treatment (Matea et al. 2017). Being mainly constituted by heavy metals, such as cadmium and tellurium, they had the tendency to induce cell death, hence new carbon-based nanomaterials were investigated, thanks to their biocompatibility and comparable fluorescence (Lim, Shen, and Gao 2015). In fact, literature reports on GQDs synthesized from rice, coffee, garlic and other food-waste precursors (L. Wang et al. 2016; Zhao et al. 2015).

In this project GQDs obtained from tea waste through a hydrothermal green process were used.

Their morphology was examined via TEM, noticing a circular shape along a wide size distribution, ranging from 4 nm to 100 nm, as analysed in par. 3.1.1 (Figure 3.1). These findings were attributed to the imperfect synthesis procedure, in fact numerous protocols, characterized by different precursors and methods, were investigated and reported in literature, in order to produce size-controlled GQDs (L. Wang et al. 2016). At the same time, these had the tendency to agglomerate in aqueous solutions, in

order to reduce their inherent high surface energy, hence before each test a sonication step was conducted.

Chemical analysis of GQDs was conducted via XPS and FTIR-ATR, and the results demonstrated the presence of hydroxyl, carboxyl and carbonyl groups on their surface which explained their several properties; detection of nitrogen was also recorded indicating the presence of amino groups on the GQDs surface.

Furthermore, these nanostructures showed very good solubility in water, an important and attractive feature: many studies focused on imparting hydrophilic moieties to the particles, to make them suitable for potential injection in the body as imaging probes in a theranostic platform (Zhu et al., n.d.; Generalova et al. 2011). This hydrophilic nature was imparted by numerous oxygenated groups on the surface, such as carboxyls, carbonyls and hydroxyls (Iannazzo et al. 2017). Moreover, this property makes them a perfect candidate for being used as building blocks during the LbL electrostatic assembly. Zeta potential measurement revealed a negative surface charge of the GQDs without being influenced by different pH.

The optical properties were investigated via fluorescence analysis and UV-Vis absorbance. The latter showed two absorption bands centered at 300 nm, which were attributed to  $\pi - \pi^*$  transitions of aromatic ring, confirming the presence detected via FTIR-ATR test (Roy et al. 2014). The absorption abilities were in accordance with what was found examining the fluorescence properties: in fact, the spectra showed peak centered on 380/400nm, consequence of excitations in the UV range (Figure 3.5). The energy bandgaps, related to the quantum confinement effect, were suggested to be one of the main cause of the emission of GQDs (Zheng et al. 2015); another mechanism was related to the chemical and structural surface and edge defects of the carbon-based nanoparticles: as Zhu et al (Zhu et al. 2017) explained, the presence of functional groups on the GQDs imparted photoluminescent properties to them, particularly carboxyl and amide groups were associated to green emission, while hydroxyl to blue emission. Ritter et al (Ritter and Lyding 2009) speculated that zig-zag, armchair and others edge shapes imparted different electronic properties to the nanodots, hence GQDs with different architecture could absorb and emit different wavelengths. The tea waste GQDs presented indeed an excitation-dependent emission (Figure 3.5), which was suggested to be induced from size distribution of the

nanoparticles (Yuan et al. 2014), as well as the surface and edge defects just highlighted.

Since the main aim of the project was the creation of a theranostic platform, one of the most important requirements was the cytocompatibility, depending largely on the cytotoxic effects that GQDs could induce to the organism. Furthermore, a comparison with industrial GQDs with similar optical properties was carried out in order to understand the importance of a green route to manufacture the devices. Live/Dead assay showed for both cell lines high viability at each time point. The Lowest viability was recorded for high concentrations, 500  $\mu\text{g}/\text{mL}$  for the industrial GQDs and 1000  $\mu\text{g}/\text{mL}$  for both GQDs type (Figure 3.6).

Similar results were obtained via Presto Blue assay, which examined the metabolic activity of the cells after 48h of culture. The behaviour of both the cell lines incubated with the green route-manufactured GQDs was consistent with Live/Dead results, so a decreasing cellular activity at high concentrations was detected, being completely absent at 1  $\text{mg}/\text{mL}$ . The metabolic activity of the cells incubated with the industrial GQDs was inexistent at 500  $\mu\text{g}/\text{mL}$  and 1  $\text{mg}/\text{mL}$ . This concentration-dependent behavior was consistent with several investigations reported in literature (Sui et al. 2016).

The different behaviours at high concentrations may be attributed to the manufacturing procedures, since the tea waste-derived GQDs were synthesized without strong acids, which induced cytotoxic effects. Graphene-based structures, such as GQDs or Graphene Oxide (GO), induce oxidative stress, due to the production of ROS which are considered the main cause of apoptosis (Chong et al. 2014).

Moreover, the size of GO, greater than GQDs', was considered a cause of cell death (Wu et al. 2013); we consequently speculated that their tendency to aggregate may prevented the internalization of the nanoparticles and, as higher quantity of nanostructures comprehensively would produce bigger clusters, it affected the cell viability.

## 4.2 Bioimaging analysis

The GQDs' imaging properties were analysed without further functionalisation, which would have imparted ligand-receptor abilities and enhanced the cellular internalization; for instance Biotin was used as targeting moiety as well as Hyaluronic Acid (Abdullah-Al-Nahain et al. 2013) or folic Acid (Chiu et al. 2016): the cellular uptake was significantly higher than the unfunctionalised nanoparticles.

We wanted to assess if the fluorescence could be concentration-dependent, consequently we chose two concentrations that needed to be low enough not to induce death to the cells: we cultured Y201 MSCs with 200 and 50  $\mu\text{g}/\text{mL}$ , in accordance with the results obtained from the biocompatibility tests.

The excitation-dependent emission of the GQDs was difficult to assess, probably due to the lower amount entering the membrane. In fact, the aggregation of CDs would enhance their fluorescent properties, proportionally to the amount of nanoparticles (Anilkumar et al. 2013), thus, as the green emission intensity was demonstrated to be weaker than the blue one, the quantity of nanodots was critical to obtain longer wavelength emission. The nanoparticles were fluorescent when internalized by the cells and, when exposed to UV excitation, these exhibited bright blue emission, consistently with the optical analysis previously assessed. The GQDs were found inside the membrane: it was demonstrated and reported in literature that caveolae-mediated endocytosis was the main mechanism of GQDs internalization, although other pathways were investigated (Wu et al. 2013).

## 4.3 $\text{CaCO}_3$ microparticles synthesis and protocol optimization

Layer by Layer was widely studied in numerous fields thanks to its simplicity and versatility. The alternative deposition of two oppositely charged PEs allows the use of various building blocks, exploiting their charge and manufacturing nano-sized multilayers, with controlled thickness and specific properties (Xiao et al. 2016).

An attractive application is the creation of a multilayer surrounding a sacrificial inner core (micro or nano-sized), with the final purpose to manufacture a capsule able to carry a cargo inside or within the layers and able to be stimuli-responsive (Johnston et al. 2006).

In this work we manufactured and optimized the synthesis protocol of colloidal microparticles made out of  $\text{CaCO}_3$ , the deposition of a multilayer film and the incorporation of GQDs as imaging probes via LbL assembly, in order to eventually fabricate a theranostic system.

The procedure was conducted at three different time points, in order to understand the influence of time on the size of the microparticles, speculating that longer period would have resulted in bigger particles. When the reagent solutions were mixed together, the crystallization of the inorganic salt occurred almost instantly as an immediate reaction took place and the initial transient amorphous calcium carbonate (ACC) was formed (Addadi, Raz, and Weiner 2003).

As highlighted before (par. 3.2.1), regardless of the length of the procedure, the powders obtained drying at RT were characterized by the presence of cubic-shaped crystals that were associated with calcite, one of the phases of the  $\text{CaCO}_3$ . In fact,  $\text{CaCO}_3$  is a polymorph, so it exists in nature under various forms with the same chemical structure, but different crystal form which influences the mechanical and physical properties of the material (Tai and Chen 1998).

Vaterite, aragonite and calcite are the three phases of calcium carbonate with respectively growing thermodynamic stability in water. Vaterite is metastable and has the highest solubility, and as demonstrated, tends to turn into the more stable calcite as soon as it's immersed in water (Trushina et al. 2014). This was confirmed by the chemical and morphological tests performed, since the amount of crystals in the product was strongly reduced when the solvent evaporation was carried out at  $37^\circ\text{C}$ : indeed, the microspheres were the majority of the content in the sample synthesized for 2 and 5 min, while a opposite behaviour could be noticed when the reaction was conducted for 10 min (Figure 3.9).

The recrystallization process may take place during the mixing of the reagents and consequently, an important part of this work focused on the stabilization of the vaterite polymorph, in order to avoid the transformation into calcite during the synthesis and, more importantly, during the LbL assembly.

It has been proved that the first product of the reaction were nano-granules, of  $10 \div 70$  nm diameter of ACC and their coalescence would finally create porous sphere-shaped microcrystals and the pores range from 20 nm to 60 nm (Won et al. 2010).

Previous researches used additives, organic or inorganic, to prevent this transformation to happen. For instance carboxyl-functionalised carbon nanotubes (CNTs) stabilized the vaterite phase, acting as nucleation site and coating the particles' surface; when no CNTs were introduced in the reaction, the product transformed in the more stable calcite after 30 minutes (Li and Gao 2007). In fact, FTIR-ATR spectra of the samples showed the calcite peak at  $711\text{ cm}^{-1}$  increasing its magnitude along with the duration of the reaction. This was indicative of the unstable nature of the vaterite in water: it was determined that the complete transformation of vaterite to calcite takes around 5 h (X. Wang et al. 2009).

In this work we introduced PSS (1mg/mL), into the  $\text{Na}_2\text{CO}_3$  solution and the synthesis was carried out for 100 seconds and dried in incubator. We obtained vaterite microparticles at those conditions, without obtaining calcite residuals. Furthermore, it was also demonstrated that the metastable phase of  $\text{CaCO}_3$  was particularly present at a temperature range of  $20^\circ\text{C}$  and  $40^\circ\text{C}$  (J. Chen and Xiang 2009). Thus, the influence of temperature was also tested at  $35^\circ\text{C}$  with and without PSS.

XPS and FTIR analysis confirmed the presence of the polyanion in the structure with the appearance of peaks characteristic of the polymer, while the temperature rise did not influence the spectra (Figure 3.24). The former detected sulfur at the atomic percentage of 0.8% (Figure 3.28), while the latter showed peaks attributed to symmetric stretching vibration of the  $\text{SO}_3^-$ , which could only be attributed to the binding of PSS with calcium and carbonate ions through hydrogen bonds and electrostatic forces (Kittitheeranun et al. 2015).

Previous works explained that organic polymers tend to coat the vaterite nanoparticles which tend, as the reaction proceeds, to aggregate and to form a bigger microparticle (Imai et al. 2012). Moreover, the negative charge of the polyanion created an electrostatic interaction with the bivalent calcium cations ( $\text{Ca}^{2+}$ ), strengthening the overall molecular structure, preventing the recrystallization in a more stable form (X. Wang et al. 2009). These concepts were confirmed by the tests conducted to examine the morphology and the chemical composition of the product. FTIR-ATR analysis demonstrated that all three reactions favored the presence of the vaterite with respect to the calcite phase, and a strong presence of ACC was detected. SEM pictures, at the same time, proved the absence of rhombohedral crystals in accordance with the

previous assessment (Figure 3.10).

However, the temperature had the effect of changing the morphology of the product since the manufactured particles possessed a cauliflower-like shape: the temperature favoured the nucleation but it caused the nuclei to collide and when the coalescence occurred, the round particles adhered on the surface, anisotropically growing and conferring the unwanted shape (Trushina, Bukreeva, and Antipina 2016; Tai and Chen 1998).

As on one side, with the use of PSS, we managed to obtain perfect circular and porous microparticles with an average diameter of  $3.49 \pm 1.09 \mu\text{m}$ , we needed also to ensure their stability, in order to prevent the recrystallization process. The PSS managed to stabilize the vaterite through different chemical and physical means, previously cited, and there was no transformation consequently to the immersion of the powder in water for 4h. SEM pictures (Figure 3.11) showed no sign of morphology shift of either the products, and the FTIR spectra confirmed these findings, as the peak at  $744 \text{ cm}^{-1}$ , typical of vaterite, was clearly more intense than the  $711 \text{ cm}^{-1}$  (calcite).

The same was determined for the samples synthesized at  $35^\circ\text{C}$ : the temperature rise prevented the morphological transformation.

These findings suggested that RT was the better one in order to obtain spherical particles, suitable to be used as sacrificial template aiming to fabricate a polyelectrolyte microcapsule as theranostic platform.

## 4.4 LbL functionalisation

The functionalisation was conducted changing numerous variables, that could influence the PEs adsorption, hence the final shell and its properties.

The particles' surface charge resulted to be highly negative, with the highest value of  $-21.3 \pm 0.4 \text{ mV}$ ; the measurements were performed with the product fabricated with and without PSS, noticing no significant change in the results, which meant that the addition of the organic polymer did not lead to a change in zeta potential: the amount used to stabilize the vaterite was sufficient to accomplish this objective without affecting any physical property. The negative charge was due to the presence of  $\text{CO}_3^{2-}$

on the surface at a higher density compared to the  $\text{Ca}^{2+}$  ions; the balance between anions and cations in the structure determined the charge, but clearly the addition of the polyanion doesn't affect the magnitude of the zeta potential, being at such a lower concentration with respect to the total powder of  $\text{CaCO}_3$  (Volodkin, Larionova, and Sukhorukov 2004; Nagaraja, Pradhan, and McShane 2014).

The first tests were conducted changing the amount of particles coated, using 25, 50 and 100 mg of  $\text{CaCO}_3$  with the PEs solutions' concentrations set at 2 mg/mL and the deposition time at 10 min. Except for the lowest quantity, which zeta potential reversed with the adsorption of PAH and PSS, reaching 13 mV, the surface charge did not change polarity, although the interaction between the PAH and the  $\text{CaCO}_3$  was detected, as the charge increased (less negative) after each deposition: both polymers were adsorbed via electrostatic interaction but did not saturate the  $\text{CaCO}_3$  microparticles surface (Figure 3.29). These findings related the zeta potential recorded with the amount of microparticles used, hence the ability of the PEs to saturate the external surface. Moreover, since the vaterite stabilization was yet to be optimized, the smooth surface of the rhombohedral calcite crystals may have prevented a sufficient adsorption of the PEs (Cölfen and Antonietti 1998). The successive stabilization of the vaterite phase would avoid the shape transformation and helped to improve the interaction between the polyelectrolytes and the particles.

After the stabilization of the spherical shape of the vaterite, the porosity of the microparticles had to be taken into account. We suggested that the first few layers were not able to completely saturate the surface because the polyelectrolyte molecules entered the pores and tended to overlap without creating a stratified multilayer and after 3 layers the microparticles had a very rough and porous surface (Figure 3.12). The zeta sizer was therefore not able to measure a positive charge, because the negativity of the particles was overcoming the positivity of the PAH. In fact, Yashchenok et al (Yashchenok et al. 2013) found FITC-dextran molecules, polyelectrolyte, inside the core through confocal imaging, confirming the porosity of the structure, while they could not be seen inside the calcite crystals.

It was also proposed that the entrapment of the PEs molecules in the pores would prevent the recrystallization of the  $\text{CaCO}_3$  (Volodkin, Larionova, and Sukhorukov 2004), alongside with the addition polyanion during the synthesis.

XPS detected  $N_{1s}$  signal after 3 layers adsorption, which increased in its content after 15 layers deposition, demonstrating that an interaction between the positively-charged PAH and the material was occurring as zeta potential analysis showed. One of the variables not yet mentioned was the centrifugation steps between each PE deposition. Indeed, the recollection of the powders and the removal of any unbound polymer's molecule were necessary, however, this passage could cause some polyelectrolyte molecules to detach (high speed and long durations) and there was also the risk to lose an important part of the content within the supernatant (low speed and short durations) (Goryacheva et al. 2015). Furthermore, previous works highlighted the influence of the centrifuge on the colloids aggregation, which had to be avoided (Richardson, Bjornmalm, and Caruso 2015). Some researches proposed the use of the sonicator to prevent the agglomeration of microparticles (Biswas, Nagaraja, and McShane 2014). However, since the microspheres are the result of  $CaCO_3$  nanoparticles coalescence, we speculated the possibility that the sonication may break the structure, therefore we did not consider the use of the mentioned protocol. Several LbL assembly were carried out in order to find the better tradeoff between the wasted material and the precipitated one: 3 total centrifugations of 2.5 minutes at a speed of 1200 rpm were finally established. These parameters would have ensured the precipitation of the majority of the colloidal microparticles and their washing, without risking to damage the nanocoating or the structures themselves. SEM pictures in fact, displayed that the microspheres shape was maintained and a thick shell was built (Figure 3.12).

At the same time, the results obtained from the zeta potential measurements, forced an additional change in the protocol, as both the PEs concentration and the time of deposition were raised, respectively, to 5 mg/mL and 15 minutes.

Various researches assessed that the weight of the PEs adsorbed increases along with the concentration, and is directly proportional to the duration of the deposition (Chai et al. 2017; Xiao et al. 2016).

As soon as the particle pores and the gaps were completely saturated, the surface became smoother and homogeneous and the zeta potential values alternated in response to the LbL deposition. The analysis of the zeta potential trend determined that the surface saturation started not before the 9<sup>th</sup> layer or 11<sup>th</sup> layer (Figure 3.31).

The difference was again attributed to the amount of the particles coated in the tests, 100mg and 300 mg respectively. Comprehensively, the former began to show an alternative pattern two layers earlier than the latter.

For further confirmation of the PEs adsorption QCM-D analysis was performed, first with the only PEs solutions and after with the inclusion of the GQDs (Figure 3.21).

As expected, a decrease in resonance frequency was recorded as the layers deposited; when the washing step was conducted another shift of frequency was detected, this time with a reversed slope, which indicated a change in mass; by applying the Sauerbrey equation, the mass shift was modelled in accordance with the  $\Delta f$ , due to the detachment of weakly bound polymers. At the same time the energy dissipation was measured: this value was related to the viscoelastic properties and lower variations were associated with a more rigid film (Tonda-Turo, Carmagnola, and Ciardelli 2018). The results obtained demonstrated the rigidity of the nanocoating composed by the alternation of PAH and PSS, and the low amount of water in between the PEs.

Subsequent measures via SEM analysis revealed that the external PE film after 15 layers was  $0.45 \pm 0.11 \mu\text{m}$  thick, which indicated an average single layer thickness of around 30 nm, which was 3 times bigger than reported in literature (Volodkin et al. 2004). We supposed that after few layers, the concentration of the PEs and their molecule conformation, along with the time of deposition, would create a layer that as the adsorption went on, would increase in thickness achieving higher magnitudes than those reported in literature. The thickness measured was in contradiction with the QCM-D results as displayed in par. 3.2.2.1 and the different substrates were considered to be the main cause of inconsistency: the flat gold sensor substrate was eventually saturated more easily, and the molecules structurally organized more ordered and with different conformation compared to the spherical and porous  $\text{CaCO}_3$  surface.

The immersion in an EDTA solution had the expected effect to dissolve the  $\text{CaCO}_3$  microparticles solid core, without visibly affecting the PE shell. The EDTA has a strong affinity with  $\text{Ca}^{2+}$  ions (Liu and Picart 2016), so to create complexes and destroying the bonds with carbonate ions. Via diffusion, the various elements and complexes escaped through the porous PE matrix causing the consequent  $\text{CaCO}_3$  core dissolution (Volodkin, Larionova, and Sukhorukov 2004).

The XPS analysis showed a decrease in content of sulfur and nitrogen consequently the EDTA core dissolution, which could be attributed to the possibility of the external wall degradation due to the immersion in the solution and the continuous stirring, along with the centrifugation leading to the detachment of PEs' molecules. Moreover, it could be attributed to the process described above, regarding the interaction between calcium and EDTA. Calcium ions bind with PSS and with carbonate ions which, at the same time, bind with PAH via electrostatic interactions. The removal of the inner core will subsequently remove PEs molecules, hence the reduction in the elements content. Calcium had a similar trend showed in the XPS analysis: its content slowly decreased until finally disappearing after the EDTA immersion. XPS equipment detects signal of few nanometers, so the layering of PSS and PAH would probably hid the signal. When the inner core was removed, calcium was dissolved, although we could speculate that some was still present and bound to the PSS, but too weak to be detected.

FTIR analysis confirmed this result, given the disappearance of the main peaks associated to the ACC and to the  $\text{CO}_3^{2-}$  bond.

Via LbL adsorption the GQDs were embedded on the surface of the microparticles following the protocol previously optimized. The deposition of the nanostructures was assessed first via SEM picture analysis: comparison between the average diameters of particles coated with and without GQDs was carried out, showing significant difference (Figure 3.15). This was attributed to the size of the GQDs that were clearly incorporated within the layers. QCM-D analysis instead did not show this behavior, as the thickness measured was comparable to the bare PEs deposition: the low GQDs concentration, along with a different substrate probably prevented a large deposition of the nanostructures. Their adsorption was detected by the energy dissipation factor as it showed different behavior from the introduction of the GQDs: in fact, since the dissipation is indicative of how soft the layer is, the results obtained suggested a change within the layers and probably the small structures were able to retain water in between their lattices (Q. Chen et al. 2010).

Regarding the fluorescent abilities, as Generalova et al reported (Generalova et al. 2011), this methodology resulted perfectly suitable to create a imaging probe, whose fluorescence properties were enhanced proportionally with the adsorption of the

layers. Moreover, they demonstrated that the last layer could improve the emission intensity of the QDs, creating a sort of passivation layer, which many reports assessed that increases the Quantum Yield of the nanodots (Ding, Zhu, and Tian 2014); in this project, the last layer deposited was PAH, to impart a positive charge to the microparticles and eventually enhance their internalization.

Subsequently to the LbL assembly of the nanocoating, CaCO<sub>3</sub> microparticles and microcapsules were introduced at concentrations of 0.2 mg/mL and 0.5 mg/mL in Y201 MSCs culture, in order to assess the actual suitability of this system to be used as theranostic platform. Previous work (Zhang et al. 2012) demonstrated the ability of stem cells to internalize theranostic devices, without interfering with their functionalities.

The results were very promising given the high viability of the cells and their ability to uptake the drug carriers without dying. The confocal images taken demonstrated the excitation-dependent emission of the GQDs, confirming what was already assessed from the fluorescence test (Figure 3.34). The LbL assembly increased sensibly the number of nanodots on the microparticle, which allowed the bioimaging through different colors, blue, green and red.

## 4.5 Nanoparticles synthesis

As proof of concept, the last objective was the creation of nano-sized CaCO<sub>3</sub> particles, in order to exploit the EPR effect. Theranostic platforms have indeed the requirement to be targeted, to selectively reach a desired site, especially cancer environment, and being able to release the therapeutic compound in situ, without risking side effects. The passive targeting is based on the mentioned EPR effect, so nanoparticles could extravasate through the fenestrations in between the endothelial cells of cancer vessels (Bae and Park 2011).

The structures manufactured had in fact an average diameter of 4 μm, while the creation of the multilayer film with the incorporation of GQDs pushed the size up to 6 μm. This numbers required a necessary reduction in size, maintaining the stability previously achieved, as well as the shape and porosity.

Initially supersaturated reagent solutions were used: the supersaturation favors the

nucleation with respect to the growth of microparticles, which means that the speed of nuclei formation is faster than their size growth (Flaten, Seiersten, and Andreassen 2009). This process managed to decrease the diameter to 1.6  $\mu\text{m}$  without losing in porosity and morphology (Figure 3.17). However, the nanoscale wasn't reached yet. The idea was to find a way to prevent the diameters to rise after the initial nanoparticles agglomeration.

Consequently a second procedure was tested; previous studies investigated the effects of polyols in the creations of  $\text{CaCO}_3$ , particularly the presence of hydroxyl groups created a network of molecules bound via hydrogen bindings to calcium ions acting as site of nuclei formation (Trushina, Bukreeva, and Antipina 2016). Indeed, we dissolved the reagents in a glycerol-based solvent (83.3% v/v) which possesses 3 alcohol functional groups, examining the powders obtained via 3 different reactions.

Two synthesis were carried out changing the duration (2 and 50 minutes), and the effects were analysed via SEM: there was no difference between the batches since both presented rhombohedral crystals, which we supposed made of calcite.

We concluded that the glycerol did not stabilize the vaterite form, thus the third reaction was conducted with the addition of PSS and the outcome was reversed as the sample was constituted by nano-sized particles, with an average diameter of 720 nm, characterized by a spherical morphology and high porosity (Figure 3.18).

The coupling between hydroxyl groups and  $\text{Ca}^{2+}$  ions, as described above, favored a high rate of nucleation preventing the growth of the particle; the presence of a supersaturated solution would have resulted in a faster nucleation, but when the glycerol functional groups were all occupied the remaining free calcium and carbonate ions would have participated to the growth of the particles size: for this reason a smaller salt precursors concentration was used, specifically 0.1M, so to limit as much as possible the increase in diameters (Trushina, Bukreeva, and Antipina 2016).

The use of PSS we suggested had the same effect it had with the microparticles, so it strengthened the bindings that formed the  $\text{CaCO}_3$ , but it was impossible to assess its influence on the particles size.

## Chapter 5. Conclusion and future perspectives

---

The theranostic approach is an attractive strategy to improve drawbacks of the conventional cancer therapies, such as poor selectivity and biodistribution, low doses and side-effects.

In this work we developed polyelectrolyte microcapsules starting from calcium carbonate microparticles used sacrificial template and functionalised via LbL electrostatic assembly, with the incorporation of Graphene Quantum Dots within the nanocoating.

GQDs were manufactured via an environmentally-friendly green-route starting from tea waste as precursor. This process ensured their biocompatibility which was demonstrated to be concentration-dependent up to 500  $\mu\text{g}/\text{mL}$ .

$\text{CaCO}_3$  microparticles were fabricated and the vaterite polymorph stabilization was effectively accomplished via the introduction of 1 mg/mL of PSS in the reaction, preventing the transformation into the more thermodynamically stable calcite. The EDTA immersion was able to dissolve the inner  $\text{CaCO}_3$  core, after the LbL functionalisation, manufacturing a microcapsule without affecting the bioimaging properties. In fact, the LbL assembly was perfectly suitable to create a strong and stable shell, incorporating within the nanolayers the negatively charged GQDs.

These devices were indeed able to be internalized by the cells and to be fluorescent, showing an excitation-dependent emission. This last feature will be a major topic of research, since the GQDs need to have a narrow wavelength emission, in order to be used in theranostic system in combination with other labels.

The potentiality of this approach to be used as passively-targeted nanotheranostic device was demonstrated, as a reduction in diameter down to 320 nm was accomplished, although a smaller size distribution has to be achieved in future works. The micro and nanoparticles can potentially be loaded with one or more drugs, exploiting the diffusion through the pores and accomplishing the therapeutic effect in a controlled way, avoiding burst release. Furthermore, the LbL can also be used to impart active targeting moieties to the theranostic platforms, via deposition of biomolecules with ligand-receptor interaction abilities.

In conclusion, future researches should focus on the investigation of the different parameters that influences the outcome of the reactions, which include the reagent solutions concentrations and the use of additives such as polyols, so to manufacture targeted theranostic nano-sized capsule as new cancer treatment.



## References

- Abdelhamid, Ahmed S, Maged W Helmy, Shaker M Ebrahim, Mohammed Bahey-El-Din, Dina G Zayed, Esmat A Zein El Dein, Sanaa A El-Gizawy, and Ahmed O Elzoghby. 2018. 'Layer-by-Layer Gelatin/Chondroitin Quantum Dots-Based Nanotheranostics: Combined Rapamycin/Celecoxib Delivery and Cancer Imaging'. *Nanomedicine* 13 (14): nnm-2018-0028. <https://doi.org/10.2217/nnm-2018-0028>.
- Abdullah-Al-Nahain, Jung-Eun Lee, Insik In, Haeshin Lee, Kang Dae Lee, Ji Hoon Jeong, and Sung Young Park. 2013. 'Target Delivery and Cell Imaging Using Hyaluronic Acid-Functionalized Graphene Quantum Dots'. *Molecular Pharmaceutics* 10 (10): 3736–44. <https://doi.org/10.1021/mp400219u>.
- Addadi, L., S. Raz, and S. Weiner. 2003. 'Taking Advantage of Disorder: Amorphous Calcium Carbonate and Its Roles in Biomineralization'. *Advanced Materials* 15 (12): 959–70. <https://doi.org/10.1002/adma.200300381>.
- Anilkumar, Parambath, Li Cao, Jing-Jiang Yu, Kenneth N. Tackett, Ping Wang, Mohammed J. Meziari, and Ya-Ping Sun. 2013. 'Crosslinked Carbon Dots as Ultra-Bright Fluorescence Probes'. *Small* 9 (4): 545–51. <https://doi.org/10.1002/sml.201202000>.
- Antipov, Alexei A, Dmitry Shchukin, Yuri Fedutik, Alexander I Petrov, Gleb B Sukhorukov, and Helmuth Möhwald. 2003. 'Carbonate Microparticles for Hollow Polyelectrolyte Capsules Fabrication'. *Colloids and Surfaces A: Physicochemical and Engineering Aspects* 224 (1–3): 175–83. [https://doi.org/10.1016/S0927-7757\(03\)00195-X](https://doi.org/10.1016/S0927-7757(03)00195-X).
- Bae, You Han, and Kinam Park. 2011a. 'Targeted Drug Delivery to Tumors: Myths, Reality and Possibility'. *Journal of Controlled Release* 153 (3): 198–205. <https://doi.org/10.1016/j.jconrel.2011.06.001>.
- . 2011b. 'Targeted Drug Delivery to Tumors: Myths, Reality and Possibility'. *Journal of Controlled Release* 153 (3): 198–205. <https://doi.org/10.1016/j.jconrel.2011.06.001>.
- Biswas, Aniket, Ashvin T. Nagaraja, and Michael J. McShane. 2014. 'Fabrication of Nanocapsule Carriers from Multilayer-Coated Vaterite Calcium Carbonate Nanoparticles'. *ACS Applied Materials & Interfaces* 6 (23): 21193–201. <https://doi.org/10.1021/am5061195>.
- Bray, Freddie, Ahmedin Jemal, Nathan Grey, Jacques Ferlay, and David Forman. 2012. 'Global Cancer Transitions According to the Human Development Index (2008–2030): A Population-Based Study'. *The Lancet Oncology* 13 (8): 790–801. [https://doi.org/10.1016/S1470-2045\(12\)70211-5](https://doi.org/10.1016/S1470-2045(12)70211-5).
- Bwatanglang, Ibrahim Birma, Faruq Mohammad, Nor Azah Yusof, Jaafar Abdullah, Noorjahan Banu Alitheen, Mohd Zubir Hussein, Nadiah Abu, et al. 2016. 'In Vivo Tumor Targeting and Anti-Tumor Effects of 5-Fluororacil Loaded, Folic Acid Targeted Quantum Dot System'. *Journal of Colloid and Interface Science* 480 (October): 146–58. <https://doi.org/10.1016/j.jcis.2016.07.011>.
- Cai, Xiaoli, Yanan Luo, Weiyang Zhang, Dan Du, and Yuehe Lin. 2016. 'PH-Sensitive ZnO Quantum Dots–Doxorubicin Nanoparticles for Lung Cancer Targeted Drug Delivery'. *ACS Applied Materials & Interfaces* 8 (34): 22442–50. <https://doi.org/10.1021/acsami.6b04933>.
- Cao, Li, Mohammed J. Meziari, Sushant Sahu, and Ya-Ping Sun. 2013. 'Photoluminescence Properties of Graphene versus Other Carbon Nanomaterials'. *Accounts of Chemical Research* 46 (1): 171–80. <https://doi.org/10.1021/ar300128j>.
- Chai, Fujuan, Linlin Sun, Xinyi He, Jieli Li, Yuanfen Liu, Fei Xiong, Liang Ge, Thomas J Webster, and Chunli Zheng. 2017a. 'Doxorubicin-Loaded Poly (Lactic-Co-Glycolic Acid) Nanoparticles Coated with Chitosan/Alginate by Layer by Layer Technology for Antitumor Applications'. *International Journal of Nanomedicine* Volume 12 (March): 1791–1802. <https://doi.org/10.2147/IJN.S130404>.
- . 2017b. 'Doxorubicin-Loaded Poly (Lactic-Co-Glycolic Acid) Nanoparticles Coated with Chitosan/Alginate by Layer by Layer Technology for Antitumor Applications'. *International Journal of Nanomedicine* Volume 12 (March): 1791–1802. <https://doi.org/10.2147/IJN.S130404>.
- Chen, Daiqin, Casey A. Dougherty, Kaicheng Zhu, and Hao Hong. 2015. 'Theranostic Applications of Carbon Nanomaterials in Cancer: Focus on Imaging and Cargo Delivery'. *Journal of Controlled Release* 210 (July): 230–45. <https://doi.org/10.1016/j.jconrel.2015.04.021>.
- Chen, J., and L. Xiang. 2009. 'Controllable Synthesis of Calcium Carbonate Polymorphs at Different Temperatures'. *Powder Technology* 189 (1): 64–69. <https://doi.org/10.1016/j.powtec.2008.06.004>.
- Chen, Qiang, Wei Tang, Dingzhong Wang, Xiaojie Wu, Na Li, and Feng Liu. 2010. 'Amplified QCM-D Biosensor for Protein Based on Aptamer-Functionalized Gold Nanoparticles'. *Biosensors and Bioelectronics* 26 (2): 575–79. <https://doi.org/10.1016/j.bios.2010.07.034>.
- Chiu, Sheng-Hui, Gangaraju Gedda, Wubshet Mekonnen Girma, Jem-Kun Chen, Yong-Chien Ling, Anil V. Ghule, Keng-Liang Ou, and Jia-Yaw Chang. 2016. 'Rapid Fabrication of Carbon Quantum Dots as Multifunctional Nanovehicles for Dual-Modal Targeted Imaging and Chemotherapy'. *Acta Biomaterialia* 46 (December): 151–64. <https://doi.org/10.1016/j.actbio.2016.09.027>.
- Choi, Ki Young, Gang Liu, Seulki Lee, and Xiaoyuan Chen. 2012. 'Theranostic Nanoplatforams for Simultaneous Cancer Imaging and Therapy: Current Approaches and Future Perspectives'. *Nanoscale* 4 (2): 330–42. <https://doi.org/10.1039/C1NR11277E>.

- Chong, Yu, Yufei Ma, He Shen, Xiaolong Tu, Xuan Zhou, Jiaying Xu, Jianwu Dai, Saijun Fan, and Zhijun Zhang. 2014. 'The in Vitro and in Vivo Toxicity of Graphene Quantum Dots'. *Biomaterials* 35 (19): 5041–48. <https://doi.org/10.1016/j.biomaterials.2014.03.021>.
- Cölfen, Helmut, and Markus Antonietti. 1998. 'Crystal Design of Calcium Carbonate Microparticles Using Double-Hydrophilic Block Copolymers'. *Langmuir* 14 (3): 582–89. <https://doi.org/10.1021/la970765t>.
- Constantine, Celeste A., Kerim M. Gattás-Asfura, Sarita V. Mello, Gema Crespo, Vipin Rastogi, Tu-Chen Cheng, Joseph J. DeFrank, and Roger M. Leblanc. 2003. 'Layer-by-Layer Biosensor Assembly Incorporating Functionalized Quantum Dots'. *Langmuir* 19 (23): 9863–67. <https://doi.org/10.1021/la035237y>.
- Cui, Honggang, and Jun Wang. 2016. 'Progress in the Development of Nanotheranostic Systems'. *Theranostics* 6 (7): 915–17. <https://doi.org/10.7150/thno.16153>.
- Dai, Yunlu, Can Xu, Xiaolian Sun, and Xiaoyuan Chen. 2017. 'Nanoparticle Design Strategies for Enhanced Anticancer Therapy by Exploiting the Tumour Microenvironment'. *Chemical Society Reviews* 46 (12): 3830–52. <https://doi.org/10.1039/C6CS00592F>.
- Deng, Aipeng, Xi Kang, Jing Zhang, Yang Yang, and Shulin Yang. 2017. 'Enhanced Gelation of Chitosan/ $\beta$ -Sodium Glycerophosphate Thermosensitive Hydrogel with Sodium Bicarbonate and Biocompatibility Evaluated'. *Materials Science and Engineering C* 78: 1147–54. <https://doi.org/10.1016/j.msec.2017.04.109>.
- Deng, Zhou J., Stephen W. Morton, Elana Ben-Akiva, Erik C. Dreaden, Kevin E. Shopsowitz, and Paula T. Hammond. 2013. 'Layer-by-Layer Nanoparticles for Systemic Codelivery of an Anticancer Drug and siRNA for Potential Triple-Negative Breast Cancer Treatment'. *ACS Nano* 7 (11): 9571–84. <https://doi.org/10.1021/nn4047925>.
- Derfus, Austin M., Warren C. W. Chan, and Sangeeta N. Bhatia. 2004. 'Probing the Cytotoxicity of Semiconductor Quantum Dots'. *Nano Letters* 4 (1): 11–18. <https://doi.org/10.1021/nl0347334>.
- Dierendonck, Marijke, Stefaan De Koker, Riet De Rycke, and Bruno G. De Geest. 2014. 'Just Spray It – LbL Assembly Enters a New Age'. *Soft Matter* 10 (6): 804–7. <https://doi.org/10.1039/C3SM52202D>.
- Ding, Changqin, Anwei Zhu, and Yang Tian. 2014a. 'Functional Surface Engineering of C-Dots for Fluorescent Biosensing and in Vivo Bioimaging'. *Accounts of Chemical Research* 47 (1): 20–30. <https://doi.org/10.1021/ar400023s>.
- . 2014b. 'Functional Surface Engineering of C-Dots for Fluorescent Biosensing and in Vivo Bioimaging'. *Accounts of Chemical Research* 47 (1): 20–30. <https://doi.org/10.1021/ar400023s>.
- Dreaden, Erik C., Stephen W. Morton, Kevin E. Shopsowitz, Jae-Hyeok Choi, Zhou J. Deng, Nam-Joon Cho, and Paula T. Hammond. 2014. 'Bimodal Tumor-Targeting from Microenvironment Responsive Hyaluronan Layer-by-Layer (LbL) Nanoparticles'. *ACS Nano* 8 (8): 8374–82. <https://doi.org/10.1021/nn502861t>.
- Elani, Y. 2016. 'Construction of Membrane-Bound Artificial Cells Using Microfluidics: A New Frontier in Bottom-up Synthetic Biology'. *Biochemical Society Transactions* 44 (3): 723–30. <https://doi.org/10.1042/BST20160052>.
- Feng, Tao, Xiangzhao Ai, Guanghui An, Piaoping Yang, and Yanli Zhao. 2016. 'Charge-Convertible Carbon Dots for Imaging-Guided Drug Delivery with Enhanced in Vivo Cancer Therapeutic Efficiency'. *ACS Nano* 10 (4): 4410–20. <https://doi.org/10.1021/acsnano.6b00043>.
- Flaten, Ellen Marie, Marion Seiersten, and Jens-Petter Andreassen. 2009. 'Polymorphism and Morphology of Calcium Carbonate Precipitated in Mixed Solvents of Ethylene Glycol and Water'. *Journal of Crystal Growth* 311 (13): 3533–38. <https://doi.org/10.1016/j.jcrysgro.2009.04.014>.
- Freeman, Ronit, and Itamar Willner. 2012. 'Optical Molecular Sensing with Semiconductor Quantum Dots (QDs)'. *Chemical Society Reviews* 41 (10): 4067. <https://doi.org/10.1039/c2cs15357b>.
- Futreal, P. Andrew, Lachlan Coin, Mhairi Marshall, Thomas Down, Timothy Hubbard, Richard Wooster, Nazneen Rahman, and Michael R. Stratton. 2004. 'A Census of Human Cancer Genes'. *Nature Reviews Cancer* 4 (3): 177–83. <https://doi.org/10.1038/nrc1299>.
- Gai, Meiyu, Valeriya L. Kudryavtseva, Gleb B. Sukhorukov, and Johannes Frueh. 2018. 'Micro-Patterned Polystyrene Sheets as Templates for Interlinked 3D Polyelectrolyte Multilayer Microstructures'. *BioNanoScience* 8 (2): 654–60. <https://doi.org/10.1007/s12668-017-0403-5>.
- Generalova, Alla N., Vladimir A. Oleinikov, Margarita M. Zarifullina, Ekaterina V. Lankina, Svetlana V. Sizova, Michail V. Artemyev, and Vitali P. Zubov. 2011. 'Optical Sensing Quantum Dot-Labeled Polyacrolein Particles Prepared by Layer-by-Layer Deposition Technique'. *Journal of Colloid and Interface Science* 357 (2): 265–72. <https://doi.org/10.1016/j.jcis.2011.02.002>.
- Ghosh, Harekrishna, and Thomas Bürgi. 2013. 'Adsorption of Gold and Silver Nanoparticles on Polyelectrolyte Layers and Growth of Polyelectrolyte Multilayers: An In Situ ATR-IR Study'. *The Journal of Physical Chemistry C* 117 (50): 26652–58. <https://doi.org/10.1021/jp409241t>.
- Golub, T. R., D. K. Slonim, P. Tamayo, C. Huard, M. Gaasenbeek, J. P. Mesirov, H. Collier, et al. 1999. 'Molecular Classification of Cancer: Class Discovery and Class Prediction by Gene Expression Monitoring'. *Science* 286 (5439): 531–37. <https://doi.org/10.1126/science.286.5439.531>.
- Goode, Jennifer. 2016. 'Use of International Standard ISO 10993-1, Biological Evaluation of Medical Devices - Part 1: Evaluation and Testing within a Risk Management Process'. *Department of Health and Human Services Food and Drug Administration*, 68. <http://www.fda.gov/downloads/medicaldevices/deviceregulationandguidance/guidancedocuments/ucm348890.pdf>.

- Goryacheva, Irina Yu., Elena S. Speranskaya, Valentina V. Goftman, Dianping Tang, and Sarah De Saeger. 2015a. 'Synthesis and Bioanalytical Applications of Nanostructures Multiloaded with Quantum Dots'. *TrAC Trends in Analytical Chemistry* 66 (March): 53–62. <https://doi.org/10.1016/j.trac.2014.11.008>.
- . 2015b. 'Synthesis and Bioanalytical Applications of Nanostructures Multiloaded with Quantum Dots'. *TrAC Trends in Analytical Chemistry* 66 (March): 53–62. <https://doi.org/10.1016/j.trac.2014.11.008>.
- Han, Haijie, Daniel Valdepérez, Qiao Jin, Bin Yang, Zuhong Li, Yulian Wu, Beatriz Pelaz, Wolfgang J. Parak, and Jian Ji. 2017. 'Dual Enzymatic Reaction-Assisted Gemcitabine Delivery Systems for Programmed Pancreatic Cancer Therapy'. *ACS Nano* 11 (2): 1281–91. <https://doi.org/10.1021/acsnano.6b05541>.
- Hanahan, Douglas, and Robert A Weinberg. 2000. 'The Hallmarks of Cancer'. *Cell* 100 (1): 57–70. [https://doi.org/10.1016/S0092-8674\(00\)81683-9](https://doi.org/10.1016/S0092-8674(00)81683-9).
- Hanahan, Douglas, and Robert A. Weinberg. 2011. 'Hallmarks of Cancer: The Next Generation'. *Cell* 144 (5): 646–74. <https://doi.org/10.1016/j.cell.2011.02.013>.
- Iannazzo, Daniela, Alessandro Pistone, Marina Salamò, Signorino Galvagno, Roberto Romeo, Salvatore V. Giofrè, Caterina Branca, Giuseppa Visalli, and Angela Di Pietro. 2017. 'Graphene Quantum Dots for Cancer Targeted Drug Delivery'. *International Journal of Pharmaceutics* 518 (1–2): 185–92. <https://doi.org/10.1016/j.ijpharm.2016.12.060>.
- Imai, Hiroaki, Natsuki Tochimoto, Yuichi Nishino, Yoko Takezawa, and Yuya Oaki. 2012. 'Oriented Nanocrystal Mosaic in Monodispersed CaCO<sub>3</sub> Microspheres with Functional Organic Molecules'. *Crystal Growth & Design* 12 (2): 876–82. <https://doi.org/10.1021/cg201301x>.
- James, Sally, James Fox, Farinaz Afsari, Jennifer Lee, Sally Clough, Charlotte Knight, James Ashmore, et al. 2015. 'Multiparameter Analysis of Human Bone Marrow Stromal Cells Identifies Distinct Immunomodulatory and Differentiation-Competent Subtypes'. *Stem Cell Reports* 4 (6): 1004–15. <https://doi.org/10.1016/j.stemcr.2015.05.005>.
- Jasieniak, Jacek, Marco Califano, and Scott E. Watkins. 2011. 'Size-Dependent Valence and Conduction Band-Edge Energies of Semiconductor Nanocrystals'. *ACS Nano* 5 (7): 5888–5902. <https://doi.org/10.1021/nn201681s>.
- Jia, Nengqin, Qiong Lian, Hebei Shen, Chen Wang, Xingyu Li, and Zhongnan Yang. 2007. 'Intracellular Delivery of Quantum Dots Tagged Antisense Oligodeoxynucleotides by Functionalized Multiwalled Carbon Nanotubes'. *Nano Letters* 7 (10): 2976–80. <https://doi.org/10.1021/nl071114c>.
- Johnston, Angus P.R., Christina Cortez, Alexandra S. Angelatos, and Frank Caruso. 2006. 'Layer-by-Layer Engineered Capsules and Their Applications'. *Current Opinion in Colloid & Interface Science* 11 (4): 203–9. <https://doi.org/10.1016/j.cocis.2006.05.001>.
- Kittitheeranun, Paveenuch, Warayuth Sajomsang, Sarunya Phanpee, Alongkot Treetong, Tuksadon Wutikhun, Kunat Suktham, Satit Puttipipatkachorn, and Uracha Rungsardthong Ruktanonchai. 2015. 'Layer-by-Layer Engineered Nanocapsules of Curcumin with Improved Cell Activity'. *International Journal of Pharmaceutics* 492 (1–2): 92–102. <https://doi.org/10.1016/j.ijpharm.2015.06.040>.
- Li, Wenwen, and Chao Gao. 2007. 'Efficiently Stabilized Spherical Vaterite CaCO<sub>3</sub> Crystals by Carbon Nanotubes in Biomimetic Mineralization'. *Langmuir* 23 (8): 4575–82. <https://doi.org/10.1021/la0632427>.
- Li, Xiankai, Lu Zong, Xiaochen Wu, Jun You, Mingjie Li, and Chaoxu Li. 2018. 'Biomimetic Engineering of Spider Silk Fibres with Graphene for Electric Devices with Humidity and Motion Sensitivity'. *Journal of Materials Chemistry C* 6 (13): 3212–19. <https://doi.org/10.1039/C8TC00265G>.
- Liao, Wei-Ching, Marianna Riutin, Wolfgang J. Parak, and Itamar Willner. 2016. 'Programmed PH-Responsive Microcapsules for the Controlled Release of CdSe/ZnS Quantum Dots'. *ACS Nano* 10 (9): 8683–89. <https://doi.org/10.1021/acsnano.6b04056>.
- Lim, Shi Ying, Wei Shen, and Zhiqiang Gao. 2015. 'Carbon Quantum Dots and Their Applications'. *Chemical Society Reviews* 44 (1): 362–81. <https://doi.org/10.1039/C4CS00269E>.
- Liu, Changjun, Peng Zhang, Xinyun Zhai, Feng Tian, Wenchen Li, Jianhai Yang, Yuan Liu, Hongbo Wang, Wei Wang, and Wenguang Liu. 2012. 'Nano-Carrier for Gene Delivery and Bioimaging Based on Carbon Dots with PEI-Passivation Enhanced Fluorescence'. *Biomaterials* 33 (13): 3604–13. <https://doi.org/10.1016/j.biomaterials.2012.01.052>.
- Liu, Xi Qiu, and Catherine Picart. 2016a. 'Layer-by-Layer Assemblies for Cancer Treatment and Diagnosis'. *Advanced Materials* 28 (6): 1295–1301. <https://doi.org/10.1002/adma.201502660>.
- . 2016b. 'Layer-by-Layer Assemblies for Cancer Treatment and Diagnosis'. *Advanced Materials* 28 (6): 1295–1301. <https://doi.org/10.1002/adma.201502660>.
- Ma, Q, X Wang, Y Li, Y Shi, and X Su. 2007. 'Multicolor Quantum Dot-Encoded Microspheres for the Detection of Biomolecules'. *Talanta* 72 (4): 1446–52. <https://doi.org/10.1016/j.talanta.2007.01.058>.
- Ma, Yufei, Jie Huang, Saijie Song, Huabing Chen, and Zhijun Zhang. 2016. 'Cancer-Targeted Nanotheranostics: Recent Advances and Perspectives'. *Small* 12 (36): 4936–54. <https://doi.org/10.1002/smll.201600635>.
- Macdonald, Mara L., Raymond E. Samuel, Nisarg J. Shah, Robert F. Padera, Yvette M. Beben, and Paula T. Hammond. 2011. 'Tissue Integration of Growth Factor-Eluting Layer-by-Layer Polyelectrolyte Multilayer Coated Implants'. *Biomaterials* 32 (5): 1446–53. <https://doi.org/10.1016/j.biomaterials.2010.10.052>.
- Masood, Farha. 2016. 'Polymeric Nanoparticles for Targeted Drug Delivery System for Cancer Therapy'. *Materials Science and Engineering: C* 60 (March): 569–78. <https://doi.org/10.1016/j.msec.2015.11.067>.

- Matea, Cristian, Teodora Mocan, Flaviu Tabaran, Teodora Pop, Ofelia Mosteanu, Cosmin Puia, Cornel Iancu, and Lucian Mocan. 2017. 'Quantum Dots in Imaging, Drug Delivery and Sensor Applications'. *International Journal of Nanomedicine* Volume 12 (July): 5421–31. <https://doi.org/10.2147/IJN.S138624>.
- Mattu, C., G. Brachi, L. Menichetti, A. Flori, P. Armanetti, E. Ranzato, S. Martinotti, S. Nizzero, M. Ferrari, and G. Ciardelli. 2018. 'Alternating Block Copolymer-Based Nanoparticles as Tools to Modulate the Loading of Multiple Chemotherapeutics and Imaging Probes'. *Acta Biomaterialia* 80 (October): 341–51. <https://doi.org/10.1016/j.actbio.2018.09.021>.
- Melancon, Marites P., R. Jason Stafford, and Chun Li. 2012. 'Challenges to Effective Cancer Nanotheranostics'. *Journal of Controlled Release* 164 (2): 177–82. <https://doi.org/10.1016/j.jconrel.2012.07.045>.
- Mohammad, Faruq, Ibrahim birma Bwatanglang, Nor Azah Yusof, Jaafar Abdullah, Mohd Zobir Hussein, Noorjahan Banu Alitheen, and Nadiyah Abu. 2016. 'Folic Acid Targeted Mn:ZnS Quantum Dots for Theranostic Applications of Cancer Cell Imaging and Therapy'. *International Journal of Nanomedicine*, January, 413. <https://doi.org/10.2147/IJN.S90198>.
- Montalbano, G., S. Toumpaniari, A. Popov, P. Duan, J. Chen, K. Dalgarno, W. E. Scott, and A. M. Ferreira. 2018. 'Synthesis of Bioinspired Collagen/Alginate/Fibrin Based Hydrogels for Soft Tissue Engineering'. *Materials Science and Engineering C* 91 (March): 236–46. <https://doi.org/10.1016/j.msec.2018.04.101>.
- Morton, Stephen W., Kevin P. Herlihy, Kevin E. Shopsowitz, Zhou J. Deng, Kevin S. Chu, Charles J. Bowerman, Joseph M. DeSimone, and Paula T. Hammond. 2013. 'Scalable Manufacture of Built-to-Order Nanomedicine: Spray-Assisted Layer-by-Layer Fractionalization of PRINT Nanoparticles'. *Advanced Materials* 25 (34): 4707–13. <https://doi.org/10.1002/adma.201302025>.
- Nagaraja, Ashvin T., Sulolit Pradhan, and Michael J. McShane. 2014. 'Poly (Vinylsulfonic Acid) Assisted Synthesis of Aqueous Solution Stable Vaterite Calcium Carbonate Nanoparticles'. *Journal of Colloid and Interface Science* 418 (March): 366–72. <https://doi.org/10.1016/j.jcis.2013.12.008>.
- Nair, Raji V., Reny Thankam Thomas, Vandana Sankar, Hanif Muhammad, Mingdong Dong, and Saju Pillai. 2017a. 'Rapid, Acid-Free Synthesis of High-Quality Graphene Quantum Dots for Aggregation Induced Sensing of Metal Ions and Bioimaging'. *ACS Omega* 2 (11): 8051–61. <https://doi.org/10.1021/acsomega.7b01262>.
- . 2017b. 'Rapid, Acid-Free Synthesis of High-Quality Graphene Quantum Dots for Aggregation Induced Sensing of Metal Ions and Bioimaging'. *ACS Omega* 2 (11): 8051–61. <https://doi.org/10.1021/acsomega.7b01262>.
- Olerile, Livesey David, Yongjun Liu, Bo Zhang, Tianqi Wang, Shengjun Mu, Jing Zhang, Lesego Selotlegeng, and Na Zhang. 2017. 'Near-Infrared Mediated Quantum Dots and Paclitaxel Co-Loaded Nanostructured Lipid Carriers for Cancer Theragnostic'. *Colloids and Surfaces B: Biointerfaces* 150 (February): 121–30. <https://doi.org/10.1016/j.colsurfb.2016.11.032>.
- Paltrinieri, Laura, Min Wang, Sumit Sachdeva, Nicolaas A. M. Besseling, Ernst J. R. Sudhölter, and Louis C. P. M. de Smet. 2017. 'Fe<sub>3</sub>O<sub>4</sub> Nanoparticles Coated with a Guanidinium-Functionalized Polyelectrolyte Extend the PH Range for Phosphate Binding'. *Journal of Materials Chemistry A* 5 (35): 18476–85. <https://doi.org/10.1039/C7TA04054G>.
- Pan, Dengyu, Jingchun Zhang, Zhen Li, and Minghong Wu. 2010. 'Hydrothermal Route for Cutting Graphene Sheets into Blue-Luminescent Graphene Quantum Dots'. *Advanced Materials* 22 (6): 734–38. <https://doi.org/10.1002/adma.200902825>.
- Pierrat, Philippe, Rongrong Wang, Dimitri Kereselidze, Marie Lux, Pascal Didier, Antoine Kichler, Françoise Pons, and Luc Lebeau. 2015a. 'Efficient in Vitro and in Vivo Pulmonary Delivery of Nucleic Acid by Carbon Dot-Based Nanocarriers'. *Biomaterials* 51 (May): 290–302. <https://doi.org/10.1016/j.biomaterials.2015.02.017>.
- . 2015b. 'Efficient in Vitro and in Vivo Pulmonary Delivery of Nucleic Acid by Carbon Dot-Based Nanocarriers'. *Biomaterials* 51 (May): 290–302. <https://doi.org/10.1016/j.biomaterials.2015.02.017>.
- Poon, Zhiyong, Dongsook Chang, Xiaoyong Zhao, and Paula T Hammond. 2011. 'Layer-by-Layer Nanoparticles with a PH-Sheddable Layer for *in Vivo* Targeting of Tumor Hypoxia'. *ACS Nano* 5 (6): 4284–92. <https://doi.org/10.1021/nn200876f>.
- Richardson, J. J., M. Bjornmalm, and F. Caruso. 2015. 'Technology-Driven Layer-by-Layer Assembly of Nanofilms'. *Science* 348 (6233): aaa2491–aaa2491. <https://doi.org/10.1126/science.aaa2491>.
- Richardson, Joseph J., Jiwei Cui, Mattias Björnalm, Julia A. Braunger, Hirotaka Ejima, and Frank Caruso. 2016. 'Innovation in Layer-by-Layer Assembly'. *Chemical Reviews* 116 (23): 14828–67. <https://doi.org/10.1021/acs.chemrev.6b00627>.
- Rinckenbach, Simon, Joseph Hemmerlé, Florence Dieval, Youri Arntz, Jean-Georges Kretz, Bernard Durand, Nabil Chakfe, Pierre Schaaf, Jean-Claude Voegel, and Dominique Vautier. 2008. 'Characterization of Polyelectrolyte Multilayer Films on Polyethylene Terephthalate Vascular Prostheses under Mechanical Stretching'. *Journal of Biomedical Materials Research Part A* 84A (3): 576–88. <https://doi.org/10.1002/jbm.a.31333>.
- Ritter, Kyle A., and Joseph W. Lyding. 2009. 'The Influence of Edge Structure on the Electronic Properties of Graphene Quantum Dots and Nanoribbons'. *Nature Materials* 8 (3): 235–42. <https://doi.org/10.1038/nmat2378>.
- Roy, Prathik, Arun Prakash Periasamy, Chiashain Chuang, Yi-Rou Liou, Yang-Fang Chen, Joseph Joly, Chi-Te Liang, and Huan-Tsung Chang. 2014. 'Plant Leaf-Derived Graphene Quantum Dots and Applications for White LEDs'. *New J. Chem.* 38 (10): 4946–51. <https://doi.org/10.1039/C4NJ01185F>.

- Sabra, Sally, Mona Abdelmoneem, Mahmoud Abdelwakil, Moustafa Taha Mabrouk, Doaa Anwar, Rania Mohamed, Sherine Khattab, et al. 2018. 'Self-Assembled Nanocarriers Based on Amphiphilic Natural Polymers for Anti- Cancer Drug Delivery Applications'. *Current Pharmaceutical Design* 23 (35). <https://doi.org/10.2174/1381612823666170526111029>.
- Saqib, J., and Isam H. Aljundi. 2016. 'Membrane Fouling and Modification Using Surface Treatment and Layer-by-Layer Assembly of Polyelectrolytes: State-of-the-Art Review'. *Journal of Water Process Engineering* 11 (June): 68–87. <https://doi.org/10.1016/j.jwpe.2016.03.009>.
- Sharma, Parvesh, Scott Brown, Glenn Walter, Swadeshmukul Santra, and Brij Moudgil. 2006. 'Nanoparticles for Bioimaging'. *Advances in Colloid and Interface Science* 123–126 (November): 471–85. <https://doi.org/10.1016/j.cis.2006.05.026>.
- Silva, Catarina Oliveira, Jacinta Oliveira Pinho, Joana Margarida Lopes, António J. Almeida, Maria Manuela Gaspar, and Catarina Reis. 2019. 'Current Trends in Cancer Nanotheranostics: Metallic, Polymeric, and Lipid-Based Systems'. *Pharmaceutics* 11 (1): 22. <https://doi.org/10.3390/pharmaceutics11010022>.
- Sui, Xin, Chao Luo, Chong Wang, Fangwei Zhang, Jingyan Zhang, and Shouwu Guo. 2016. 'Graphene Quantum Dots Enhance Anticancer Activity of Cisplatin via Increasing Its Cellular and Nuclear Uptake'. *Nanomedicine: Nanotechnology, Biology and Medicine* 12 (7): 1997–2006. <https://doi.org/10.1016/j.nano.2016.03.010>.
- Tai, Clifford Y., and F.-B. Chen. 1998. 'Polymorphism of CaCO<sub>3</sub>, Precipitated in a Constant-Composition Environment'. *AIChE Journal* 44 (8): 1790–98. <https://doi.org/10.1002/aic.690440810>.
- Tonda-Turo, Chiara, Irene Carmagnola, and Gianluca Ciardelli. 2018. 'Quartz Crystal Microbalance With Dissipation Monitoring: A Powerful Method to Predict the in Vivo Behavior of Bioengineered Surfaces'. *Frontiers in Bioengineering and Biotechnology* 6 (October): 158. <https://doi.org/10.3389/fbioe.2018.00158>.
- Trushina, Daria B., Tatiana V. Bukreeva, and Maria N. Antipina. 2016. 'Size-Controlled Synthesis of Vaterite Calcium Carbonate by the Mixing Method: Aiming for Nanosized Particles'. *Crystal Growth & Design* 16 (3): 1311–19. <https://doi.org/10.1021/acs.cgd.5b01422>.
- Trushina, Daria B., Tatiana V. Bukreeva, Mikhail V. Kovalchuk, and Maria N. Antipina. 2014. 'CaCO<sub>3</sub> Vaterite Microparticles for Biomedical and Personal Care Applications'. *Materials Science and Engineering: C* 45 (December): 644–58. <https://doi.org/10.1016/j.msec.2014.04.050>.
- Volodkin, Dmitry V., Natalia I. Larionova, and Gleb B. Sukhorukov. 2004. 'Protein Encapsulation via Porous CaCO<sub>3</sub> Microparticles Templating'. *Biomacromolecules* 5 (5): 1962–72. <https://doi.org/10.1021/bm049669e>.
- Volodkin, Dmitry V., Alexander I. Petrov, Michelle Prevot, and Gleb B. Sukhorukov. 2004. 'Matrix Polyelectrolyte Microcapsules: New System for Macromolecule Encapsulation'. *Langmuir* 20 (8): 3398–3406. <https://doi.org/10.1021/la036177z>.
- Vozar, Steven, Yeh-Chuin Poh, Thomas Serbowicz, Matthew Bachner, Paul Podsiadlo, Ming Qin, Eric Verploegen, Nicholas Kotov, and A. John Hart. 2009. 'Automated Spin-Assisted Layer-by-Layer Assembly of Nanocomposites'. *Review of Scientific Instruments* 80 (2): 023903. <https://doi.org/10.1063/1.3078009>.
- Wang, Lei, Shou-Jun Zhu, Hai-Yu Wang, Song-Nan Qu, Yong-Lai Zhang, Jun-Hu Zhang, Qi-Dai Chen, et al. 2014. 'Common Origin of Green Luminescence in Carbon Nanodots and Graphene Quantum Dots'. *ACS Nano* 8 (3): 2541–47. <https://doi.org/10.1021/nn500368m>.
- Wang, Liang, Weitao Li, Bin Wu, Zhen Li, Shilong Wang, Yuan Liu, Dengyu Pan, and Minghong Wu. 2016a. 'Facile Synthesis of Fluorescent Graphene Quantum Dots from Coffee Grounds for Bioimaging and Sensing'. *Chemical Engineering Journal* 300 (September): 75–82. <https://doi.org/10.1016/j.cej.2016.04.123>.
- . 2016b. 'Facile Synthesis of Fluorescent Graphene Quantum Dots from Coffee Grounds for Bioimaging and Sensing'. *Chemical Engineering Journal* 300 (September): 75–82. <https://doi.org/10.1016/j.cej.2016.04.123>.
- Wang, Xiaoli, Rui Kong, Xiaoxiao Pan, Hai Xu, Daohong Xia, Honghong Shan, and Jian R. Lu. 2009. 'Role of Ovalbumin in the Stabilization of Metastable Vaterite in Calcium Carbonate Biomineralization'. *The Journal of Physical Chemistry B* 113 (26): 8975–82. <https://doi.org/10.1021/jp810281f>.
- Wang, Yanli, Parambath Anilkumar, Li Cao, Jia-Hui Liu, Pengju G Luo, Kenneth N Tackett, Sushant Sahu, Ping Wang, Xin Wang, and Ya-Ping Sun. 2011. 'Carbon Dots of Different Composition and Surface Functionalization: Cytotoxicity Issues Relevant to Fluorescence Cell Imaging'. *Experimental Biology and Medicine* 236 (11): 1231–38. <https://doi.org/10.1258/ebm.2011.011132>.
- Wang, Zhaofeng, Jingfang Yu, Xin Zhang, Na Li, Bin Liu, Yanyan Li, Yuhua Wang, et al. 2016. 'Large-Scale and Controllable Synthesis of Graphene Quantum Dots from Rice Husk Biomass: A Comprehensive Utilization Strategy'. *ACS Applied Materials & Interfaces* 8 (2): 1434–39. <https://doi.org/10.1021/acsami.5b10660>.
- Wang, Zifei, Fanglong Yuan, Xiaohong Li, Yunchao Li, Haizheng Zhong, Louzhen Fan, and Shihe Yang. 2017. '53% Efficient Red Emissive Carbon Quantum Dots for High Color Rendering and Stable Warm White-Light-Emitting Diodes'. *Advanced Materials* 29 (37): 1702910. <https://doi.org/10.1002/adma.201702910>.
- Wang, Zonghua, Jianfei Xia, Chengfeng Zhou, Brian Via, Yanzhi Xia, Feifei Zhang, Yanhui Li, Linhua Xia, and Jie Tang. 2013. 'Synthesis of Strongly Green-Photoluminescent Graphene Quantum Dots for Drug Carrier'. *Colloids and Surfaces B: Biointerfaces* 112 (December): 192–96. <https://doi.org/10.1016/j.colsurfb.2013.07.025>.
- Won, Yu-Ho, Ho Seong Jang, Ding-Wen Chung, and Lia A. Stanciu. 2010. 'Multifunctional Calcium Carbonate Microparticles: Synthesis and Biological Applications'. *Journal of Materials Chemistry* 20 (36): 7728. <https://doi.org/10.1039/c0jm01231a>.

- Wu, Congyu, Chong Wang, Ting Han, Xuejiao Zhou, Shouwu Guo, and Jingyan Zhang. 2013a. 'Insight into the Cellular Internalization and Cytotoxicity of Graphene Quantum Dots'. *Advanced Healthcare Materials* 2 (12): 1613–19. <https://doi.org/10.1002/adhm.201300066>.
- . 2013b. 'Insight into the Cellular Internalization and Cytotoxicity of Graphene Quantum Dots'. *Advanced Healthcare Materials* 2 (12): 1613–19. <https://doi.org/10.1002/adhm.201300066>.
- Xiao, Fang-Xing, Mario Pagliaro, Yi-Jun Xu, and Bin Liu. 2016. 'Layer-by-Layer Assembly of Versatile Nanoarchitectures with Diverse Dimensionality: A New Perspective for Rational Construction of Multilayer Assemblies'. *Chemical Society Reviews* 45 (11): 3088–3121. <https://doi.org/10.1039/C5CS00781J>.
- Xue, Xiangdong, Yee Huang, Ruonan Bo, Bei Jia, Hao Wu, Ye Yuan, Zhongling Wang, et al. 2018. 'Trojan Horse Nanotheranostics with Dual Transformability and Multifunctionality for Highly Effective Cancer Treatment'. *Nature Communications* 9 (1): 3653. <https://doi.org/10.1038/s41467-018-06093-5>.
- Yashchenok, Alexey, Bogdan Parakhonskiy, Senem Donatan, Dorothee Kohler, Andre Skirtach, and Helmuth Möhwald. 2013. 'Polyelectrolyte Multilayer Microcapsules Templated on Spherical, Elliptical and Square Calcium Carbonate Particles'. *Journal of Materials Chemistry B* 1 (9): 1223. <https://doi.org/10.1039/c2tb00416j>.
- Yuan, Xiaochan, Zhiming Liu, Zhouyi Guo, Yanhong Ji, Mei Jin, and Xinpeng Wang. 2014. 'Cellular Distribution and Cytotoxicity of Graphene Quantum Dots with Different Functional Groups'. *Nanoscale Research Letters* 9 (1): 108. <https://doi.org/10.1186/1556-276X-9-108>.
- Zhang, Ming, Turker Yilmaz, Ali Ozgur Boztas, Ozgur Karakuzu, Woo Young Bang, Yagmur Yegin, Zhiping Luo, Mark Lenox, Luis Cisneros-Zevallos, and Mustafa Akbulut. 2016. 'A Multifunctional Nanoparticulate Theranostic System with Simultaneous Chemotherapeutic, Photothermal Therapeutic, and MRI Contrast Capabilities'. *RSC Advances* 6 (33): 27798–806. <https://doi.org/10.1039/C5RA27792B>.
- Zhang, Mo, Linling Bai, Weihua Shang, Wenjing Xie, Hong Ma, Yingyi Fu, Decai Fang, et al. 2012. 'Facile Synthesis of Water-Soluble, Highly Fluorescent Graphene Quantum Dots as a Robust Biological Label for Stem Cells'. *Journal of Materials Chemistry* 22 (15): 7461. <https://doi.org/10.1039/c2jm16835a>.
- Zhao, Shaojing, Minhuan Lan, Xiaoyue Zhu, Hongtao Xue, Tsz-Wai Ng, Xiangmin Meng, Chun-Sing Lee, Pengfei Wang, and Wenjun Zhang. 2015. 'Green Synthesis of Bifunctional Fluorescent Carbon Dots from Garlic for Cellular Imaging and Free Radical Scavenging'. *ACS Applied Materials & Interfaces* 7 (31): 17054–60. <https://doi.org/10.1021/acsami.5b03228>.
- Zhao, Tingting, Xuebin Li, Mingguang Zhang, Jian He, Xuwen Zhang, Hui Liu, Xingguo Wang, and Haoshuang Gu. 2017. 'Fluorescence and Drug Loading Properties of ZnSe:Mn/ZnS-Paclitaxel/SiO<sub>2</sub> Nanocapsules Templated by F127 Micelles'. *Journal of Colloid and Interface Science* 490 (March): 436–43. <https://doi.org/10.1016/j.jcis.2016.11.079>.
- Zheng, Xin Ting, Arundithi Ananthanarayanan, Kathy Qian Luo, and Peng Chen. 2015a. 'Glowing Graphene Quantum Dots and Carbon Dots: Properties, Syntheses, and Biological Applications'. *Small* 11 (14): 1620–36. <https://doi.org/10.1002/smll.201402648>.
- . 2015b. 'Glowing Graphene Quantum Dots and Carbon Dots: Properties, Syntheses, and Biological Applications'. *Small* 11 (14): 1620–36. <https://doi.org/10.1002/smll.201402648>.
- Zhu, Shoujun, Jieren Shao, Yubin Song, Xiaohuan Zhao, Jianglin Du, Lei Wang, Haiyu Wang, Junhu Zhang, and Bai Yang. n.d. 'Deeply Investigating the Surface State of Graphene Quantum Dots', 7.
- Zhu, Shoujun, Yubin Song, Joy Wang, Hao Wan, Yuan Zhang, Yang Ning, and Bai Yang. 2017. 'Photoluminescence Mechanism in Graphene Quantum Dots: Quantum Confinement Effect and Surface/Edge State'. *Nano Today* 13 (April): 10–14. <https://doi.org/10.1016/j.nantod.2016.12.006>.

## Website

[www.cancerresearchuk.org](http://www.cancerresearchuk.org)